Water-Assisted Synthesis of Next Generation 2D Materials for Energy Storage

Uthman Kayode Alli

A thesis submitted in fulfilment of the degree of Doctor of Philosophy in Chemical Process and Energy Engineering, in the Department of Chemical Sciences, School of Engineering, London South Bank University.

Supervisors: Dr. Suela Kellici (1st)

Prof. Steve Dunn (2nd)

September 2022

Declaration

I declare that this Ph.D. thesis writing titled "Water-Assisted Synthesis of Next Generation 2D materials for Energy Storage" is my work, and it has not been submitted in any other university towards a degree, and all sources used have been acknowledged with references and permissions granted where required.

Dedication

To my beautiful daughter Layla Alli

and

To my Late Grandfather; Aare Hadji Abdul-Lateef Olatokunbo Alli.

Acknowledgements

After an eventful three years of research, I would like to express sincere gratitude to all those involved in bringing this work to a successful conclusion.

My most immense gratitude goes to Almighty Allah for the grace of good health, strength, and wisdom given to me in ensuring the completion of this research study.

I am grateful to Dr. Kellici and Prof. Dunn for their outstanding support and supervision throughout my research work process. My supervisors' passion and commitment to research have catalysed my progress in my personal development and research. Many thanks go to Dr. Power (Open University, Milton Keynes- United Kingdom) for his guidance and the tremendous support he has given to me as a visiting research student. I would like to acknowledge the members of the EM Suite (Open University (OU), United Kingdom) for their excellent work in SEM and TEM imaging of my MXene samples in chapters 6 & 7. Thanks to Dr. Tobias Heil (Max Planck Institute of Colloids and Interfaces, Germany) for the TEM measurements on TiO2 -rGO sample. Thanks to Dr. Avishek Dey (OU), Dr Matthew Kershaw (OU) for their respective support in conducting Raman and XRD measurements. Acknowledgements go to Dr. David Morgan (Cardiff University, United Kingdom) for XPS measurements of NMT, MnO_2 and TiO_2 samples, and peak fittings of NMT samples in chapter 6. Much appreciation goes to PhD Dana Popescu (National Institute of Materials Physics, Romania) for peak fittings of MnO_2 samples, and for XPS measurements and peak fittings of NMT CYR. Also, I want to acknowledge Kieran McCarthy, Seamus Killian and Dr. Tadhg Kennedy (Bernal Institute, University of Limerick, Ireland) for their collaboration and performing electrochemical tests and analysis on NMT samples.

To Dr. Ioan Alexandru Baragau and my Nano2Dlab research colleagues (Dr. Zhen Lu, Dr. Sunil Hettiarachchi, Kiem Ngyuen, and Conor Davids), I say thank you for all your moral support and help rendered during this study. Much thanks also go to Dr. Matthew Billing, and Guru Subramaniam for all the knowledge and experience shared during my research journey.

I want to extend more gratitude to my family, Alhaji and Alhaja M.O Alli, for their immeasurable love and support, the family of Mr. E.O Idowu, for their words of encouragement and prayers. I want to thank my good friends Dr. Williams Ali and Dr. Kenechukwu Udechukwu for their moral support and consistent thrive for my development. I also want to thank Bintu Kemokai, for her support and patience. It is a blessing to have our beautiful daughter Layla with you. Finally, my warmest gratitude extends to Miss Destiny Chunda for the considerate, unselfish and loving heart that you have, as only a few are able to give much of themselves. I am blessed to have you in my life.

Table of Contents

Abbreviations

0D – Zero Dimensional

1D – One Dimensional

2D – Two Dimensional

3D – Three Dimensional

3MT – Three Minutes Thesis

AC - Activated Carbon

ACN – Acrylonitrile

AFM – Atomic Force Microscopy

BET- Brunauer-Emmett Teller Surface Area Analysis

BHS – Batch Hydrothermal Synthesis

BP – Black Phosphorus

CAG - Carbon Aerogels

CE – Coulombic Efficiency

CHFS - Continuous Hydrothermal Flow Synthesis

c-LP – Crystal Lattice Parameter

CNT – Carbon NanoTubes

CQDs – Carbon Quantum Dots

CV - Cyclic Voltammetry

CVD – Chemical Vapor Deposition

CYR - Cyrene

d-MXene – Dimethyl Sulfoxide Delaminated MXene

DMC – Dimethyl Carbonate

DMSO – Dimethyl Sulfoxide

DMF – Dimethyl Formamide

EC – Ethylene Carbonate

EC - Electrochemical Capacitors

E. Coli - Escherichia Coli

EDL – Electric Double Layer

EDLC – Electric Double Layer Capacitor

EDS – Electron Dispersive X-ray Spectroscopy

EIS - Electrochemical Impedance Spectroscopy

EM – Electron Microscopy

ESD- Energy Storage Device

F1 – Feed 1

F2 – Feed 2

F3 – Feed 3

FT-IR – Fourier-Transform Infrared

GCD - Galvanostatic Charge- Discharge (GCD)

GHG - Greenhouse Gas

GO - Graphene Oxide

GQDs – Graphene Quantum Dots

HER – Hydrogen Evolution Reaction

HRTEM – High Resolution Transmission Electron Microscopy

HSP – Hansen Solubility Parameters

LCA – Life Cycle Assessment

LIBs - Lithium-Ion Batteries

$LiPF_6$ – Lithium Hexafluoro Phosphate

LMO – Lithium Manganese Oxides

LPE – Liquid Phase Exfoliation

NMP – N-Methyl-2-pyrrolidone

NMT – N-doped MXene-TiO_2

PANI – Polyaniline

PEDOT – Poly (3,4- ethylene dioxythiophene)

pH – Potential of Hydrogen

PPy – Polypyrrole

PVDF – Polyvinylidene Fluoride

rGO – Reduced Graphene Oxide

SAED – Selected Area Electron Diffraction

SEI – Solid Electrolyte Interface

SEM - Scanning Electron Microscopy

SSA - Specific Surface Area

S. aureus – Staphylococcus aureus

$TEABF_4$ – Tetraethyl Ammonium Tetra Fluoroborate

TEM - Trasmission Electron Microscopy

TMD – Transition Metal Dichalgonides

TMO - Transition Metal Oxides

XPS – X-ray Photoelectron Spectroscopy

XRD - X-ray Diffraction

Units

A – Ampere

Å – Angostroms

cm – Centimetre

°C - Degree Celsius

eV – Electron Volt

F – Farad

g – Grams

h – Hour

J - Joule

m – Metre

mg – Milligram

mL – Millilitre

mN – MilliNewton

µm – Micrometre

MPa – MegaPascal

nm – Nanometre

% - Percentage

S m^{-1} – Coulomb per metre

s – Second

V – Volts

W – Watts

Abstract

Over the years, various nanomaterials are continuously researched and synthesised to improve energy storage devices' energy and power densities. Two-Dimensional (2D) materials have developed great interest as a new prototype in materials science due to their collective advantages of ultrathin thickness and tuneable physical and chemical properties. The application of these nanomaterials extends to energy storage, water purification, catalysis, biosensors, antibacterial films, and coatings, thereby prompting the development of viable techniques for synthesising nanomaterials. However, challenges of further size reduction of nanomaterials with a simultaneous low cost, scalable and reproducible synthesis approach remain famous for sustainable progress in their practical applications.

For the first time, 2D Graphene and MXene composite materials were synthesised through a Continuous Hydrothermal Flow Synthesis (CHFS) method and engineered into electrodes for electrochemical energy storage applications. CHFS is a single-step hydrothermal process involving mixing supercritical water (374 °C, 22.4 MPa) with a flow of water-soluble precursors in a reactor to obtain a rapid and controlled synthesis of nanomaterials. This synthesis method is scalable and tuneable by controlling process parameters such as flow rate, temperature, and pressure, thereby impacting the particle size, morphology, and crystal structure of nanoparticles. In addition, CHFS limits the use of toxic reagents and produces nanomaterials with desired properties in minimal time (seconds). One of the findings in this research paves way for the in-situ production and aqueous processing of functionalised MXene composites with a high electrochemical performance. Through aqueous dispersions as a green route of synthesis in CHFS, these 2D MXene and graphene derivatives were produced with enhanced electrochemical properties. This research provides a significant contribution to the expanding portfolio of continuous hydrothermal flow synthesis reactions.

In this thesis, a variety of materials such as manganese (iv) oxide, manganese (iv) oxide/ reduced graphene oxide (rGO), titanium (iv) oxide, titanium (iv) oxide/ reduced graphene oxide (rGO), and N-doped MXene/ titanium (iv) oxide, are hydrothermally synthesised via CHFS, developed and fabricated into electrode materials for energy storage applications.

The in-depth analysis provides a comprehensive insight into how nanocomposites of promising energy storage properties are designable, made functional, and synthesised in-situ hydrothermally via CHFS from non-toxic and water-soluble precursors while delivering excellent electrochemical performance when used as electrodes in batteries.

Research Outputs

List of Publications

Review Article : **Chemical Functionalisation of 2D Materials via Batch and Continuous Hydrothermal Flow Synthesis** U. Alli, S. J. Hettiarachchi and S. Kellici, *Chem. - A Eur. J.*, 2020, 6447–6460.

Research Article: **In-situ Continuous Hydrothermal Synthesis of TiO_2 Nanoparticles on Conductive N-doped MXene Nanosheets for Li-ion storage** U. Alli, K. McCarthy, I. Baragau, N. P. Power, D. J. Morgan, S.Dunn, S. Killian, T. Kennedy, and S. Kellici, Chemical Engineering Journal, 2022, 430, 132976.

Review Article: **A Review on the Classification and Types of Heteroatoms Doping in 2D Structures (under submission review)**

Participation in Conferences/Seminars

2018 - Centre for Advanced Materials Research Workshop: Oral Presentation

2020 - MXene Conference and Workshop: Online Participation

2020 - Summer School: Poster Presentation

2020 - Summer School (3MT Presentation): Oral Presentation

2020 - Chemistry of 2D materials beyond graphene: Poster exhibition

List of Figures

List of Tables

Chapter 1: Introduction

1.1 Overview

With the global warning of climate change and the increase in energy demands, the world has turned to renewable energy sources to solve these challenges. However, these renewable energy sources (wind, solar, hydropower, biomass, etc.) also face challenges of creating cheaper and more efficient technologies in storing these intermittent energies[1]. Due to this, there is a need to find economically viable and environmentally friendly sources of energy supply or storage such as batteries and supercapacitors. Current materials used in energy storage (e.g., cobalt, nickel, and manganese) are not cost-efficient; in selected cases, performance is limited and associated with environmental and economic concerns. For example, the cost of cobalt (Co) used in the cathode material of lithium-ion batteries is expensive and not sufficient to meet the global demands for rechargeable energies[2].

Energy sources have evolved from traditional wood-burning to coal, crude oil, natural gas, and petrochemical energy sources (tar sands and shale deposits). As these fossil fuels' exploitation continues due to energy demands worldwide, their reserves are depleting with time and simultaneously raising environmental concerns due to greenhouse gases (GHG) emissions. The energy industry requires an economically viable technological innovation to level up the energy deficiency, store energy when needed, and deliver power when needed while considering environmental protection. The time variance of some energy sources does not correspond to the time dependence of energy use[3]. For example, the energy obtained from biofuels and other sources such as solar and wind is only available during a specific period, making the concept of energy storage essential for conservation and storage for later use when needed.

As growing concerns for climate change and fossil depletion continue, the development of energy storage devices (ESD) has increased interest in storing energy of different forms and converting it to its required format, producing large capacity and high-rate capability[3]. These energy storage devices provide the energy and power requirements for different electrical systems and devices such as electric vehicles, smart devices, mobile phones etc.

Energy storage devices such as batteries and electrochemical capacitors (EC) have distinctive energy storage mechanisms. Batteries store energy in chemical potential, while ECs store energy as charges[3]. These distinct energy storage mechanisms exhibited by batteries and ECs characterise both devices with different energy and power densities and their lifecycles. Faradaic processes occurring at the interface between the electrode and electrolyte in batteries provide larger energy densities. Still, they suffer from poor stability due to changes in the chemical structure of electrode material after redox reactions from several charges and discharge cycles. Electrochemical capacitors, on the other hand, store charges faster than batteries and have a number of charged and discharged cycles with no significant change in the crystal structure of the electrode material, thereby providing ECs with large power densities suitable for use in operations with high power requirements and improved acceleration in electric vehicles. In addition, charge and discharge cycles in ECs takes seconds which reduces the amount of time required for a full charge compared to batteries[3].

Despite these exciting properties exhibited by batteries and ECs, limitations in their functions are often due to costs, performance, and environmental concerns. Batteries suffer from low power densities and stability of electrode material after several charge-discharge cycles, while ECs suffer from low energy densities[4]. The electrode material plays a vital role in the functioning of an ESD. Common materials employed in electrode fabrication include carbon-based materials like activated carbon (AC)[5], graphite[6] and carbon nanotubes (CNTs)[7]. These materials are inexpensive, easily accessible, non-toxic, quickly processed, and have high chemical stability, making them a suitable electrode material for energy storage devices.

An electrode material's specific surface area (SSA), ionic and electronic conductivities and thermal and chemical stabilities are essential for engineering an energy storage device with superior energy, power, and operation parameters. The Brunauer-Emmett Teller (BET) analysis provides information about the amount of surface area of the material available for chemical reactions (in batteries) and storing charges (in ECs). However, not all this surface area is easily accessible by electrolytes[8]. Improved ionic and electronic conductivities increase charge carriers (ions and electrons) transport during energy storage reactions[9]. The thermal and chemical stabilities of the electrode material in aqueous and non-aqueous electrolytes increases the number of charge-discharge cycles, the lifecycle of the device, and its use in temperature-dependent applications[10,11]. All these properties, when appropriately engineered, provide an energy storage device with superior electrochemical function.

Two-dimensional (2D) nanomaterials in energy storage applications are a prospective and efficient solution due to their tunability and superior properties[12]. Ultrathin two-dimensional (2D) nanomaterials have exciting electronic properties due to the confinement of electrons in two dimensions, helpful for related electronic applications such as electronic/ optoelectronic device[13]. Their atomic thickness and large lateral size contribute to their very high specific surface area, making them attractive in surface-related applications such as catalysis and energy storage devices[14]. 2D materials are single layer materials with an atomic layer thickness of a few nanometres obtained by reducing their corresponding three dimensional (3D) material[12]. Examples of 2D materials are graphene, a single atomic layer of graphite with sp^2 hybridisation, a thin atomic thickness of 0.345 nm[15], and MXene, atomic layers of transition metal alternating between carbonic atomic layers[16]. Graphene shows electron mobility at room temperature, intrinsic strength and high thermal conductivity[17]. MXene exhibits excellent electrical conductivity, unique morphology, and hydrophilicity of its functionalised surface, influencing its electrochemical performance[18].

Research in transition metals oxides (TMO) is extensive due to their high specific capacitance and low resistance, relevant in energy storage applications[19]. Common TMOs used in energy storage such as oxides of cobalt, iron and nickel are not cost-efficient and limited due to lack of abundance. Other TMOs such as manganese (iv) oxide and titanium (iv) oxide are relatively abundant and environmentally friendly but are performance limited.

As reported in literature, harvesting high performance energy storage devices involves a combination of specific surface area (for high capacitance), pore-size distribution (for easy electrolyte access), electronic conductivity (for improved capacitance and high power)[20]. Typically, a combination of active materials offering these properties with binders is often used in the electrode fabrication process. Asides the environmental concerns on the use of binders, they can be detrimental to the capacitive performance of EDLC[21]. The work reported herein focuses on the water-assisted synthesis of nanomaterials and the investigation of their electrochemical performance in Li-ion batteries and supercapacitors.

1.2. Research Motivation

An increase in the energy demand of a fast-growing world population is one of the global challenges faced by the energy industries. Despite the large production of natural gas, petroleum, coal and other fuel sources, these energy demands are not entirely met but rather raised environmental concerns of greenhouse gases emission. Due to this problem, the energy industry requires economically viable technological innovations to level up the energy deficiency and store energy, considering environmental protection.

The driving force of this research is the green synthesis, modification and processing of 2D nanomaterials as an effective solution to the world problem of low energy demands and environmental pollution. Exploiting these exciting properties of 2D materials and their functionalisation through a continuous hydrothermal flow synthesis method of decorating with highly crystalline inorganic species and doping with heteroatoms provides a promising means to produce nanomaterials with improved capacitive performance.

1.3. Research Aims and Objectives

This PhD research aims to engineer novel and advanced nanomaterials with excellent capacitive charge storage properties through Continuous Hydrothermal Flow Synthesis (CHFS) and optimised conventional synthetic methods. The single-step process of CHFS enables exploration and control of features such as composition, particle size and surface functional properties of MXene and graphene derived materials to obtain desired electrical properties such as life cycle, energy, and power densities.

The specific project objectives are as follows:

- Developing methodologies for the synthesis of MXene, graphene, transition metal oxides and their derivatives through (a) CHFS approach, which allows control and tuneability of material properties, and (b) improved traditional methods (exfoliation and intercalation) in synthesising 2D derivatives to enhance control of synthetic tailoring, improve quality and develop new materials.
- Understanding the properties of the as-synthesised nanomaterials through characterisation to investigate the particle size, morphology, crystallinity, elemental and material compositions etc.
- To fabricate the as-synthesised materials into electrodes for electrochemical analysis. This process involves the formulation of active materials with binders and conductive additives where needed to prepare electrodes.
- To conduct the performance testing of electrodes for electrochemical properties via Cyclic Voltammetry (CV) and Galvanostatic Charge- Discharge (GCD) measurements.

1.4. Novelty of Research

For the first time, 2D Graphene and MXene composite materials were synthesised through a Continuous Hydrothermal Flow Synthesis (CHFS) method and engineered into electrodes for electrochemical energy storage applications. This research combined the single-step synthetic method of CHFS and improved traditional synthetic methods as a strategic way to produce electrode materials (within fraction of a second) and process them for Lithium-ion batteries.

This research paves way for the in-situ production and aqueous processing of functionalised MXene composites with a high electrochemical performance. Through aqueous dispersions as a green route of synthesis in CHFS, these 2D MXene and graphene derivatives were produced with enhanced electrochemical properties.

1.5. Research Structure

Chapter 1 introduces the global concerns on energy and the concept of energy storage. Energy storage devices and their common electrode materials are described with their pros and cons discussed.

Chapter 2 provides background information on several 2D materials explored in this research and the properties they offer. It summarises the different synthetic methods used in 2D material production. It also describes CHFS; a methodology used in this research and its advantages at operating conditions over other synthetic methods are summarised. Furthermore, an in-depth look into electrode materials for energy storage, types of energy storage devices, and their storage mechanisms are described in this chapter.

Chapter 3 describes all the material synthesis techniques used in this research. It outlines the characterisation techniques implored and specifications of the types of equipment used for analysis. The sources of chemicals used as starting precursors and their specifications are provided in detail. In addition, the specifications used in electrode fabrication before electrochemical tests are described.

Chapter 4 describes the processes in the synthesis of N-doped MXene-TiO_2 nanocomposites. The approaches include MXene synthesis from the MAX phase, its post-treatment techniques, and the in-situ production of TiO_2 on the surface of MXene through CHFS. The N-doped MXene-TiO_2 nanocomposites were characterised for surface and chemical analysis and fabricated into electrodes for electrochemical tests.

Chapter 5 gives an in-depth look into the synthesis of MnO_2 and MnO_2-rGO nanocomposites via the CHFS process. The surface and chemical properties of the materials were analysed using several material characterisation techniques. Finally, the materials were further analysed for their electrochemical properties.

Chapter 6 explores the hydrothermal synthesis of TiO_2-reduced graphene oxide nanocomposites in a continuous flow process. The as-synthesised materials were characterised for surface and chemical properties, fabricated into electrodes, and tested for electrochemical performance.

Chapter 7 investigates the delamination process of exfoliated MXenes using a bio-degradable solvent to increase the interlayer spacing and separate them into fewer and smaller MXene sheets. The delaminated MXenes were characterised for surface and chemical properties analysis.

Chapter 8 provides a summary on this doctoral research, drawn conclusions and suggestions for further research on CHFS of 2D materials for energy storage applications.

Chapter 2: Literature Review

The expression “plenty of room at the bottom” was used by Dr. Feynman in 1959, where an emphasis on the power of manipulating and controlling things on a small scale was made[22]. Dr. Feynman’s famous publication motivated a lot of researchers like Frindt in 1966 to explore the scotch-tape method in isolating few layers of MoS_2[23–25]. Exploration of these 2D nanomaterials resurfaced in the 20th century when Geim and co-workers carried out a scotch-tape exfoliation of graphene from graphite during their study on the electronic transport in layers of sp^2 carbon[26]. This mechanical exfoliation method was later repeated in isolating other layered materials[27].

2D materials are single or few-layered materials with an atomic layer thickness of a few nanometres that are obtained either by reducing their corresponding three-dimensional (3D) material through a *top-down* synthesis method or building up from constituent atoms and molecules referred to as the *bottom-up* synthesis method[12]. 2D materials have been studied extensively in different applications such as energy storage[28], optical[29] and biomedical science[30], owing to their ultrathin atomic thickness, high surface area, tuneable physical and chemical properties **(Fig. 2.1)**[12,31]. The atomic thickness and large lateral size of these 2D nanomaterials contribute to their very high specific surface area, making them attractive in surface-related applications such as catalysis and energy storage devices[14]. With strong in-plane covalent bond and atomic thickness, ultrathin 2D materials possess excellent mechanical strength and flexibility, making them suitable in wearable electronics[13]. Also, the atoms on the surfaces of these 2D nanomaterials can be modified and functionalised to control their surface properties and functionalities. This contributes to their processing in certain applications such as solutions for the fabrication of thin-film electrodes and solar cells[32].The 2D plane confines the transport of heat, photon, and charge carriers, generating a significant change in the optical and electronic property of the 2D material[33]. Due to their size reduction, their band gap increases and creates a new property of the material.

2D materials consists of a broad selection of single and combination of elements in the periodic table. This generates heterogeneity in their electronic properties, such as metals, non-metals, metalloids, and semiconductors with direct and indirect bandgaps[33]. 2D materials are explored in the thin film industry, where their compatibility with active technologies facilitates their use in electronic and optoelectronic devices [34–36]. In healthcare applications, the relative large surface area of 2D materials are explored as biosensors, where they act as an active surface sensing element[37]. Furthermore, 2D materials can be tailored to detect specific analytes (e.g., glucose) with high selectivity[38].

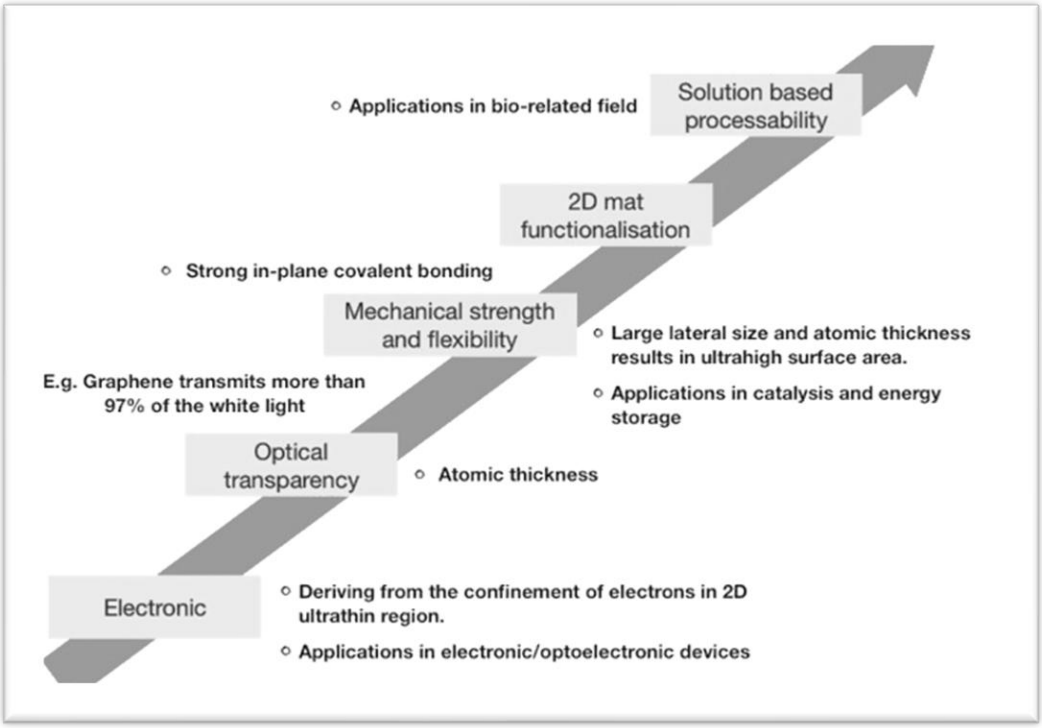

Fig. 2.1 Properties of 2D materials that contributes to their extensive use in several applications[12]

The enormous attention on 2D materials does not rely on its intrinsic properties alone, but also on the tunability of the material. These 2D materials can be tuned via different techniques to enhance the property of the material and meet a specific application requirement. For example, size tuning creates changes to the structure of the material (e.g., an increase or decrease in surface area and defects of the material), causing a change in its electronic/optoelectronic properties[39]. In addition, material properties can also be fine-tuned by varying the particle size and shape, providing use in biomedical applications[40]. Tuning of 2D materials can also include changes to the band gap structure as bulk material is sized down to a single layer 2D material. Intercalation and combination of 2D materials are functionalisation strategies implored in the tuning of 2D materials; the former can significantly cause changes in the electronic properties (transition between metallic and semiconductor transport), and the latter creates a platform to design new 2D materials with enhanced and superior properties[12]. This functionalisation can be achieved by covalent and non-covalent improvement techniques involving surface modification via chemical oxidation or reduction, doping, addition of chemical groups, sonication and exfoliation to facilitate formation into sheets, stable dispersions and enhance their properties for numerous applications[41,42]. Surface functionalisation assists in tuning the properties of a material to achieve a specific function ranging from drug delivery to biosensing, energy storage and other applications[43–45]. Through this means, designing a range of functional 2D materials with superior properties from their parent 2D is feasible **(Fig. 2.2).**

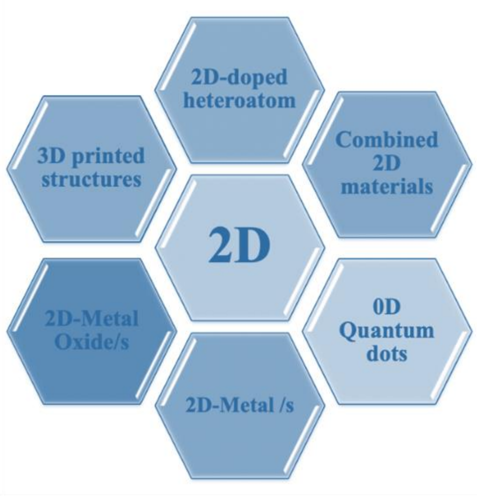

Fig. 2.2 Functionalisation of 2D Materials into target materials for specific applications [46]

According to He and co-workers[47], 2D materials are classified into mono-elemental, dual-elemental, and multi-elemental 2D materials consisting of one element, two elements, and more than two elements, respectively. Mono-elemental 2D materials include semiconducting black phosphorus (BP) composed of the layers of phosphorus atoms covalently bonded together with Van der Waals interaction between the layers. Other mono-elemental 2D materials include graphene, silicone, antimonene, and bismuthene. Dual-elemental 2D materials include transition metal dichalcogenides (TMDs) such as molybdenum disulfide (MoS_2). In MoS_2, there is a covalent bond between Mo and S atoms and weaker Van der Waals interaction between S atoms making it easy to obtain a few layers by mechanical exfoliation. Another dual-elemental 2D material is boron nitride (BN), MXenes such as Ti_2C and Ti_3C_2. Multi-elemental 2D materials include other MXenes such as $(Ti, V)_2C$[48]. The structure of these 2D materials of interest in this research project is shown in **Fig. 2.3**.

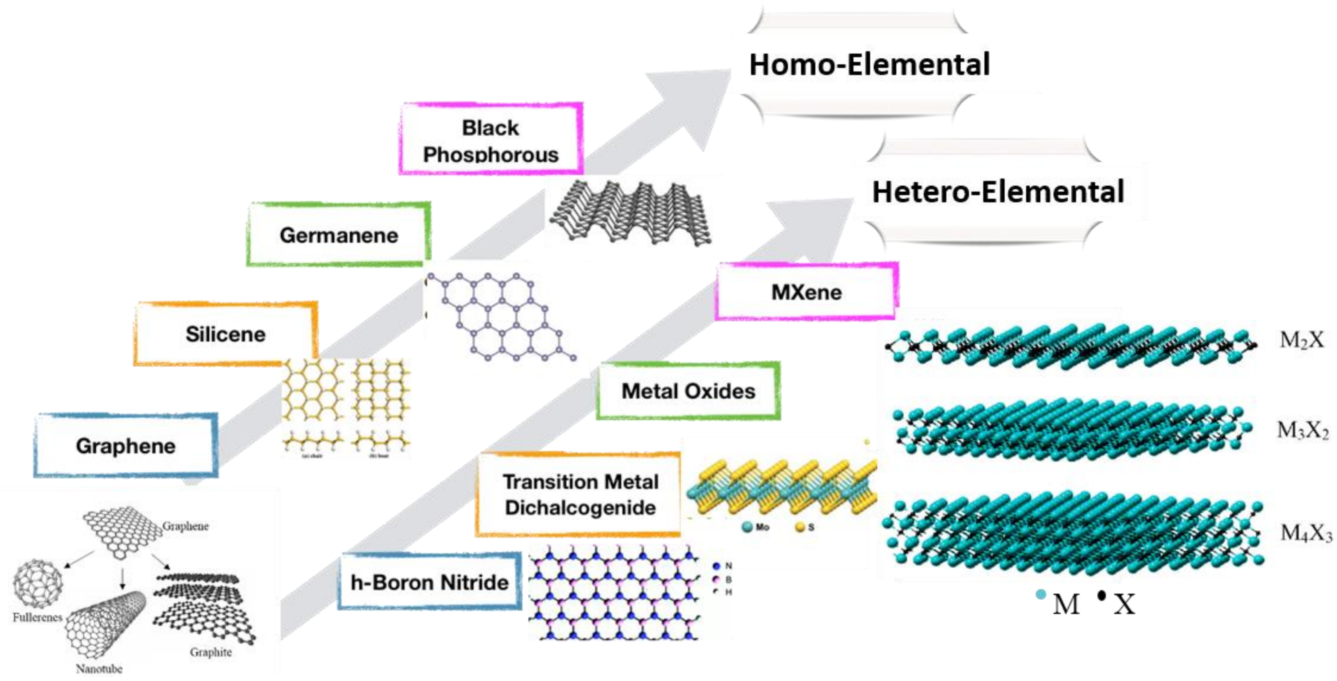

Fig. 2.3 Classification of 2D materials and their respective stuctures[12,49,50]

These layered materials have strong in-plane covalent or ionic bonding and weak interlayer Van der Waals interaction between the layers; facilitating their exfoliation into few and single-layered nanosheets[33]. Exfoliation of these 2D nanostructures from their bulk counterparts can be induced by mechanical or liquid exfoliation[51]. Mechanical exfoliation involves techniques such as the scotch-tape method and sonication of bulk phases with Van der Waals layered structure to induce separation into mono and few layered nanosheets. In materials such as germanene and silicene, they do not have Van der Waals interaction between the layers, and show stable inter-atomic bonding through sp^3 hybridisation. As such, chemical methods are implored to successfully exfoliate the layered structures of germanene and silicene into mono and few-layered sheets[52,53].

2.1. Graphene and its Nanocomposites

Graphene is a flat monolayer of aromatic sp^2 carbon atoms tightly packed into a 2D honeycomb lattice. Graphene transforms into other dimensions such as 0D, 1D and 3D, fullerenes or quantum dots, nanotubes and graphite, respectively[54]. Graphene serves as a building block for these dimensions of graphitic materials. The successful preparation of monolayer graphene occurred in 2004[26], which created a remarkable thread in the experimental and theoretical investigation of the properties of graphene and its range of applications. Following the novel exfoliation of graphene from graphite, several efforts have been deployed into controlling the growth of monolayer graphene.

Graphene has exciting electronic properties, which has made its research in the electrochemical industry very promising. Graphene is a zero-band semiconductor due to the overlapping nature of its valence and conducting bands. With a high theoretical specific surface area of approximately 2630 m^2 g^{-1}, graphene provides an electrochemical double layer gravimetric capacitance of about 550 F g^{-1} [55]. In addition, graphene has charge mobility of 200,000 cm^2 V^{-1} s^{-1}, making it a suitable material for optoelectronic devices [17,56]. Despite these exciting properties of graphene, restacking and the hydrophobic nature affect its application in specific fields such as biomedicine and its processibility in an aqueous medium. This limitation is due to Van der Waal interactions and π-π stacking between its aromatic rings, making graphene form aggregates in solution[31]. This behaviour could affect its function in areas of biomedical science such as drug deliverability, bio-sensing and bio-imaging. According to Zhang and co-workers[57], graphene exhibits hydrophobicity unless it is oxidisable, such as graphene oxide (GO). As a result, graphene use in specific applications requires the addition of polymers or surfactants to be stable in aqueous solutions. Despite these limitations, graphene offers excellent mechanical, electronic and surface properties, making graphene a suitable substrate to decorate various transition metal oxides in the synthesis of graphene-based nanocomposites for lithium-ion batteries (LiBs).

2.1.1 Graphene-MnO_2 Nanocomposites

Transition metal oxides (TMOs) are attractive materials in energy storage applications owing to their high specific capacitance, stability, and good charge-discharge performance over a wide potential window. Many transition metal oxides have been explored for their electrochemical activities, with ruthenium oxide showing the highest electrochemical performance of 760 F g^{-1} [58]. However, ruthenium oxide as an electrode material is limited by its cost and toxicity, making the technology not economically feasible. Other TMOs such as manganese (IV) oxide and titanium (IV) oxide have gained more interest due to their excellent electrochemical performance, natural abundance at a low cost and no environmental concerns.

Manganese (IV) oxide (MnO_2) is a transition metal oxide with high energy density and making it suitable for application as components of electrode materials for energy storage devices. It is naturally abundant at a low cost with no environmental concerns[59]. MnO_2 is a promising electrode material in different energy storage systems such as metal-ion batteries, alkaline batteries, and supercapacitors due to its high specific capacity and environmental friendliness[60]. MnO_2 is a non-stoichiometric compound with an oxidation state of +4, and existing in various polymorphs such as hollandite (α), pyrolusite (β), nsutite (γ), ramsdellite (R) and birnessite (δ) (**Fig. 2.4)**[61]**.**

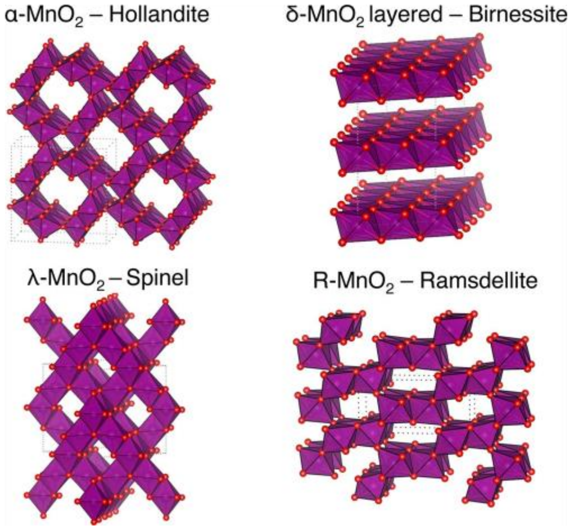

Fig. 2.4 Structures of MnO_2 polymorphs[62]

Despite the exciting properties exhibited by MnO_2, it is limited by poor electrical conductivity. The theoretical specific capacitance of MnO_2 reaches 1370 F g^{-1} as the oxidation state of Mn^+ changes from +4 to +3 over a potential window of 0.8 V[58]. However, this high theoretical value has not been matched up by research data as reported values are below 200 F g^{-1}[63–66]. Over the years, several research works have explored strategies to improve the capacitance and conductivity of MnO_2. These strategies include fabricating synthetic methods to enhance surface area with desired crystal structure, combining MnO_2 with conductive materials such as graphene[67], carbon nanotubes[68] and conductive polymers[69]. In addition, increasing the interlayer distance of layered MnO_2 by metal cation doping[70] also improve its electrochemical performance.

Graphene can be combined with organic and inorganic materials such as graphene/metal oxides[71], graphene/metals[72], graphene/carbon-based materials[73] and graphene/polymers[74]. Due to their excellent electrochemical activity and faradaic redox reaction, transition metal oxides and conducting polymers are explorable as electrode materials in energy storage devices[75]. Carbon-based materials like carbon nanotubes (CNTs) and graphite exhibit good electrical conductivity that provides superior electrochemical performance of the nanocomposites owing to their exceptional surface area and porous structure, compared to only graphene-based electrodes[76]. Graphene-based supercapacitors showed a specific capacitance of 75 F g^{-1}, 99 F g^{-1}, 117 F g^{-1} and 135 F g^{-1} ionic liquid, organic, aqueous H_2SO_4 and aqueous KOH electrolytes respectively[77,78].

MnO_2 is a transition metal oxide that exhibit significant faradaic reactions occurring at the electrode surface. Several reports have been on the synthesis of different morphologies of MnO_2; needles, rods and birnessite, amongst others, on the surface of graphene sheets. MnO_2 energy storage mechanisms include reversible redox processes, cation adsorption-desorption and ion intercalation[79]. MnO_2 /Graphene (Gr) nanocomposites combine the electric double-layer capacitance of graphene and the pseudocapacitance of MnO_2 to obtain improved capacitance values compared to graphene-based electrodes.

The process dependent synthesis of MnO_2 /Gr by decorating graphene oxide (GO) with MnO_2 followed by reduction with hydrazine hydrate was reported by Kim and co-workers with a specific capacitance value of 328 F g^{-1} at a scan rate of 10 mV s^{-1} was obtained[59]. Other works have also been done, such as the dispersion of MnO_2 needles on the surface of GO. Still, a low value of capacitance was obtained (197 F g^{-1}) due to limited electronically conductive channels[59,80].

The electrochemical performance of MnO_2 depends on the synthesis condition, type of morphology, crystallinity, and particle size[81]. The physical and chemical properties of MnO_2 are affected by its method of synthesis. As a result, several methodologies such as microwave synthesis[82], Ultrasound synthesis[83], and hydrothermal synthesis[63] have been explored to offer advantages in morphology variation, porosity, pore size distribution, higher resource and energy efficiency.

Enhancing the electrochemical performance of MnO_2 /Gr electrodes is achievable through a novel continuous hydrothermal synthesis of MnO_2/Gr nanocomposite. This research introduces this synthetic process to produce homogeneously dispersed MnO_2 nanoparticles on the surface of graphene sheets in a single step, thereby enabling better electrical conductivity of graphene, increased surface area, and decreased diffusion path, increasing the pseudocapacitive reaction and offering much-improved capacitance.

2.1.2. Graphene-TiO_2 Nanocomposites

TiO_2 is a naturally abundant TMO with advantages such as low toxicity, reasonable cycling rate, fast ionic transport and high theoretical capacity (335 mA h g^{-1})[84]. These properties make it a promising material for energy storage applications. TiO_2 exists in three common polymorphs (anatase, rutile and brookite) as shown in **Fig. 2.5**, with anatase the most extensively studied polymorph for energy storage[85]. Anatase TiO_2 has a tetragonal crystal structure with the space group I_{41}/amd. A unit cell consists of four distorted TiO_6 octahedrons and four distorted oxygen octahedral vacancies where lithium ions are inserted during lithiation[85]. TiO_2 has been explored in different applications such as photocatalysis[86] and energy storage[87].

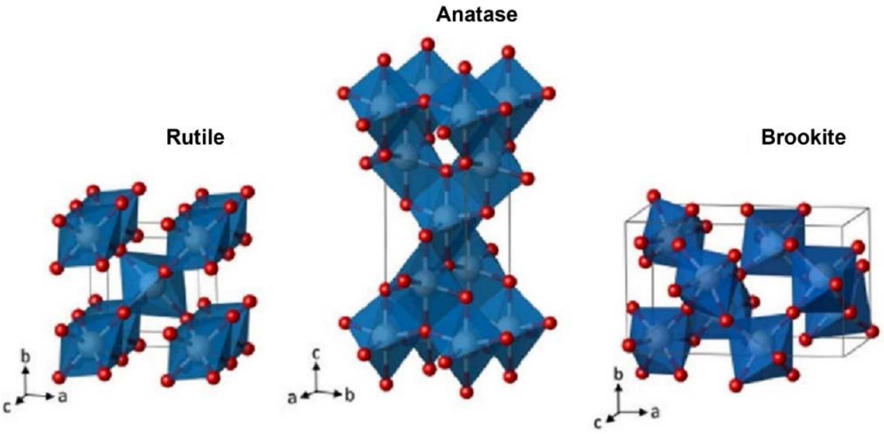

Fig. 2.5 Structures of TiO_2 polymorphs[88]

Several approaches have been made towards improving the application of TiO_2 for energy storage. These include doping with metal ions[89], tuning at the nanoscale to vary morphologies[90,91] and mixing with carbonaceous materials such as graphene and nanotubes to form composites with superior electrochemical properties[92]. For example, carbon-coated TiO_2 hollow spheres were prepared by Zhang and co-workers and applied as an anode material for sodium-ion batteries. The battery showed excellent cycling stability and a reversible capacity of 140 mA h g^{-1} after 500 cycles[93]. Changsheng et al (2015) prepared a TiO_2-C based anode for sodium-ion batteries that delivered a good cycling performance and a reversible discharge capacity of 275 mA h g^{-1}[94]. Furthermore, on graphene-TiO_2 research, reduced graphene oxide (rGO)-TiO_2 nanotubes were prepared by Peng Zheng et al (2016) for lithium-ion batteries. The rGO-TiO_2 nanocomposites showed a remarkable capacity of 263 mA h g^{-1} at 0.1 A g^{-1} after 100 cycles[95].

TiO_2-graphene nanoparticles have been synthesised through different routes such as hydrothermal[96], solvothermal[97], microwave-assisted technique[71] and chemical methods[98].

2.2. MXenes and its Nanocomposites

MXenes are transition metal carbides, carbonitrides and nitrides obtained by selectively etching out the A element from its MAX phase precursor[48,99]. MAX phase is a bulk material where M stands for early transition metal (such as Ti, V, Cr, etc.), A is a group IIIA or group IVA element (such as Al or Ga), and X is a carbon (C) or carbonitride (CN) or nitride (N). MXenes have a general formula of $M_{n+1}X_nT_x$, where n = 1, 2 or 3, T_x = surface terminations such as O, OH or F, and x is the number of surface terminations **(Fig. 2.6)**[48]. About 19 different MXene compositions have been synthesised, and several have been predicted to exist (*ca.* 60). Some examples are $Ti_3C_2T_x$, Ti_2CT_x, Ti_3CNT_x, $Nb_4C_3T_x$ etc[48]. MXenes exhibit a sandwich-like arrangement where n+1 layers of M cover n layers of X, i.e. $[MX]_n M$. $Ti_3C_2T_x$ is the most studied MXene with high electronic conductivity of about 9880 S cm^{-1} and excellent charge-storage properties[100]. MXenes with more than one M element exists in random and ordered arrangements of M atoms. When there is a random arrangement of two different transition metals in the M layers, it is a solid solution. On the other hand, when the different M atoms are orderly in the M layer, it is called an ordered phase[48]. MXenes are implored in numerous applications such as electrochemical energy storage, transport conductors, water desalination, antibacterial films, coatings and biosensors[57].

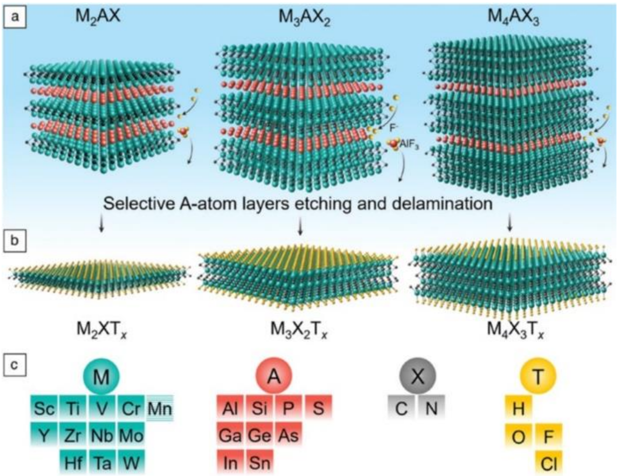

Fig. 2.6 MXene synthesis from their precursors (a) Different MAX phases structures (b) Post-etch MXene structure with surface terminations (c) Elements present in MAX and MXene phases[101]

MXene is hydrophilic and has a higher electronic conductivity, allowing its electrode to be used as both the active material and current collector in supercapacitors[48]. MXenes also exhibit a pseudo-capacitance through reversible redox reactions occurring at the Ti surface. MXene nanosheets have a negative charge that allows the formation of stable, viscous aqueous colloidal solution without the addition of surfactant and polymer[48,57,102]. In addition, MXene has a higher tap density of about 4 g cm^{-3} than graphene, which has a tap density of about 0.4 g cm^{-3}. This property contributes to a higher areal or volumetric capacitance. MXene films can have a high volumetric capacitance of 900 F cm^{-3} [103]. These show an increasing interest in the application of MXenes in energy storage devices.

2.2.1. MXene-TiO_2 Nanocomposites

Reinforcement of materials with MXene improves its mechanical and electronic properties. Such materials include carbon-based nanomaterials such as CNTs[104], mesoporous carbon[105] and graphene[106]. Other reinforcements include polymers[107] and transition metal oxides[108]. The formation of MXene hybrids with these materials help prevent restacking of MXene sheets, aids flexibility, improves conductivity, and increases electrochemical performance[109].

MXene have gained increased attention in energy storage research. The characteristics of a good energy storage device includes high storage capacity, excellent cyclability and rate capability. All these device properties rely on the composition and properties of the electrode material. Graphite is a common anode material used in lithium-ion batteries but suffers from low specific capacity and impaired rate performance. This challenge paved way for the development of improved anode materials with MXene-based compositions[110,111].

MXene-TiO_2 composites have been reported in the literature for different applications. Jingxiang Low et al. (2018) synthesised TiO_2 nanoparticles grown on the surface of highly conductive MXenes via a calcination method for the photocatalytic reduction of CO_2[112]. Therein, the MXene-TiO_2 composites showed up to 3.7 times higher photocatalytic CO_2 reduction for methane production (0.22 μmol h^{-1} than commercial TiO_2). For energy storage, JianFeng and co-workers prepared MXene-TiO_2 nanocomposites through an in-situ hydrolysis and heat treatment method. The as-synthesised composites showed a good electrochemical performance of 143 F g^{-1} at 5 mV s^{-1}, with excellent cycling stability after 6000 cycles[113]. Furthermore, MXene-TiO_2 composites can be surface-functionalised and employed as an electrocatalyst in the hydrogen evolution reaction (HER), as described[114]. The as-prepared electrocatalyst showed improved HER performance of 190 mV at 10 mA cm^{-2}. This enhanced performance was attributed to the functionalisation of the basal planes of MXenes with O active sites.

The novel properties of these 2D nanomaterials are attainable depending on the route of synthesis implored to offer unique characteristics such as a high surface area to volume ratio, distinct morphologies, and surface functionalities. The following section will briefly overview 2D materials of interest for this research project.

2.3. Synthetic Strategies of 2D Materials

The novel properties of these 2D materials have been the driving force in the continuous research development of superior materials for use in a variety of applications. The physical and chemical properties of a material are dependent on the synthetic strategy employed. 2D materials are synthesised via different methods which are classified distinctively according to the processes involved in creating nanometre sized structures. These are the top-down and bottom-up synthesis.

2.3.1. Top-down Synthesis

Top-down synthesis involves the exfoliation of 3D bulk materials into 2D materials by mechanical vibration or chemical reactions. The former employs mechanical energy such as ultrasonication and mechanical (scotch tape) exfoliation to separate layered solids into single or few-layer 2D materials.

Mechanical exfoliation and Ultrasonication

The process of mechanical exfoliation involves generating a physical interaction between the material and the source of mechanical force. This process is followed by the application of the required force to remove Van der Waal force- bounded layers. **Fig. 2.7 (a & b)** shows the illustration of mechanical exfoliation and ultrasonic exfoliation, respectively.

The synthetic techniques of mechanical exfoliation and ultrasonication offer advantages but have their limitations. For example, low-cost mechanical exfoliation (such as vigorous handshaking) separates layered solids into only one or a few-layer nanosheet which helps preserve the crystal structure and properties of the material. The convenience of this method can produce large-size ultra-thin nanosheets[115]. However, this method is limited to layered Van der Waals solids like graphene and molybdenum disulphide. The ease of this method makes it convenient for small scale production in laboratory research but cannot be scaled up for industrial production[115].

Another mechanical exfoliation technique is the Scotch-tape method. In 2004, Geim and Novoselov exfoliated graphite (three-dimensional bulk precursor) into single-layer graphene using the scotch-tape method[26]. This technique involves the use of mechanical force repeatedly to separate graphite (layer by layer) from scotch-tape, thereby thinning the graphitic layer until one single-layer graphene is obtained (**Fig. 2.7a**).

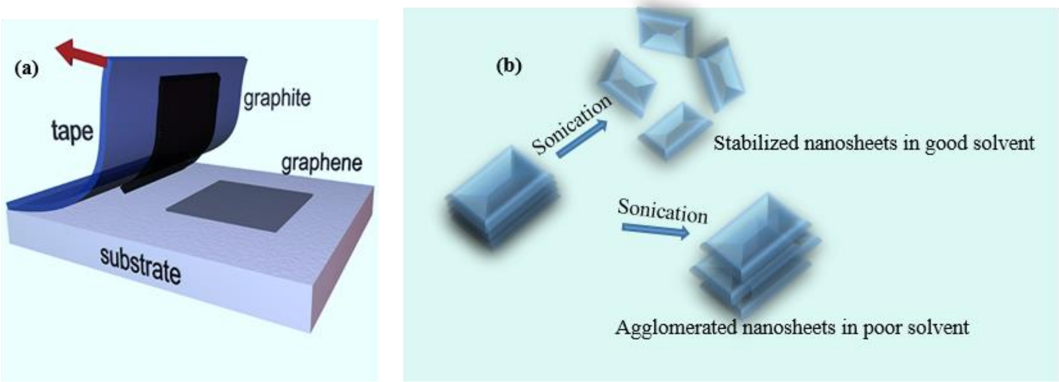

Fig. 2.7 (a) Micromechanical exfoliation techniques via Scotch tape[26,116] and **(b)** solvent-assisted exfoliation[115].

Ultrasonication is also applicable in exfoliating layered solids into single or few-layered nanosheets and offers a more effective, scalable, and productive exfoliation. However, the effectiveness of this process depends on the duration of sonication and the dispersed solvent. Nanosheets stabilise in suitable solvents and agglomerate or from sediments in poor solvents, a property dependent on the surface energies of the solvent used[115]. Examples of solvents used in ultrasonication include de-ionised water, methanol, isopropanol, dimethyl sulfoxide (DMSO), acetone, etc.[115].

The use of ultrasonic energy has been demonstrated in the synthesis of SnO$_2$ - nanoparticles[117]; SnO$_2$ nanoparticles (8-30 nm) were synthesised at room temperature. An increment in sonication time was also found to have caused a decrease in particle size, an increase in surface area and a change in morphology. Besides affecting particle size, surface area and morphology, ultrasonication also aids in the delamination of 2D materials into single 2D sheets. This ultrasonic method was employed as a precipitation assisted technique in the nanomaterial synthesis process[117]. The production of single-layer 2D material via ultrasonication was reported by Manish Chhowala and co-workers as described[118,119].

Therein, a lithium intercalation strategy was employed that involved the formation of a lithium-intercalated compound, followed by an ultrasonication process to generate 2D nanosheets. As described by Zhang *et al.* [120], in the isolation of ultra-thin MoS_2 nanosheets, lithium is intercalated into the layered material via a galvanostatic discharge process at a current density. The electrolyte is then removed by washing the intercalated compound with a suitable solvent. After washing, the slurry is exfoliated by ultrasonication in water or ethanol and centrifuged to separate unexfoliated materials and collect monolayer ultra-thin 2D nanosheets. Atomic force microscopy (AFM) measurements showed a thickness of 1 nm in as-synthesised monolayer MoS_2 nanosheets. Selected area electron diffraction pattern (SAED) of MoS_2 showed single crystal hexagonal diffraction pattern that also confirmed monolayer MoS_2 sheets[120].

Furthermore, chemical exfoliation and ultrasonication can be adopted to synthesise single or few-layer thick MXenes (**Fig. 2.7b**) through acid-assisted bulk MAX phase material exfoliation into multi-layered MXene, which is further separated through ultrasonication[115].

Ball milling

Another example of a top-down synthetic strategy is the ball-milling method. This method consists of tungsten carbide or silicon carbide balls and a stainless-steel mill chamber where the balls rotate inside. A pulling force on the material is provided by a magnet placed outside the mill chamber; this magnetic force increases as the chamber rotates. This method is inexpensive and creates uniformly fined nano powders with sizes dependent on the speed of rotation. An advantage of this techniques is its application on a range of materials like metal oxides, cellulose, polymers, catalysts etc. However, nanomaterial may have crystal defects due to the forces involved and may be contaminated by ball and milling additives[121]. Three types of ball mills exist: tumbler, planetary and vibrational **(Fig. 2.8)**.

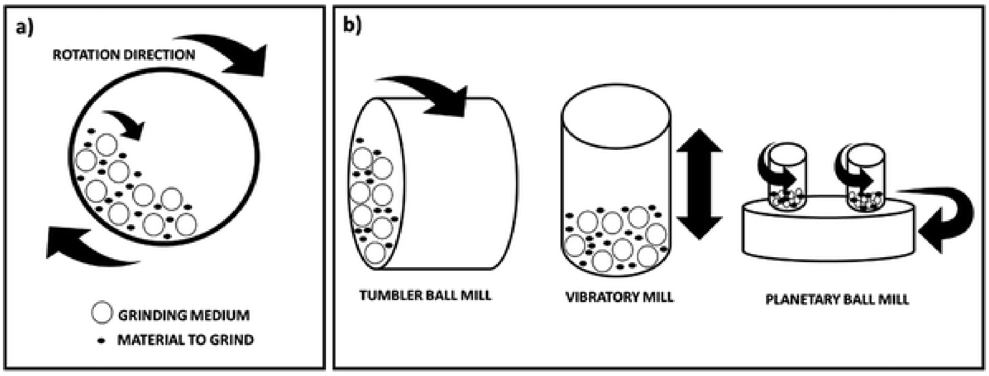

Fig. 2.8 Representation of the different ball mill types[121]

The tumbler ball mill is a cylindrical vessel loaded with a limited amount of stainless steel balls rotating along its direction of length. The larger the diameter of the tumbler ball mill vessel, the more efficient the milling process. The vibrational mill has a cylindrical vessel wherein the sample and the balls are placed and shaken at high frequencies (direction shown in **Fig. 2.8b**). In the planetary mill, a rotating disk is used to suspend and rotate each vessel around its axis [121].

Structure, morphology, crystallinity, and thermal stability are properties of the material often impacted by the ball milling process. The ball milling method has been used in the synthesis of cellulose nano derivatives, where a morphology change was observed in microcrystalline cellulose[122]. Furthermore, crystallinity, thermal stability and morphology of cellulose were reported by Amir and co-workers, where cellulose showed a decrease in crystallinity, thermal stability, and a change in morphology[123].

As a top-down strategy, wet ball milling was used with *N*, *N*- dimethylformamide (DMF) to exfoliate graphite to graphene sheets. After centrifugation (post ball milling), the synthesised graphene sheets obtained from the supernatant were single and few-layered with a thickness between 0.8-1.8 nm[124]. Another example of the remarkable research on ball milling as a synthetic strategy in 2D materials production was reported by Zhao et al. (2015). Therein, MoS_2-C (30 % C) nanocomposites were prepared as an anode material for lithium-ion batteries and showed a high discharge capacity of 720 mA h g^{-1} after 200 cycles at a current density of 100 mA. In addition, the anode material showed high Coulombic efficiency and also achieved a reversible capacity of 428 mA h g^{-1} at a current density of 2000 mA h g^{-1}. Compared to a MoS_2-C composite (20 % C), the enhanced performance was accredited to the synergistic effect of carbon coating and nano crystallisation achieved in the ball milling process[125].

Chemical exfoliation

Chemical exfoliation of bulk phase material occurs by either ion exchange, ion intercalation or application of heat. Generally, chemical exfoliation is adopted as an easier route for large scale production and when stronger intermolecular forces are present between the atoms in the material, which makes mechanical exfoliation ineffective. This can be seen in the bulk MAX phase precursor, which possesses metallic bonds between the M element (Ti) and Al element (Al or Ga), and a covalent bond between the M and X element.

Gogotsi and co-workers first reported the successful extraction of Al from Ti_3AlC_2 MAX phase to form Ti_3C_2 MXene in 2011[99]. Therein, a solution of hydrofluoric acid was used as the etchant to selectively remove Al layers. Chemicals can selectively etch A layers without disrupting the M-X bonds[126]. The removal of A layers enables easier separation of MX layers due to weakened interactions. Three reactions occur during the etching process as shown in eqs. (1-3).

$$Ti_3AlC_2 + 3HF = AlF_3 + 3/2\ H_2 + Ti_3C_2 \qquad (1)$$

$$Ti_3C_2 + 2H_2O = Ti_3C_2(OH)_2 + H_2 \qquad (2)$$

$$Ti_3C_2 + 2HF = Ti_3C_2F_2 + H_2 \qquad (3)$$

Eq. 1 describes the addition of the etchant and removal of Al layer to produce Ti_3C_2 MXenes. **Eq(s). 2 and 3** describes the subsequent terminations (OH and F groups) formed on the surface of 2D MXenes due to the fluorine and hydroxyl- rich aqueous environment of exfoliation reaction[99].

A mechanical vibration such as a vortex mixer can easily separate the as-etched material into single or few layers depending on the type of chemical etchant used. The quality of the as-synthesised nanosheets depends on etching conditions such as nature of etchant used, the concentration of etchant and duration of the etching process[99,126].

An example is the etching of MAX precursor with lithium fluoride in hydrochloric acid (LiF/HCl) solution to obtain larger MXene flakes compared to smaller flakes obtained when anhydrous HF is used[48]. The area of application for the layered 2D material determines the type of etchant to be used. Electrochemical energy storage applications would prefer larger flakes to enhance fast charge transport between the layers[48,57].

On the other hand, graphene is synthesised through the modified Hummers method involving the initial oxidation of graphite to graphitic oxide, followed by chemical exfoliation into graphene oxide sheets[127]. These GO sheets are reduced by chemicals such as hydrazine (N_2H_4) or potassium hydroxide (KOH) to produce reduced graphene oxide (rGO) or graphene sheets as described below.

Reduction of Graphite Oxide (GO)

In 1958, William S. Hummers Jr., and Richard E. Offeman published an article on the preparation of graphitic oxide from graphite[128]. This synthetic method is famously referred to as the Hummers' method. This wet-chemical method is widely used in the synthesis of graphene because of its scalability, solvent compatibility and high yield, making it easily processed for several applications.

Hummers' method involves the treatment of graphite powder with a mixture of sodium nitrate ($NaNO_3$), potassium permanganate ($KMnO_4$) and sulfuric acid (H_2SO_4). Firstly, a mixture of sodium nitrate and sulfuric acid is made (generating nitric acid in-situ for safe handling). Graphite is added to the mix, where sulfuric acid molecules diffuse between graphitic layers and expand the layers during the process. This is followed by introducing the oxidising agent ($KMnO_4$) in small amounts (to control the temperature of the reaction). The oxidation step introduces defects in the form of holes in the graphene structure, affecting the quality and subsequently the properties of the material[128]. Over the years, modifications to the Hummers' method have been made to replace sodium nitrate, thus eliminating the production of toxic nitric gas[129].

After the synthesis of GO, the surface of GO is treated with a reducing agent to eliminate oxygen functionalities created during the oxidation step. This reduction process can be used to functionalise graphene (e.g. heteroatom doping of the graphene structure) if desired by using reducing agents such as hydrazine[130]. Otherwise, reducing agents with carbon, hydrogen and oxygen compositions (e.g. ascorbic acid) can be used to avoid undesired doping[131]. After the reduction step, the as-synthesised graphene material is referred to as reduced-graphene oxide (rGO). **Fig. 2.9a** below shows the chemical structures of graphene, GO and rGO, and **Fig. 2.9b** shows the schematic illustration of the chemical reduction process of graphite to rGO.

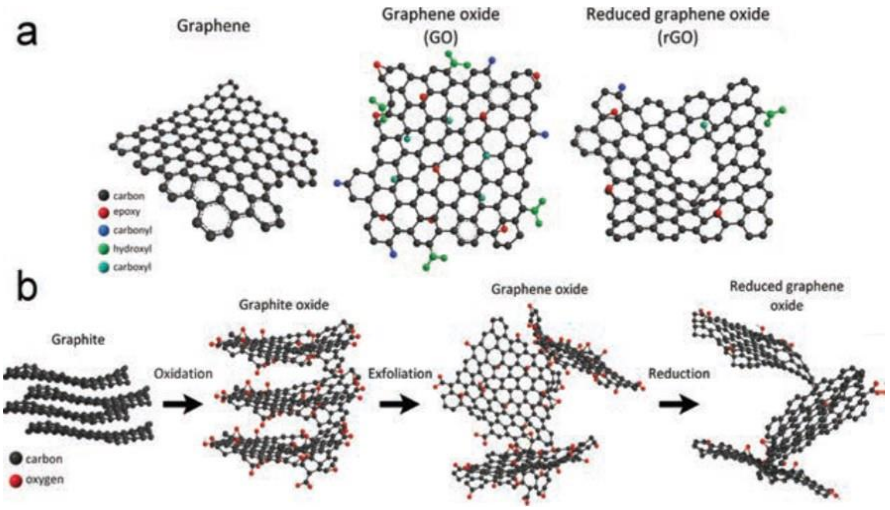

Fig. 2.9 (a) Chemical structures of graphene, GO and rGO **(b)** Schematic showing rGO synthesis route from graphite[132]

2.3.2. Bottom-up Synthesis

This involves synthesising nanoscale materials from constituent atoms or molecules that react, nucleate, and grow into complex structures. This method offers an advantage of mass production and high yield over previously stated exfoliation methods. In addition, exfoliated methods as described above are only suitable for layered bulk precursors. An example of the bottom-up synthesis includes the wet chemical strategy, microwave-assisted strategy, topochemical transformation and chemical vapour deposition (CVD)[115]. Each of these has its respective synthesis routes for preparing certain 2D materials like graphene, MoS2, nanocomposites, etc.

Wet chemical strategy

Due to the low cost and high yield of this method, it is favourable for the synthesis of various 2D materials. This strategy includes hydro/solvothermal synthesis and template synthesis techniques. The former will be discussed later in this chapter.

Template synthesis

Template synthesis involves adjusting the morphology of a template by growing crystals of specific sizes, followed by removing the template via temperature or pH adjustments[115]. Quantum dots (0D), nanowires (1D), and non-layered 2D materials such as α–Fe_2O_3 semiconductor nanosheets can be synthesised using this method of bottom-up synthesis (illustrated in **Fig. 2.10**).

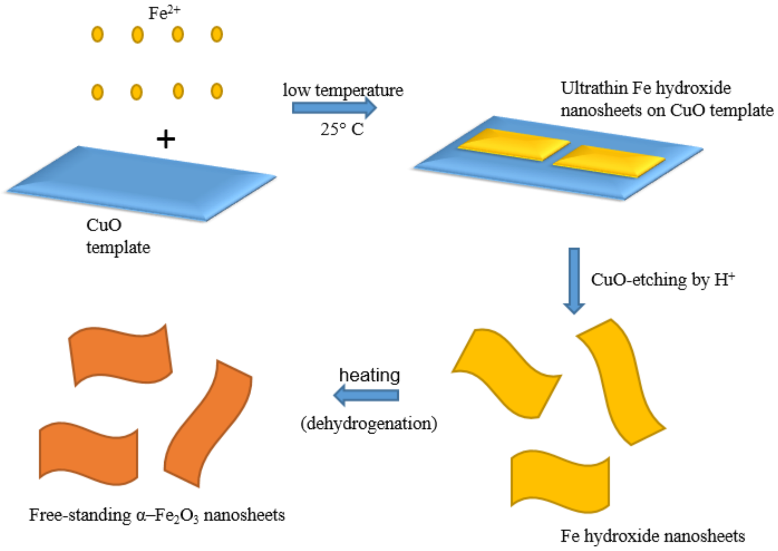

Fig. 2.10 Template synthesis schematic of α–Fe_2O_3 nanosheets as a bottom-up synthesis approach[115]

Microwave-assisted synthesis

This method is often used to promote chemical reactions. It involves treating the starting materials under microwave irradiation. The reaction is performed in a microwave reactor at a set operating power for a short period of time (typically for a few minutes). The product is collected, centrifuged, washed with water and ethanol, and dried to obtain ultrathin nanomaterials. Zhou and co-workers explored a large scale synthesis of ultrathin α- $Ni(OH)_2$ through a microwave-assisted liquid phase growth[133]. The as-synthesized $Ni(OH)_2$ nanosheets had a thickness of less than 2 nm, and showed enhanced electrochemical performance with a specific capacitance of 4173 F g^{-1} at a current density of 1 A g^{-1}. Hasanpoor and co-workers also reported the effects of changing reaction time, type of precursor and irradiation power in the microwave-assisted synthesis of ZnO nanoparticles. As these operation parameters were varied, a change in morphology and particle size of ZnO nanoparticles were observed[134].

Topochemical transformation

Exfoliation and chemical methods offer better processing and higher yields. However, exfoliation is limited to layered compounds with Van der Waals interactions. The topochemical strategy involves the structural modification of a host material by introducing guest species into the host material structure [135]. This is observed in the acid-assisted exfoliation of MAX phase precursors to MXenes[18,48,102,136]. In addition, the delamination process of multi-layered MXenes to single or few-layered MXenes via the insertion of guest organic molecules (e.g., Urea, DMSO) is a topochemical transformation strategy employed in 2D material research. Different guest molecules make different structural modifications to the delaminated MXenes by changing the c-lattice parameter (c-LP) from 19.5 Å to 25.5 Å after insertion of hydrazine[135].

Chemical Vapor Deposition (CVD)

As the name implies, this technique involves vaporising the material precursor and introducing it along with a carrier gas into a tube furnace **(Fig. 2.11)**. The material is deposited on the substrate that is placed inside the tube furnace. CVD process produces highly pure 2D nanomaterials with controllable thickness, morphology and crystallinity by tuning the reaction process parameters[115]. These parameters include precursor type, reaction temperature, substrate type and pressure[137].

During the CVD process, thermal decomposition, chemical synthesis, and chemical transport of precursor are the reactions occurring. As a result, a gaseous precursor provides control on the number of molecules involved by tuning its flow rate and partial pressure. This can be observed in the CVD process of graphene, where CH_4 and H_2 are used as the gaseous precursors to control the flow rate of precursors and concurrently control graphene's size, structure, and morphology. CVD can also be explored as a strategy in the functionalisation of these 2D materials. For example, introducing another gaseous phase, such as NH_3 in the CVD process will produce nitrogen-doped graphene[138].

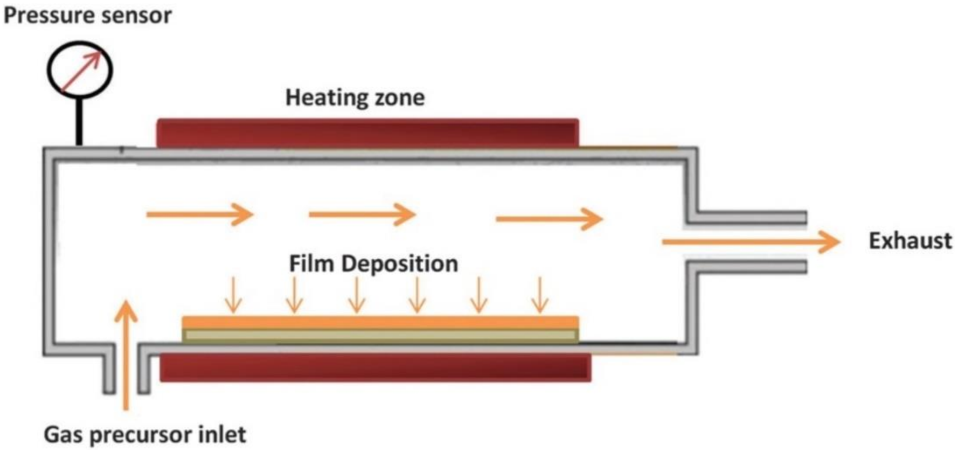

Fig. 2.11 Schematic of CVD process showing the parts of the chamber[139]

Despite the numerous advantages offered by the CVD process, it is hindered by the high temperature and vacuum requirements and specific substrate use[115].

Chemical Vapor Deposition of Graphene (CVD)

This method involves the vapour phase deposition of a hydrocarbon source on a metal substrate at a high temperature of (1000 °C) under an inert atmosphere[137]. In 1966, CVD on metal substrates was first reported in the growth of graphite films on Ni substrate[140]. Later in 1992, the CVD deposition of a single layer of graphite on Pt substrate was reported[141]. After the isolation of graphene in 2004, CVD has been extensively researched for growing single-layer graphene[142,143]. This method provides a scalable and controllable strategy to grow single or few-layered graphene. In a typical CVD-graphene process **(Fig. 2.12)**, the gaseous hydrocarbon precursor (methane) and carrier gas (hydrogen) are injected into the furnace through the gas inlet channel **(step 1)** and migrate towards the substrate **(steps 2-4)**, where they react in the vapour phase or on the surface of the metal substrate (Ni, Cu), where it is deposited as a continuous film of graphene. CVD-graphene is synthesised in two steps; pyrolytic decomposition of precursor to form disassociated carbon atoms and creation of carbon structure from the disassociated carbon **(steps 5-7)**. These two steps require very high levels of heat, and as a result, metal catalysts such as Cu or Ni must be used to reduce the reaction temperature to about 1000 °C. During the process of deposition, by-products **(step 8)** are also formed which are removed from the furnace through the exhaust outlet channel **(step 9)**.

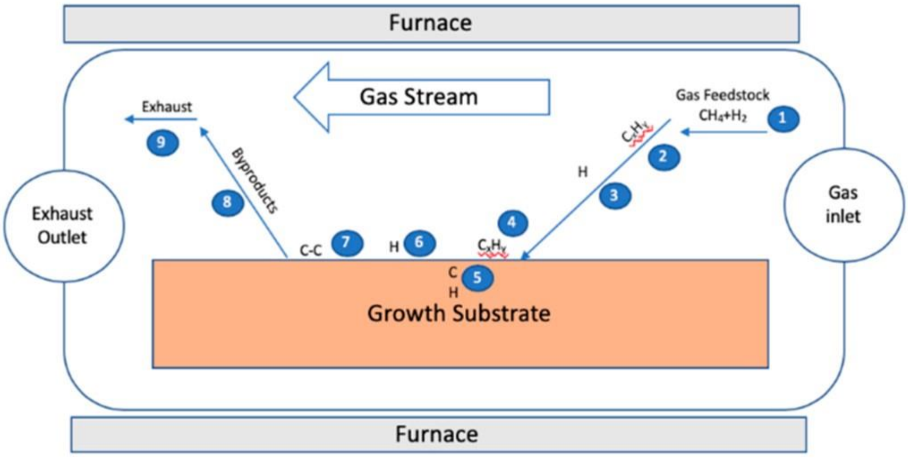

Fig. 2.12 Schematic showing the CVD of graphene films on a metal substrate using methane and hydrogen as hydrocarbon precursor and carrier gas respectively[144]

Ni-assisted[145] and Cu-assisted[146] CVD methods have been reported. However, Cu-assisted CVD generates single layer and defect-free graphene sheets with no substrate boundaries[146]. Sajjad et al. (2014) observed the grain growth of graphene under low-pressure CVD at different hydrogen flow rates. Therein, it was observed that the nucleation and growth of graphene at higher hydrogen flow reduced defects and impurities in the CVD grown graphene films[143]. Another reported work on CVD synthesised graphene is the direct transfer of as-synthesised graphene through CVD to different polymer substrates (polystyrene, polyethene) by applying heat and pressure[147].

Despite the high quality of graphene produced through CVD, it is challenged by the formation of toxic by-products and substrate boundaries. The former raises an environmental concern, while the latter makes it difficult to transfer deposited graphene onto the required substrate. In addition to this, some metal catalysts such as Ni react with the carbon phase at high temperatures, thereby generating unwanted defects in the material and impurities in the form of carbides. This metallic surface interaction with carbon makes scaling up the CVD method not feasible to produce graphene for numerous applications.

Other wet chemical methods

Graphite is naturally abundant. As a result, a wet chemical strategy could be potentially feasible for the large-scale synthesis of graphene. Wet chemical strategy involves the conversion of graphite into an intermediate compound via chemical treatment, followed by the isolation of graphene precursor from the intermediate using other chemical or/and physical methods such as sonication, heating, or microwave irradiation.

Liquid phase exfoliation (LPE)

In the LPE process **(Fig. 2.13)**, graphite is dispersed in a suitable solvent to exfoliate individual layers. The immersion of graphite in the solvent contributes to the weakening of the Van der Waals forces existing between the graphene layers. Graphene has a surface energy of 46.7 mN m^{-1} that makes solvents such as N-methyl pyrrolidone (NMP), N, N'-dimethylformamide (DMF) with surface energies of 40 mN m^{-1} and 37.1 mN m^{-1} respectively suitable for exfoliation of graphite due to the reduction in interfacial tension between the solvent and graphene layer[148]. In 2008, Yenny and co-workers successfully exfoliated graphite in NMP for the first time[149]. The graphene sheets were fabricated to a thin sheet and showed a high conductivity of 6500 S m^{-1}. Despite the success of the LPE process, the yield of graphene obtained is very low (1 %) at a concentration of 0.01 mg ml^{-1}. Higher concentrations of 0.3 mg mL^{-1}, 0.1 mg mL^{-1} and 0.5 mg mL^{-1} were achievable when graphite is dispersed in *ortho*-dichlorobenzene (o-DCB)[150], pentafluorobenzonitrile[151] and benzylamine[152]. However, the flake size obtained was relatively small (<3 µm).

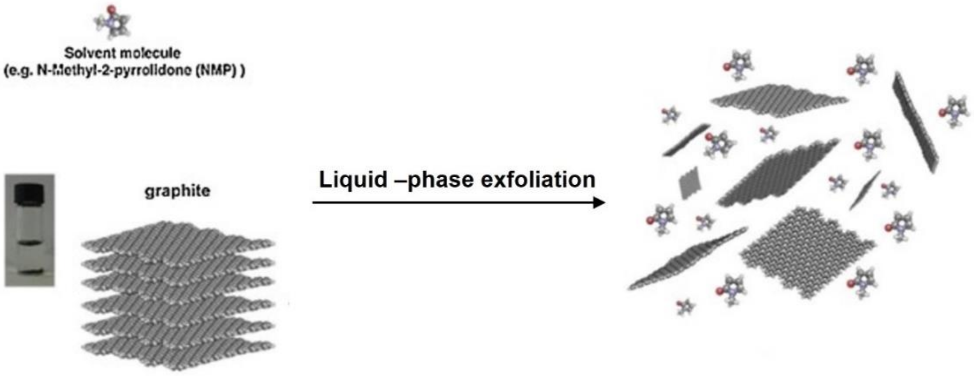

Fig. 2.13 Schematic of LPE process of graphite to produce graphene dispersions through weakening of Van der Waals interactions between graphene layers[153]

These organic solvents, such as NMP, is toxic and raise environmental concerns. Water is a green solvent because it is non-toxic and can be used in thin films fabrication. However, due to the hydrophobic nature of graphene, its dispersibility in water is not attainable, exfoliation of graphene in water is not feasible. The introduction of ionic surfactants can temporarily aid the suspension of graphene sheets in water. Such surfactants include 4-dodecylbenzene sulfonic acid (SDBS)[151] and sodium cholate[154], which have been reported to exfoliate graphite in water successfully.

Another example of liquid-phase exfoliation is the post-etching process of MXenes. Through a solvent-assisted delamination technique, multi-layered MXenes are separated into fewer layered MXene sheets. Such solvents include dimethyl sulfoxide (DMSO), N, N-dimethylformamide (DMF), N-methyl pyrrolidinone (NMP) and isopropyl amine[155]. However, many of these solvents contain nitrogen and sulfur heteroatoms, producing NO_x and SO_x compounds, respectively, when disposed of by incineration. In compliance with one of the principles of green chemistry involving the design of safer chemicals, developing solvents with high functionality and low environmental footprint is essential for green energy storage applications[156]. That is, chemicals should not only provide their functionality but should also be non-toxic.

Cyrene is a bio-based polar aprotic solvent obtained from biomass via two steps (**Fig. 2.14**): (i) heat-assisted conversion of cellulose to levoglucosenone in the presence of an acid catalyst, and (ii) catalytic reduction of levoglucosenone to dihydrolevoglucosenone (cyrene)[156].

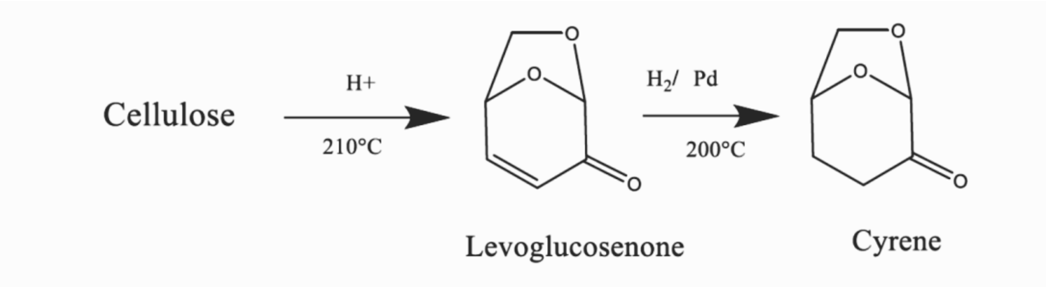

Fig. 2.14 Schematic of cyrene synthesis from biomass[157]

The interaction between solvent and solute is significant as solvents serve to dissolve chemicals. According to their dielectric constants, solvents are generally classified as polar or non-polar, and polar solvents are further classified into polar-protic and polar-aprotic solvents. Polar-protic solvents have dissociable hydrogen atoms, which distinguish them from its counterpart.

To determine a solvent's alternative, it is important to know the Hansen solubility parameters (HSP). HSP was developed by Charles M. Hansen as a way of predicting if a material will dissolve in another to form a solution. The Hansen space is a three-dimensional (x,y,z) representation that indicates the dispersion (δ_D), polarity (δ_p) and hydrogen bonding (δ_H) interactions of a solvent[156]. Neighbouring solvents in the Hansen space exhibit similar solubility properties, such as cyrene and NMP **(Table 1)**, and as such are predicted to behave similarly. Considering this and other exciting properties of cyrene, it would be beneficial to explore cyrene as a substitute to NMP, DMF, and other toxic solvents used as intercalating agents in the delamination of MXenes.

Table 1: Hansen space parameters showing similar solubility properties of cyrene and NMP[156]

Hansen space parameters	Cyrene	DMSO	NMP
δ_D	18.8	18.4	18.0
δ_p	10.6	16.4	12.3
δ_H	6.9	10.2	7.2

2.4. Hydrothermal Synthesis

Hydrothermal synthesis is a technique that has been exploited enormously over the years in producing various nanomaterials such as metal oxides, zeolites, ceramics, and nanocomposites[158]. Compared to traditional synthetic methods, hydrothermal synthesis methods do not involve very high-temperature operations, limiting chemical flexibility and control of the shape and size of particles[159]. Hydrothermal processes have produced 2D materials such as graphene, Molybdenum disulfide (MoS_2), MnO_2 and TiO_2. These hydrothermal methods of inorganic material synthesis include (i) batch and (ii) continuous hydrothermal flow synthesis.

2.4.1. Batch Hydrothermal Synthesis (BHS)

Several methods are used to produce inorganic nanomaterials, as highlighted in the table below.

Table 2: Comparison of synthetic methods to produce inorganic nanomaterials [160]

	Solid-state reactions	Coprecipitation	Sol-gel	Hydrothermal
Cost	Low – Moderate	Moderate	High	High
Composition control	Poor	Good	Excellent	Good- Excellent
Morphology control	Poor	Moderate	Moderate	Good
Purity (%)	<99.5	>99.5	>99.99	>99.5
Heat treatment	Yes	Yes	Yes	No
Milling step	Yes	Yes	Yes	No

Batch hydrothermal synthesis (BHS) is not a new development as it has been in operation for several years. A typical batch hydrothermal reactor schematic is shown below **(Fig. 2.15)**. It involves heating up precursors at elevated pressures in a sealed vessel at the required reaction temperature[161]. This reaction time determines the extent of nucleation and the sizes of particles formed at the end of the process. In a batch hydrothermal reactor, the precursors build up and reach a threshold level of supersaturation, then nucleation occurs. Dunne and co-workers [29] described that during the formation of the particles, there is a drop in the degree of supersaturation, and nucleation terminates when the rate of precursor input is less than the nucleation rate. Growth of particles is observed in a batch hydrothermal process due to the continuous growth of nucleated particles in the reactor, which attributes to the precursors' slow heating rate. The slowly-heated precursors are maintained above the critical nucleation threshold, enhancing continuous nucleation and simultaneous particle growth[159]. The distribution of particle sizes produced through this processing route is broad. In batch hydrothermal synthesis, a longer reaction time results in the growth of already formed nuclei. This is termed focusing of particle size, highlighting the faster growth of smaller particles than larger ones coupled with the formation of larger particles at the expense of smaller ones as suggested by Ostwald ripening and coalescence[159]. This results in the narrowing of the particle size distribution—however, the particle size increases.

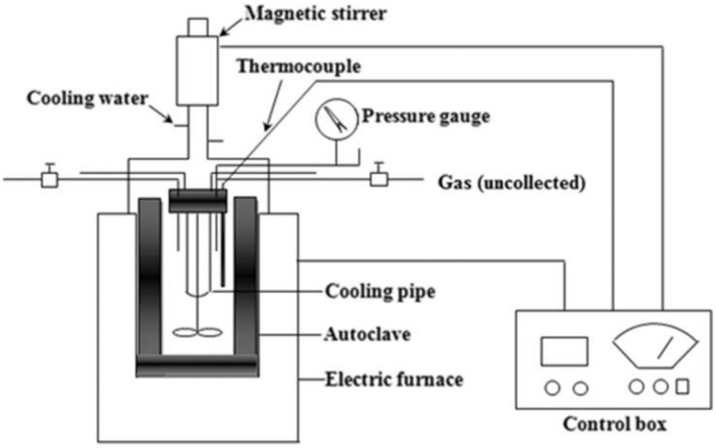

Fig. 2.15: Schematic illustration of a typical hydrothermal batch reactor[162]

2.4.2. Continuous Hydrothermal Synthesis (CHFS)

With a growing interest in green processes and nanotechnology, more sustainable synthetic routes are required in the production of nanomaterials for vast applications. Most of the reported literature on the synthesis of nanomaterials is based on batch or multi-step processes, which are often time-consuming and involve the use of toxic precursors.

In recent years, the use of a rapid, continuous, controllable, and environmentally friendly method of nanomaterial synthesis have been reported. This method is green as it involves the use of water (instead of organic solvents) and water-based precursors.

CHFS has been explored by several researchers in the engineering of nanomaterials for different applications. As mentioned, Kellici et al. (2014) synthesised reduced graphene oxide through CHFS by using aqueous KOH as an auxiliary precursor feed to replace hydrazine[163]. The CHFS- functionalised 2D reduced graphene oxide showed high antibacterial activities. Therein, CHFS showed a green, faster and economical synthetic means of graphene production with controllability over oxygen functionalities and particle size by controlling the reaction's temperature, pressure, and flow rates. Similarly, through CHFS, nitrogen-doped carbon quantum dots with an average particle size of 3.3 ± 0.7 nm were synthesised by Kellici et al. (2020) from aqueous citric acid and ammonia solutions. The N-doped carbon dots showed high selectivity and sensitivity for detecting highly toxic chromium (VI) ions[164]. Evans et al. synthesised vanadium dioxide-carbon nanotube (VO_2-CNT) nanocomposites via CHFS with dispersions of carbon nanotubes in an aqueous metal salt solution[165]. The synthesised VO_2-

CNT nanocomposites showed high sensitivity to water vapour and ammonia gas. Another example is the conversion of 2D graphene sheets into 0D graphene quantum dots through continuous hydrothermal flow synthesis (CHFS) and a particle sizing agent as described[166].

Kellici and co-workers also demonstrated a single rapid method of synthesising Ag-graphene nanocomposites with excellent antibacterial properties through combination with sulfonated calixarenes[167] . In their work, surface-functionalised reduced graphene oxide (rGO) through continuous hydrothermal flow method provides a support for Ag nanoparticles to prevent aggregation and also enhances bacteria adsorption due to negatively charged rGO surface. The Ag nanoparticles are stabilized by a class of macrocyclic compounds called calixarenes[167]. The nanocomposites showed high activity against E. coli (Gram-negative) and S. aureus (Gram-positive) bacteria and in selected cases the materials were reported to outperform traditional antibiotics.

Ceria-zirconia oxide/graphene nanocomposites were prepared via CHFS as a catalyst for the synthesis of dimethyl carbonate (DMC) from methanol and carbon dioxide[168]. In this work, graphene served as a substrate for growing ceria and zirconia oxide on its surface. The process modifies the surface of graphene and lowers its oxidation, resulting in the production of highly crystalline nanostructures. The synthesised ceria-zirconia oxide/graphene nanocomposites produced a 58.0 % methanol conversion to generate a 33.0 % yield of DMC[168]. This method produced 82.4 % conversion of propylene carbonate (PC) and a DMC yield of 78.2 %[168]. Tin doped zirconia (Zr–Sn–O) and tin doped zirconia/graphene nanocomposite (Zr–Sn/GO) have also been synthesised by CHFS as catalysts for the synthesis of DMC[169].

CHFS materials portfolio also includes the first development of directly printed graphene-based 3D structured heterogenous catalysts utilised for an industrially relevant reaction, the conversion of CO_2 into cyclic carbonates. Therein, 3D printed structures of CHFS synthesized graphene-based CeZrLa nanocatalyst showed improved activity with higher CO_2 conversion[170]. In addition, the nanocatalyst‘s ability to seperate from the product reduces materials and operating costs thereby contributing to the sustainability of the process[170]. This printing strategy shows great potential and fuels more pursuit towards green technology.

Batch hydrothermal synthesis (BHS) involves a slow reaction process as compared to Continuous Hydrothermal Flow Synthesis (CHFS), which produces materials through a faster reaction time by passing water-soluble precursors through a stream of supercritical water[166]. This supercritical state of water is achieved through pre-heating the water supply under elevated pressure. Water is a green solvent whose properties are exploited at supercritical conditions during the hydrothermal synthesis process of 2D materials. At these supercritical conditions of 374° C and 22.4 MPa, polar water behaves like a non-polar solvent due to changes in its density and polarity at high temperatures[159]. Exploiting these properties of supercritical water, such as its reduced dielectric constant and increased dissociation to H^+ and OH^- (**Eq. 4**). Hydrolysis, condensation and thermal decomposition of precursors are reactions occurring at the supercritical water conditions[171]. For example, in the generation of metal oxide nanoparticles, the metal salt hydrolyses, dehydrates and precipitates under set reaction conditions according to **Eq. 5 and Eq. 6** [159].

$$K_w = [H^+]\,[OH^-] = 1.0e^{-14}\,\text{mol}^2\,\text{dm}^{-6} \qquad \text{(Eq. 4)}$$

$$\text{Hydrolysis:} \quad ML_x + xH_2O \longrightarrow M(OH)_x + xHL \qquad \text{(Eq. 5)}$$

$$\text{Dehydration:} \quad M(OH)_x \longrightarrow MO_{x/2} + (x/2)\,H_2O \qquad \text{(Eq. 6)}$$

These processes occur due to the specific physical and chemical properties of water under these conditions. This behaviour of water and other precursors create an environment that facilitates nucleation and growth of particles. CHFS synthesis of nanoparticles occurs at supercritical conditions **(Fig. 2.16a)** where the reaction rate increases due to a decrease in the dielectric constant **(Fig. 2.16b)** of supercritical water[172].

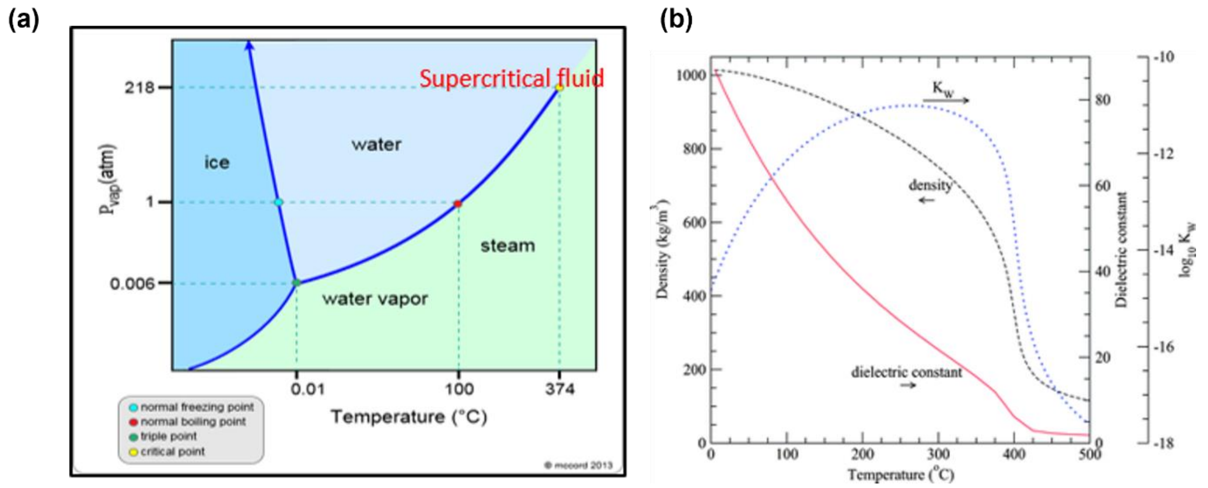

Fig. 2.16 (a) Phase diagram of water showing the supercritical region and **(b)** trend in the selected properties of supercritical water[159]

Fine particles, metal oxides and single crystals can be synthesised in CHFS by processing in near-critical or supercritical water conditions by controlling the density, viscosity and dielectric constant of the reaction medium through independent control over reaction parameters as temperature and pressure[163]. The reaction time is the time taken for nanoparticles to form, which determines the extent of nucleation and the sizes of particles formed at the end of the process. This hands-on approach of CHFS process offers the ease to tune the particle size, morphology, and crystal structure of as-synthesised materials. Controllable variables in a CHFS process includes reaction temperature and pressure, precursor type (acetate, nitrates) and flow rates, pH and concentration of inflow precursors, that simultaneously determine the properties of nanoparticles being formed (e.g. morphology, crystallinity, particle size and surface area)[173].

CHFS is an advantageous methodology over batch synthesis. It provides a rapid (fraction of second) reaction time, green (water-based), low cost, scalable, efficient, continuous, and reproducible synthesis procedure. In a simplified schematic shown below **(Fig. 2.17)**, the CHFS process involves delivering a flow of heated water above its boiling point under pressure to a mixed flow of water-soluble metal precursor(s), resulting in the nucleation and growth of nanoparticles at the reaction zone. Following this nanoparticle formation process, a heat exchange process takes place, where a flow of unheated water cools the nanoparticles. The end products of the process are collected as a dispersion of nanoparticles in water.

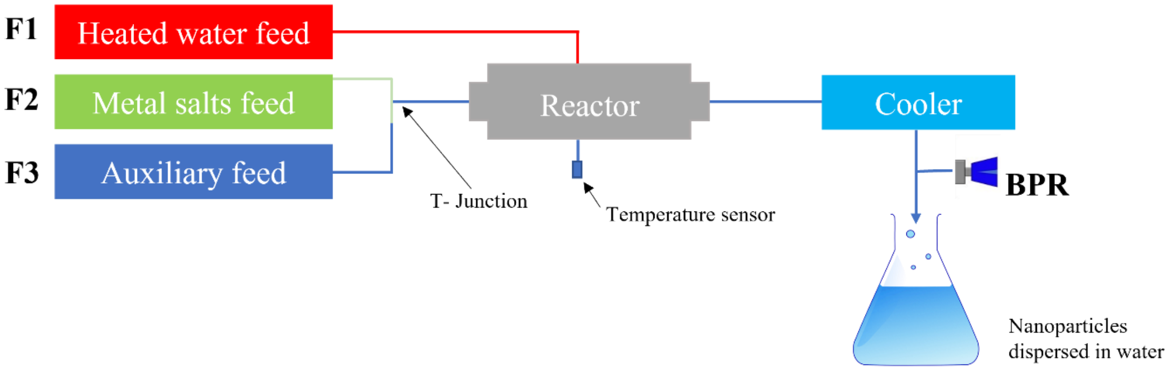

Fig. 2.17 A simplified schematic showing the components of the CHFS reactor used in the synthesis of nanomaterials.

In a continuous hydrothermal flow system, there is improved control of reaction temperature, pressure, residence time, precursor concentration and pH, as well as the heating rate of precursors[159,163,174,175]. In the CHFS reactor, there are three feeds delivering precursors into the reactor that meet at the mixing point (**Reactor in Fig. 2.17)**. The first is a water feed **F1** which delivers water, pre-heated under set reaction temperature and pressure into the mixing point. The second feed **F2** meets at a **T**- junction with the third feed precursor **(Fig. 2.17)** before delivering its precursors (e.g., aqueous metal salt, graphene oxide etc.) to the mixing point. The third feed, **F3** is called the auxiliary feed, which supplies other required precursors, e.g., surface stabilizers, alkaline solution etc.) to the mixing point. The resulting pressurized streams of precursors at the mixing point of the reactor are heated up rapidly with subsequent reactions occurring. The temperature of the mixing point, pressure and flow rates can be controlled, which highlights one of the advantages of the continuous hydrothermal flow process[163]. After the resulting reaction, the solution leaves the mixing point at the required residence time, which depends on the flow rate of the feeds and tubing's diameter of the mixing point. A stream of cold water cools the solution from the cooler at the base of the mixing point. The pressure of the reactor system is controlled by the back-pressure regulator (**BPR**), and the particles are collected from the outlet tubing of the BPR [176]. The particles are washed, separated by centrifugation, and freeze-dried to obtain solid nanocrystals which are collected for analysis.

2.4.3. Advantages of CHFS over BHS

Batch hydrothermal synthesis (BHS) involves a slow reaction process (several hours or days) as compared to Continuous Hydrothermal Flow Synthesis (CHFS), which produces materials through a faster reaction time by passing water-soluble precursors through a stream of supercritical water[166].

CHFS reaction times are in the order of seconds or fractions of a second. Indeed, the time from precursor to recovered nanomaterial (at the exit of the process) is typically in the order of a couple of minutes. This reaction time determines the extent of nucleation and the sizes of particles formed at the end of the process. Moreover, the reaction temperature when the two flows are mixed is typically in the range of 300–380 °C, compared to typically less than 250 °C for batch hydrothermal.

In addition, CHFS offers a chemical environment to functionalise materials through doping with atoms such as nitrogen, sulphur etc. [12]. Doping is a means of functionalising 2D materials for improved intrinsic properties. This doping process involves introducing a metal or non-metal into the material's crystal structure to enhance material performance for various applications. Doping via CHFS is carried out by delivering a supplementary feed of an aqueous dopant solution into the reactor to meet with supercritical water at set reaction conditions. Thus, CHFS synthesis/functionalisation occurs at supercritical conditions where the reaction rate increases due to a decrease in the dielectric constant of supercritical water[172]. Fine particles, metal oxides and single crystals can be synthesised in CHFS by processing in near-critical or supercritical water conditions by controlling the density, viscosity and dielectric constant of the reaction medium through independent control over reaction parameters as flow rates, temperature and pressure[163]. Through this means, there is easy to tune the particle size, morphology, and crystal structure of as-synthesised materials (unlike BHS, where larger particle sizes are obtained). Furthermore, the CHFS technology has further shown its green nature in the synthesis of nanomaterials by replacing organic solvents and compounds requiring energy-intense processing and generating higher emissions with water as a solvent resulting in lower emissions in raw materials and post-processing techniques[177]. Kellici et al. (2018) performed an LCA analysis in the CHFS of GQDs using SimaPro (8.3.0.0) software with Ecoinvent 3 Life Cycle Inventory database. Conclusions from this LCA analysis showed that CHFS generates less than 50 % environmental impact than the batch hydrothermal method in terms of human toxicity, ionising radiation and particulate matter[175].

Hence, CHFS provides numerous advantages over batch hydrothermal *via* providing a rapid (nanomaterials generated in a few seconds), green (utilises water rather than toxic precursors), low cost, the scalable, efficient, continuous, and reproducible procedure of synthesising high surface area and highly crystalline nanomaterials (**Fig. 2.18)**.

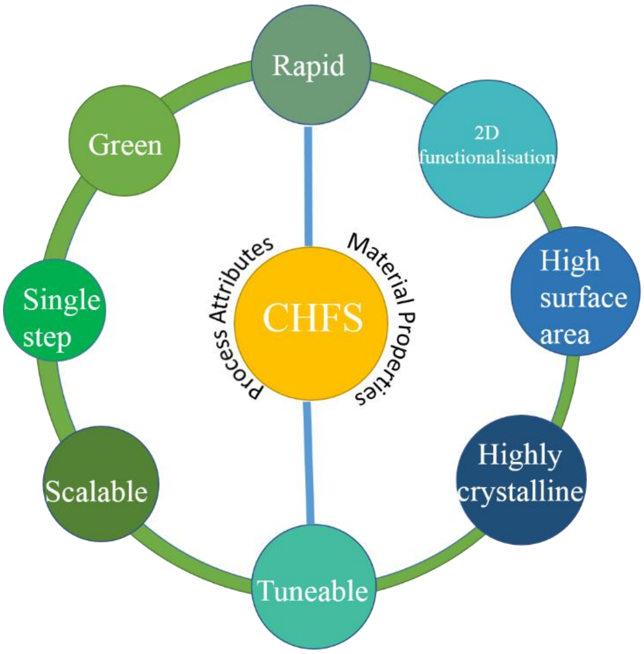

Fig. 2.18. Advantages of CHFS approach in material synthesis and the properties of the materials that it offers[12]

2.5. Energy Storage Devices

They play a role in storing electric energy when needed and releasing this electric energy when required. Energy storage devices (ESD) store energy in various forms such as chemical, electrochemical, kinetic, thermal, and electromagnetic[178].

2.5.1. Basic Parameters

2.5.1.1. Capacitance

Generally, capacitance is a parameter used to measure a material's ability to store electric charges. The theoretical capacity (C) is often calculated from **Eq. 7**, and it is dependent on the number of charges transferred as voltage (V) is applied across the plates. Current is a flow of electrons which depends on the amount of charge transferred per unit time (**Eq. 8**). By substituting **Eq. 8** into **Eq. 7** and introducing the mass of the electrode (m), the specific capacitance can be calculated from the amount of charge transferred per unit mass of the electrode (**Eq. 9**) in F g^{-1}. Similarly, the specific surface area of the electrode (s) can be introduced into **Eq. 7** to obtain the specific capacitance of the electrode in F cm^{-2}, as shown in **Eq. 9**.

$$Q = CV \qquad \text{(Eq. 7)}$$

$$Q = It \qquad \text{(Eq. 8)}$$

$$C_s = \frac{I * \Delta t}{\Delta V * m(\text{or } s)} \qquad \text{(Eq. 9)}$$

where, Q = charge (*C)*, C_s = specific capacitance (F g^{-1} or F cm^{-2}), I = charge-discharge current (A), m = mass of active electrode material (g), *s* = specific surface area of active electrode material (cm^2), ΔV = potential window (v) and Δt = discharge time (s).

The capacitance of a capacitor is a measure of how much electric charge can be stored across the plates of a capacitor (**Eq. 10**). This value increases as the area of the plates increases, and the distance ε value of capacitance due to thin EDL as compared to larger dielectric in capacitors[179].

$$C = \frac{\varepsilon A}{d} \qquad \text{(Eq. 10)}$$

Where C is the capacitance (F), ε is the dielectric constant (F m^{-1}) of the medium which is the product of the relative permittivity of vacuum (ε_o) and relative permittivity of the dielectric material (ε_r), A is the area of the plates (m^2) and d is the separation of the plates (m)[179,180].

2.5.1.2. Energy and Power Densities

Specific terminologies describe the process of storage and release of electric energy. These energy and power densities characterise the energy storage device[4]. Energy density measures the amount of electric energy per unit volume or unit weight an ESD can store[4].On the other hand, power density is the device's rate to deliver the energy stored per unit volume or weight[4]. The energy **(Eq. 11)** and power densities **(Eq. 12)** are calculated from the equations below:

$$E = 0.5\ C_s V^2 \qquad \text{(Eq. 11)}$$

$$P = E_s/\Delta t \qquad \text{(Eq. 12)}$$

2.5.1.3. Cycle Life

The life cycle of the ESD is the number of times (referred to as cycles) that the device can be charged and discharged before it reaches a stage where it no longer can store and deliver electric energy efficiently[4].

All these properties (life cycle, energy, and power densities) define the extent of performance of an energy storage device and the type of application requirement it can be implemented.

2.5.2. Electrochemical Storage

Electrochemical energy storage devices (EESD) are classified into batteries and electrochemical capacitors. The former stores energy as chemical reactants, while the latter stores energy as charge[178]. For this reason, batteries and electrochemical capacitors exhibit different lifecycle, energy, and power densities, making them applicable in various energy and power requirement operations.

In 1800, Alessandro Volta reported the first battery, which consisted of zinc and copper electrodes, a paper separator and a NaCl electrolyte[181]. Several significant developments followed this, including the lead-acid battery by Gaston Planté[182], nickel-cadmium battery[183], alkaline battery[184], cathodic $LiCoO_2$[185,186] and anodic graphite battery[187], and the more recent lithium-ion batteries[188], which has transformed electronic devices and electric vehicles. Supercapacitors, on the other hand, was the first patent in 1957 by H. Becker of General Electric and consisted of stainless steel electrodes in a sulfuric acid electrolyte[189]. This discovery paved the way for further innovation in supercapacitors and understanding their storage mechanism.

2.5.2.1. Batteries

Batteries play an important role in electrical energy storage. A battery is an electrochemical cell that converts chemical energy to electrical energy[178]. In a battery system, the chemical energy is the storage medium, converted to electrical energy as an electric current at a specific voltage during discharge.

The components of a battery include the positive electrode, the negative electrode, and the electrolyte. The cell reaction involves the active material in the electrodes and sometimes in the electrolyte (e.g., lead-acid batteries), thereby generating electrons in one electrode and absorbed by the other electrode. This flow of electrons is referred to as the current produced by the battery. **Eq(s). 13 & 14** are reactions occurring at the negative and positive electrodes during the battery discharge process. The negative electrode is oxidised and releases electrons, while the positive electrode is reduced and gains electrons. The overall cell reaction is represented by **Eq. 15**.

A battery is classified as primary (non-rechargeable) and secondary (rechargeable) batteries. These reactions (**Eq. 13 & Eq. 14**) occurring at the electrodes are typical in a non-rechargeable battery. However, when a rechargeable battery is charged, these processes are reversed, and an amount of energy must be supplied to the cell **(Eq. 15)**.

$$N_{(red)} \rightarrow N_{(ox)} + n \cdot e^{-} \qquad \text{Eq. (13)}$$

$$P_{(ox)} + n \cdot e^{-} \rightarrow P_{(red)} \qquad \text{Eq. (14)}$$

$$N_{(red)} + P_{(ox)} \rightarrow N_{(ox)} + P_{(red)} + \text{Energy} \qquad \text{Eq. (15)}$$

Sakai and Amano (2013) reported that the lead-acid battery provides excellent power output performance in low and high-temperature environments[190]. However, limitations such as low power production, slow charge-discharge rates and poor cyclic stability raise concerns about the need for new energy storage technologies such as metal-ion batteries and supercapacitors as the future of energy storage devices. Metal-ion batteries include Na^{+}, Li^{+}, Mg^{2+}, Ca^{2+}, Zn^{2+} and Al^{3+} ion batteries. These monovalent and multivalent metal cations shuffle back and forth between the positive and negative electrodes during charge and discharge processes. They are inserted and removed from the host electrode material.

Energy Storage Mechanisms in Batteries

In a lithium-ion battery for example, the positive and negative electrodes are soaked in an electrolyte containing dissociated salts and separated by a micro-porous membrane. The charge and discharge processes in a lithium-ion battery involve reversible intercalation/de-intercalation of lithium ions into/from the host electrode material. During the charging process,

Li^+ is extracted from the cathode (lithium metal oxides) and intercalated into the anode (carbonaceous materials)[191]. The process is reversed during discharge, as shown in **Fig. 2.19**.

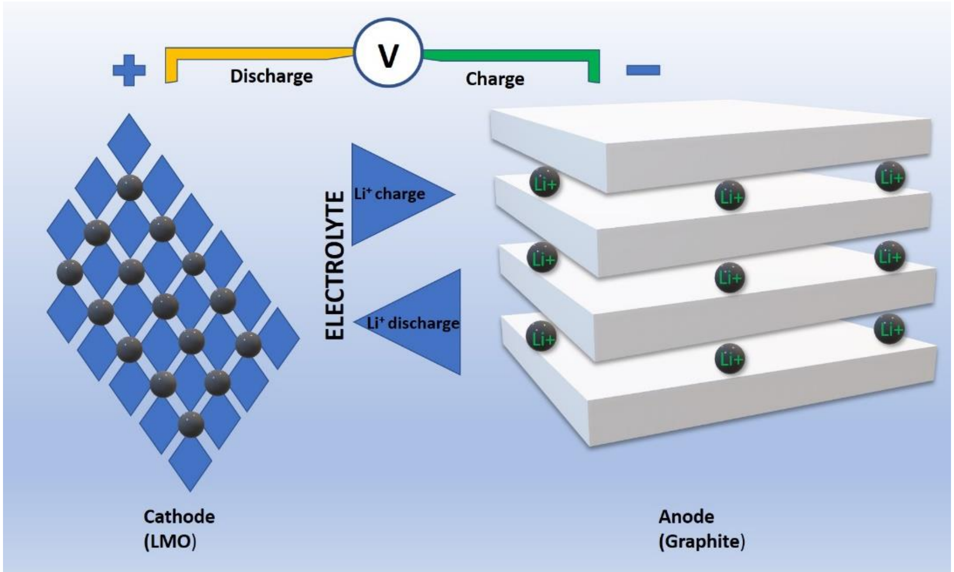

Fig. 2.19. Schematic of Lithium-ion battery charge storage mechanism showing intercalation/de-intercalation of Li^+ ions during charge and discharge processes[192]

2.5.2.2. Capacitors and Supercapacitors

A capacitor consists of two metallic electrodes separated by a dielectric medium **(Fig. 2.20)**. Potential energy is stored in a capacitor in the form of an electric field and released to the circuit as electrical energy. Dielectric used in capacitors include ceramics, polymer films or aluminium oxide. Compared to batteries, capacitors have lower energy densities but faster charge and discharge rates as they store energy directly onto the plates[179].

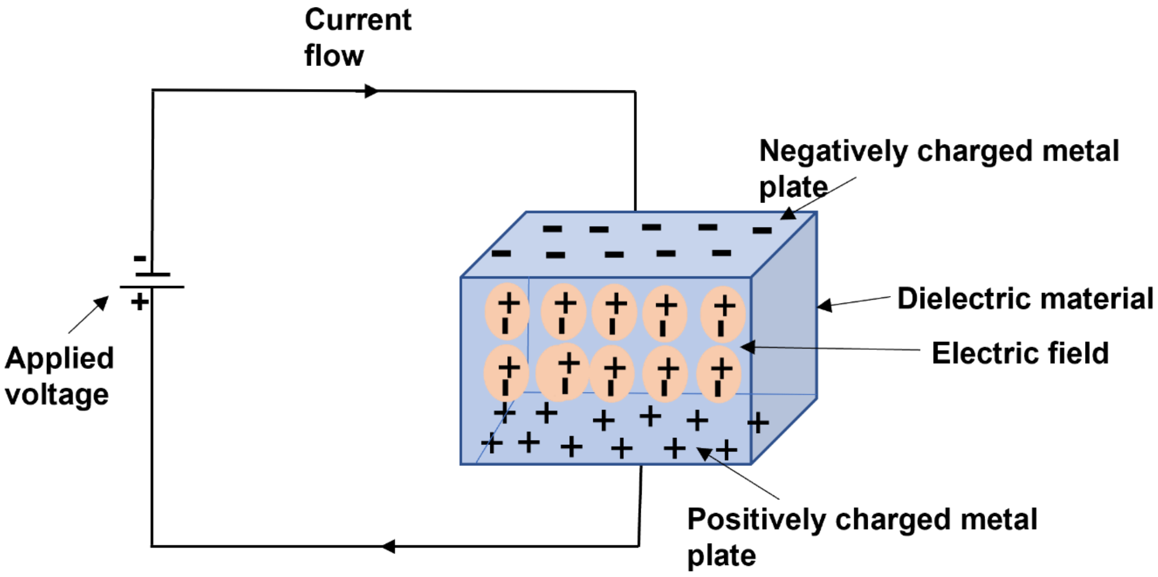

Fig. 2.20. Schematic showing storage mechanism in capacitors through charge storage across parallel plates.

Electrochemical capacitors or supercapacitors are distinct from capacitors in that the dielectric present in capacitors are replaced by an electric double layer (EDL) **(Fig. 2.21)**[180]. In supercapacitors, the electrode materials are soaked in an electrolyte and are separated by the EDL, which is much thinner than the dielectric found in capacitors. Supercapacitors are classified based on their charge storage mechanism; electric double-layer capacitors (EDLC) and pseudocapacitors. In EDLC, charge storage occurs at the electrode-electrolyte interface of high surface area carbon-based materials. During charging, a potential is applied. The electric field strength increases, generating an electric field within the cell, which causes hydrated counter ions to move from the aqueous electrolyte and adsorb between the electrode-electrolyte interface **(Fig. 2.21)**, forming an electric double layer. Electrode materials used in EDLC are commonly carbon-based materials such as activated carbon, carbon aerogels (CAGs), graphite, carbon nanotubes (CNTs), and nano-sized carbon materials like graphene [193]. The attraction of carbon-based materials in EDLC is due to their unique physical and chemical properties such as:

- High surface area (>2000 m^2/g)
- Porous nature
- Processibility into composites with other materials
- High conductivity

- High temperature and corrosion resistance

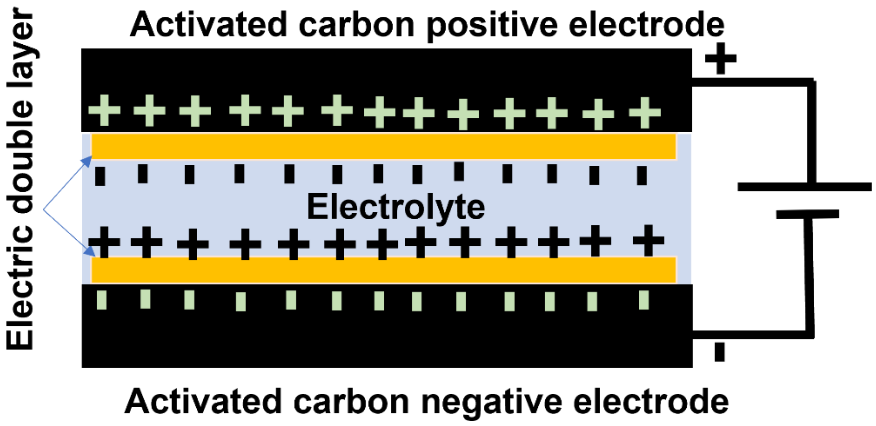

Fig. 2.21 Schematic of a supercapacitor showing the formation of an electric double layer[194]

In pseudo capacitors, charge storage involves ion intercalation fast and reversible surface or near-surface faradaic reactions of TMO electrodes[180]. Commonly used materials in a pseudo capacitor are TMOs such as RuO_2, TiO_2 and MnO_2. These metal oxides are attractive due to their high specific capacitance, high operational window, and several oxidation states. A combination of electric double-layer capacitive and pseudocapacitive electrode materials contributes to improved energy and power densities[195]. An example is the combination of pseudocapacitive metal oxides (e.g., TiO_2) with a capacitive carbon-based electrode (e.g., graphite, graphene, CNTs, MXenes).

2.5.3. Electrode Materials

Electrochemical capacitors may be distinguished in terms of the material composition of the electrodes, which simultaneously determines the device's storage mechanism and electrochemical performance. These electrode materials include carbon-based materials, transition metal oxides and conductive polymers. For good electrochemical performance, the specific surface area of the electrode material and the type of electrolyte used in the ECs are essential parameters to be examined. Also, controlling these material properties provides a promising route for developing ECs with improved electrochemical performance.

Different forms of carbon materials (activated carbon, CNTs, multiwalled carbon nano tubes, graphite and graphene) exist and have been explored as electrode materials due to their surface area, electronic conductivity, porous nature, chemical compatibility and other mechanical properties. The morphology and chemical compatibility of these carbon-based materials influence electrolyte permeation which promotes the formation of an electric double layer in EDLCs. Despite the exciting properties these carbon-based materials offer, some of these materials (e.g. AC) are challenged by the inability to control the pore size distribution efficiently, thereby affecting its energy storage capacity in EDLCs[196]. Graphene has been explored as a suitable alternative to other carbon-based electrode materials owing to its low cost, large-scale synthesis, and unique electronic properties. Several reports have been published on graphene-based electrodes with remarkable electrochemical performances[74,77,120].

Transition metal oxides and conducting polymers show pseudocapacitive energy storage mechanisms due to redox-active sites in their structures. Transition metals such as RuO_2, TiO_2 and MnO_2 have been reported in the literature to offer energy storage capacities. From all the transition metal oxides, RuO_2 show the best electrochemical performance, such as a very high specific capacitance (1000 F g^{-1}). However, RuO_2 is limited by its high cost of commercialisation. RuO_2 can either be replaced with other low-cost transition metal oxides such as TiO_2 and MnO_2 or combined as a nanocomposite with carbon-based materials or conducting polymers. Conducting polymers include polypyrrole (PPy), polyaniline (PANI) and the more popular poly (3,4-ethylene dioxythiophene) (PEDOT). These polymers undergo partial oxidation and reduction processes to generate charged species[197]. Several reports on conductive polymers as electrode materials have been reported with remarkable energy storage performances. Conductive polymers offer the advantage of good electrical conductivity, pseudocapacitance, flexibility, and low cost. However, they are limited by the instability of redox sites over multiple charges and discharge cycles, thereby reducing their storage capacity[198].

As such, the development of more environmentally sustainable electrode compositions must be progressive that utilise the excellent hydrophilic surface properties of MXenes in aqueous processing and electrode fabrication to eradicate the use of toxic organic solvents[199]. In addition, MXenes have high electronic conductivity (6500 S cm^{-1}), enabling them to serve as an active material and a current collector[12,48]. Examples of MXenes include $Ti_3C_2T_x$, Ti_2CT_x, Ti_3CNT_x, $Nb_4C_3T_x$, etc. [48,99]. Reversible redox reactions occurring at the titanium surface (Ti) in MXenes provide a pseudo-capacitance, thereby increasing the faradaic performance of a MXene electrode[103]. A tapped density of 4 g cm^{-3} exhibited by MXenes reduces the electrode's mass loading compared to 2D graphene (0.4 g cm^{-3}). A reported high volumetric capacitance of up to 900 F cm^{-3} in MXenes attracts increasing interest in energy storage applications[12,48].

Due to its natural abundance, low cost, high safety and non-toxic nature[84], TiO_2 serves as an attractive Li-ion anode material in energy storage[200,201] and various applications such as photocatalysis[86,202,203] and water treatment[202,203]. TiO_2 also exhibits a low volume expansion (<4 %) during the lithiation process, a prerequisite for long cycle life materials. However, challenges exist in performance, owing to the poor electrical conductivity and sluggish Li-ion diffusion within the material[204,205]. Utilising nano-TiO_2 is a potential route to overcome this due to improved surface area and reduced diffusion distance for Li-ion transport compared to bulk materials[204]. Furthermore, combining TiO_2 nanoparticles with highly conductive 2D materials such as MXenes can boost performance significantly while simultaneously eliminating the need for conventional fluorinated polymeric binders[204].

Advanced surface modifications of 2D materials via a unique route of synthesis offer an advantage of distinct morphologies, improved surface area and surface functionalities. In addition, these modifications alter the material structure by size tuning and engineering defects in the material, thereby causing a change in the electronic and optoelectronic properties[39]. As stand-alone materials do not have enough properties to render practical functions, it is advantageous to combine the properties and modified functionalities of 2D MXenes and TiO_2 nanoparticles as electrode materials to enhance electrochemical performance. However, the current approaches in the synthesis of materials face challenges, including toxic precursors, non-uniformity of particle size distribution, lengthy manufacturing time, and energy costs. As a result, there is a need to adopt synthetic strategies that overcome these challenges by providing a rapid, clean and scalable material synthesis process while delivering high-performance materials.

2.5.3.1. Electrolytes

Asides from the electrode material, electrolytes play a major role in the capacitive performance of energy storage devices. Some properties of a good electrolyte include high ionic conductivity, non-flammable, non-toxic and low cost. There are different types of electrolytes. They are classified into aqueous, organic, and ionic electrolytes. Aqueous electrolytes such as Na_2SO_4, KOH, NaOH, KNO_3, $LiNO_3$, etc. offer high ion concentration and low internal resistance but are limited to a low operating voltage of 1.0 V due to water splitting reaction that generates H_2 gas at a higher voltage[206]. Organic electrolytes (lithium hexafluorophosphate

($LiPF_6$) in ethylene carbonate (EC) or dimethyl carbonate (DMC), tetraethylammonium tetrafluoroborate (TEABF4) in acrylonitrile (ACN)) offer a higher operation voltage (up to 3.5 V). However, they are limited by cost, low conductivity and safety concerns[20]. Ionic electrolytes have a wide operation window (up to 6.0 V) good thermal and chemical stability that enhances the cycling performance of the ECs. Despite these properties, ionic electrolytes are limited by low conductivity[207].

2.5.4. Electrochemical Capacitors vs Batteries

The Ragone plot **(Fig. 2.22)** shows the characteristic performance of different energy storage devices by relating their energy and power densities. Electrochemical capacitors (EC) store potential energy in an electric field, while a battery stores its potential energy in a chemical form. These storage mechanisms provide ECs and batteries with low and high energy densities respectively. However, during discharge, the chemical process involved in converting chemical energy to electrical energy in batteries is slow. Hence, batteries show lower power densities when compared to the ECs where fast charge and discharge rates occur. ECs are employed in applications involving short-term energy storage, fast power delivery and regenerative braking (in electric vehicles). As the demand for portable electronics increases, researchers have focused on improving the charge-discharge times in batteries and increase the storage capacities in ECs.

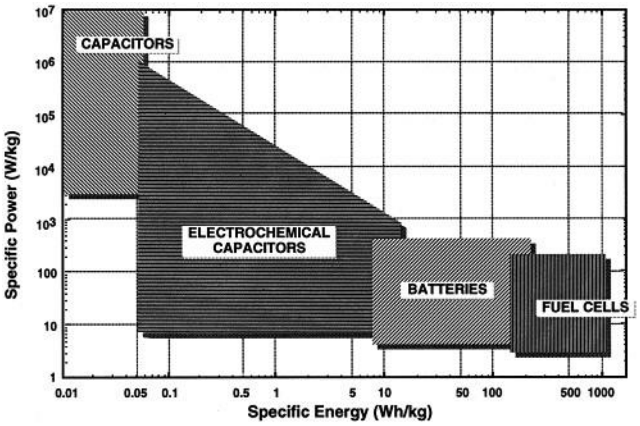

Fig. 2.22 Ragone plots for different energy storage devices showing relationship between energy and power densities[208]

ECs bridge the gap between conventional capacitors and batteries by offering improved energy and power densities compared to their counterparts. **Table 3** summarises the differences between ECs and batteries.

Table 3: Difference in properties between electrochemical capacitors and batteries

Electrochemical Capacitors	**Batteries**
Low energy density	High energy density
High power density	Low power density
Long cycle life	Limited cycle life
Fast charge-discharge cycles (in seconds)	Slower charge-discharge cycles (minutes to hours)
Wider temperature operating conditions (-40 °C to 65°C for both charge and discharge)	Narrow temperature operating conditions (0 to 45 °C for charge and -20 °C to 60 °C for discharge)
Low cell voltage (2.3 V – 2.8 V)	Higher cell voltage (3.6 V to 3.7 V)

Chapter 3: Methodology

3.1. Chemicals and Materials

Table 4: List of chemicals and materials used in this research study

Chemical	Molecular Formula	Specification	Supplier
Graphene oxide	GO	25 %	AbalonyX
MAX Phase	Ti_2AlC Ti_3AlC_2	Maxthal 211	Kanthal®
Manganese (ii) nitrate hexahydrate	$Mn(NO_3)_2.6H_2O$	98 %	Fischer Scientific
Potassium hydroxide	KOH	85 %	Sigma-Aldrich
Hydrogen peroxide	H_2O_2	30 %	Fischer Scientific
Titanium (iv) bis (ammonium lactato) dihydroxide	$[CH_3CH(O)CO_2NH_4]_2Ti(OH)_2$	50 wt. %	Sigma-Aldrich
De-ionised water	H_2O	15MΩ	
Cyrene			Sigma-Aldrich
Ethanol	C_2H_6O	99.5 %	Fischer Scientific
Isopropanol	C_3H_8O	99.5 %	Fischer Scientific
Carbon black	C		Kurraray
Activated carbon	AC	YP-50	Kurraray
Ammonia	NH_3	32%	Merck

3.2. Continuous Hydrothermal Reactor

In a continuous hydrothermal flow synthesis system, it offers control of reaction temperature, pressure, residence time, precursor concentration and pH, and the heating rate of precursor [163,171,174]. In the reactor used in this study (schematics of which is shown in **Fig. 3.1**), there are three feeds delivering precursors into the reactor that meet at the mixing point labelled as Reactor. The first is a water feed **F1** (Gilson 307 HPLC pump fitted with 25 mL pump head) delivering water, pre-heated through a heater under set reaction temperature and pressure into the mixing point (counter-current mixer). The second feed **F2** (Gilson 305 HPLC pump fitted with 10 mL pump head) meets at room temperature at a T-junction with the third feed precursor (**Fig. 3.1**) before delivering its precursors (e.g., aqueous metal salt, graphene oxide etc.) to the mixing point. The third auxiliary feed **F3** (Gilson 307 HPLC pump fitted with 10 mL pump head) feed supplies other required precursors (e.g., surface stabilizers, alkaline solution etc.) to the reactor. The formed products flow from the Reactor and her cooled down by passing through the cooler before they are collected.

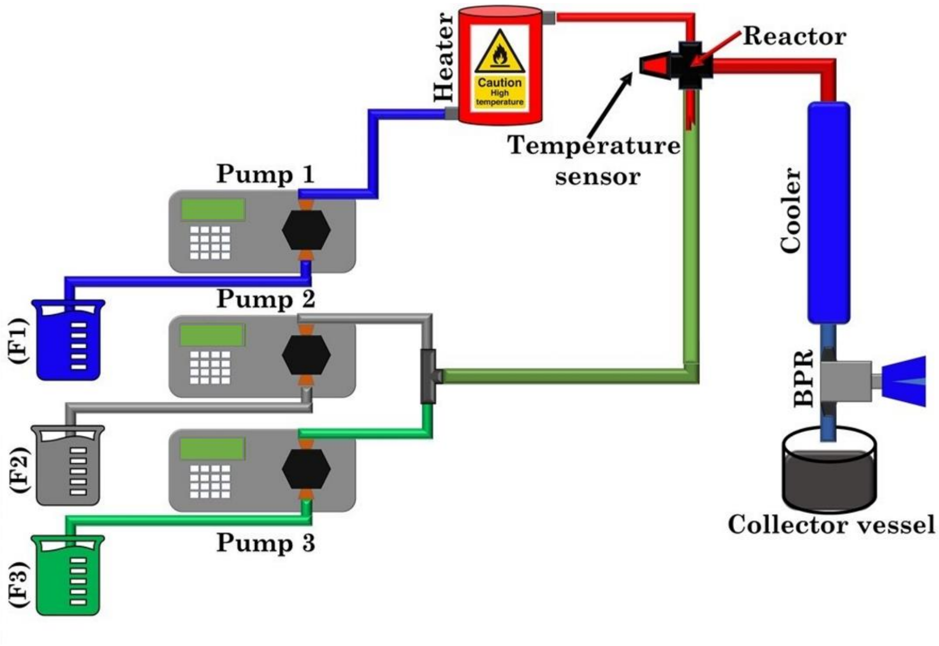

Fig. 3.1 Schematic showing the parts of a continuous flow process reactor for rapid synthesis of nanomaterials [192]

The list of water-soluble precursors and the experimental conditions used to synthesise these nanomaterials are summarised in **Table 5.** The resulting pressurized streams of precursors at the mixing point of the reactor are heated up rapidly, with subsequent reactions occurring. The temperature of the mixing point and pressure and flow rates can be tuned, highlighting one of the advantages of the continuous hydrothermal flow synthesis process[174]. After the resulting reaction, the mixture leaves the mixing point at the set residence time. The residence times depend on the flow rate of the feeds and the reactor volume. The reaction mixture is then passed through a vertical cooler at the base of the mixing point. The tubing and fittings are 1/8-inch 316SS Swagelok, except the counter-current reactor and the cooler constructed using 1/4-inch fittings. The pressure of the reactor system is controlled by the back-pressure regulator (**BPR**), and the particles pass through the cooler before they are collected from the outlet tubing of the

BPR. The particles are washed, separated by centrifugation, and freeze-dried to obtain solid nanocrystals, subjected to further analysis.

Table 5: List of as-synthesised materials through CHFS and their experimental parameters

Synthesised Materials	**Precursors**	**T (°C)**	**P (MPa)**	**Flow rates (mL min^{-1}) (P1, P2, P3)**
MnO_2	• 0.05 M Mn $(NO_3)_2.6H_2O_{(aq)}$ • 1 M $H_2O_{2(aq)}$	450	24.8	20, 5, 5
MnO_2/rGO	• 0.05 M Mn $(NO_3)_2.6H_2O_{(aq)}$ • 1 mg mL^{-1} $GO_{(aq)}$ • 1 M KOH(aq) • 1 M $H_2O_{2(aq)}$	450	24.8	20, 5, 5
N-TiO_2	• 0.2 M $[CH_3CH(O\text{-})CO_2NH_4]_2Ti\ (OH)_{2(aq)}$ • 0.5 M 32% $NH_{3(aq)}$ solution	450	24.8	20, 5, 10
N-TiO_2/rGO	• 0.2 M $[CH_3CH(O\text{-})CO_2NH_4]_2Ti\ (OH)_{2(aq)}$ • 2 mg mL^{-1} $GO_{(aq)}$ • 0.5 M $NH_{3(aq)}$	450	24.8	20, 5, 10
N-Ti_2C	• 2 mg mL^{-1} DMSO delaminated $Ti_2C_{(aq)}$ • 0.5M 32% $NH_{3(aq)}$	350-450	24.8	20, 5, 5
N-Ti_3C_2-TiO_2	• 2 mg mL^{-1} cyrene delaminated $Ti_2C_{(aq)}$ • 0.5 M 32% $NH_{3(aq)}$	350	24.8	20, 5, 5

3.3. CHFS of Materials

3.3.1. CHFS of TiO_2 and its Nanocomposites

TiO_2 and its nanocomposites were synthesised via the CHFS process using the respective precursors in **Table 5**. The precursors were prepared as aqueous solutions and delivered into the reactor at a flow rate of 20 mL min^{-1}, 10 mL min^{-1} and 10 mL min^{-1} in pumps **F1**, **F2** and

F3, respectively. The hands-on approach of CHFS enabled the control of experimental conditions, such that a temperature of 450 °C and a pressure of 24.8 MPa were used for the reaction. The as-synthesised materials were collected, centrifuged, washed with DI water and freeze-dried to obtain solids. The dried solids were examined via different analytical techniques.

3.3.2. Synthesis of N-doped TiO_2 Composites

Using ammonia as a nitrogen source, doping was employed as a functionalisation strategy to potentially enhance the electrochemical properties of TiO_2 composites. To do this, DI water was pumped via **F1** and an aqueous mixture of TiO_2 and graphene precursors in respective samples delivered via **F2**, and an aqueous solution of ammonia through the auxiliary feed **F3**, into the reactor with the flow rates in **F1, F2** and **F3** adjusted to 20 ml min^{-1}, 5 ml min^{-1} and 10 ml min^{-1} respectively. All synthesised materials were collected, washed with DI water, centrifuged, and freeze-dried to collect solid samples. The collected dried samples were characterised and analysed prior to running an electrochemical test.

3.3.3. CHFS of MnO_2 on the Surface of reduced Graphene Oxide nanosheets

Using a flow reactor design discussed earlier, CHFS experiments were conducted to synthesise MnO_2/Graphene nanoparticles. The system consists of pumps F1, F2 and F3 as labelled in **Fig. 3.1** above, delivering aqueous mixtures of de-ionised (DI) water in F1, pre-mixed manganese (IV) nitrate, H_2O_2 and GO solution in F2, and KOH in F3 at a flow rate of 20 mL min^{-1}, 5 mL min^{-1} and 5 mL min^{-1} in pumps F1, F2 and F3 respectively. In a typical experiment, Mn $(NO_3)_2$ (0.05 M) solution was prepared, and H_2O_2 (1 M) was added. GO (1 mg mL^{-1}) was added to the resulting mixture in different volume compositions to prepare Mn $(NO_3)_2$/GO in 1:1, 1:2 and 1:3 ratios. This aqueous mixture of Mn $(NO_3)_2$/GO/ H_2O_2 in P2 was pumped to meet a flow of KOH in F3 at a T-junction (**Fig. 3.1**). This mixture then meets superheated water (450 °C, 24.1 MPa) from F1 at the mixing point **R**, at which point formation of products occurs continuously. The experimental CHFS operating conditions (temperature, pressure and flow rate) were kept the same for all the reactions. The reaction temperature was monitored by a K-type thermocouple connected to the 1/4-inch Swagelok cross union stainless steel mixing point to read the temperature data on a Pico log software. The resulting suspension was cooled by passing through a vertical cooler, and the slurry was collected from the tubing outlet of the back-pressure regulator (BPR). The products were centrifuged and washed several times to a pH of 7. The residue was freeze-dried for 24 hrs, and solid particles collected for characterisation were labelled as **A**, **B, C** and **D** for MnO_2, MnO_2/Gr 1:1, MnO_2/Gr 1:2 and

MnO_2/Gr 1:3 nanocomposites, respectively. In sample A, no GO was added to the Mn $(NO_3)_2$ (0.05 M) and H_2O_2 (1 M) aqueous mixture.

3.3.4. Synthesis of MXene Precursors

MXene was prepared following processes described in the literature by Gogotsi and co-workers[99]. A schematic of the etching and delamination process is shown in **Fig. 3.2**. Ti_2AlC MAX (Ti_2AlC or Ti_3AlC_2) phase material (6 g) was added slowly into 20 % HF (200 mL) in a large flask. The resulting mixture was stirred mildly at room temperature for 24 h. Solid materials were obtained by vacuum filtration of the slurry and washed with DI water (2 L) until a pH of 6. Wet solids were collected and freeze-dried to get dried multi-layered MXene powder (*m*-MXene). *m*-MXene was further delaminated into fewer layers by bath sonication in (i) DMSO for 24 h, washed with isopropanol, and centrifuged at 3500 rpm for 20 minutes to obtain delaminated MXenes (*d*-MXenes), (ii) cyrene for 20 h, washed with isopropanol, and centrifuged at 1000 rpm for 2 mins to obtained cyrene-delaminated MXenes (MX-CYR) as detailed below. The delaminated MXenes were used as starting precursor in the CHFS treatment process.

3.3.5. N-doped TiO_2 -Ti_3C_2 and N-doped TiO_2-Ti_2C MXenes Nanocomposites via Delamination with Cyrene

To optimise the electrochemical performance of previously synthesised NMT nanocomposites, the synthetic procedure was modified to improve the material properties for an improved energy storage function. The starting material (*m*-MXene) was delaminated via ultrasonication with a biodegradable solvent, cyrene, as the delaminating agent. *m*-MXene was ultrasonicated in cyrene for 24 h, washed with isopropanol, and centrifuged to remove multi-layered and large flake materials. The supernatant: containing smaller flake materials was collected and freeze-dried to obtain dry solids for analysis.

Preliminary work 1:

To intercalate multilayered MXenes with cyrene, Ti_2C MXene powder was suspended in 20 ml, 40 ml and 60 ml of cyrene, and stirred continuously with a magnetic stirrer at room temperature. The resulting colloidal solution was placed in an ice-bath and, purged with a flow of argon at 0.3 bar and sonicated. Two sonication methods were used: bath (for 1h) and probe sonication (for 30 mins) techniques. Both bath-sonicated $MXCYR_{bath}$ and probe-sonicated $MXCYR_{probe}$ MXenes were centrifuged at 3500 rpm for 2 minutes to separate the intercalated MXene powders from the cyrene solvent. After decantation, the residue was washed with isopropanol and further centrifuged at 9000 rpm to obtain a single flake and few-layered MXenes from supernatant and residue, respectively. Collected materials (MXCYR) were freeze-dried and stored for characterisation and further analysis.

Preliminary work 2:

From the SEM analysis in preliminary work 1, the synthetic strategy was optimised. This optimisation includes:

- Selection of bath sonication technique (as it generated less defects),
- Increase volume of cyrene solvent to 40 ml and 60 ml.
- Increased sonication time to 24 h.

These optimisation strategies were selected to improve the delamination process and investigate the oxidising effect of cyrene in MXene. Centrifugation and washing conditions remained the same, and collected materials were freeze-dried and stored for characterisation and analysis. Different techniques were used to characterise the as-synthesised MXene samples to analyse its crystallinity, morphology, chemical composition, and conductivity.

The obtained cyrene-delaminated MXenes **(CYR-MX)** were redispersed in DI water at a concentration of 2 mg mL^{-1} and delivered into the reactor as an aqueous precursor at a flow rate of 5 mg mL^{-1} for the synthesis of modified NMT nanocomposites. Other precursors introduced into the CHFS reactor includes DI water and 0.5M aqueous ammonia solution at a flow rate of 20 mL min^{-1} and 5 mL min$^{-1,}$ respectively. The modified NMT nanocomposites were fabricated into electrodes and tested for electrochemical performance via CV measurements.

3.3.6. CHFS of N-doped MXene/TiO$_2$ (NMT) Nanocomposites

The system consists of three pumps as labelled in **Fig. 3.1**, delivering aqueous mixtures of de-ionised (DI) water in **F1**, 2 mg mL^{-1} delaminated MXene solution in **F2**, and 0.5 M ammonia in **F3** at a flow rate of 20 mL min^{-1}, 5 mL min^{-1} and 5 mL min^{-1}, respectively. Therein, ammonia served as the doping source in functionalising 2D MXenes. The aqueous mixture of MXene in **F2** was pumped to meet a flow of aqueous ammonia in F3 at a T-junction. This mixture then meets superheated water (T = 350 °C and 450 °C, P = 22.4 MPa) from **F1** at the reactor, where product formation occurs continuously. Experimental CHFS operating conditions (pressure and flow rate) remained the same for the different temperature reactions. The reaction temperature was monitored by a K-type thermocouple connected to the 1/4-inch Swagelok cross union stainless steel mixing point to read the temperature data on a Pico log software. The resulting suspension was cooled by passing through a vertical cooler, and the slurry was collected from the tubing outlet of the back-pressure regulator **(BPR)**. The assembled products were centrifuged and washed several times to a pH of 6. The residue was freeze-dried for 24 hrs, and solid particles were collected for characterisation. The as-synthesised materials at two different temperatures of 350 °C and 450 °C were labelled as NMT350 and NMT450, respectively.

3.3.7. CHFS Synthesis of N-doped Cyrene delaminated Ti_2C and Ti_3C_2 – TiO_2 nanocomposites (NMT-CYR)

With the same experimental procedure described in **section 3.3.4**, delaminated MXene is replaced with **CYR-MX** as the MXene precursor supplied into the CHFS reactor.

3.4. Equipment and Techniques

3.4.1. Centrifugation and Freeze-Drying

Centrifugation was performed using a Heraus Megafuge 8 centrifuge by Thermo Scientific at selected revolutions per minute to separate solids from the supernatant. After centrifugation, collected slurries were frozen with liquid nitrogen and freeze-dried using a Heto Powder Dry PL3000 for 24 h. After freeze-drying, the obtained dried solids were ground using an Agate mortar and pestle set and stored in vials in the appropriate storage conditions.

3.4.2. Scanning Electron Microscopy

Scanning Electron Microscopy imaging (SEM) was employed in this research as it offers higher magnification and nanometre-scale resolution than a microscope, enabling three-dimensional imaging of the sample surface. The basic principle of SEM operation involves ejecting a highly accelerated beam of electrons towards the sample surface. After interaction of these high energy primary electrons with the sample, back-scattered electrons, secondary electrons, and X-ray signals are generated and received by the detectors, which gives information about the structure, composition and topography of the sample. Using a Zeiss Upra 55VP field emission gun scanning electron microscope, all images were acquired.

For good SEM imaging, the samples are required to be electrically conductive to have a conductive path for the ejected electrons. As a result, non-metallic powdered samples for SEM imaging were prepared by sputter coating with gold to ensure conduction of the layer. Samples were imaged at 5kV with secondary electron imaging (SEI) to obtain images.

3.4.3. Energy Dispersive X-Ray Spectroscopy

Energy-Dispersive X-Ray Spectroscopy (EDS) analysis of samples was obtained by using X-Max50 detector and Aztec Live Energy acquisition and analysis software. It combines a live electron image with live X-Ray chemical imaging to give chemical information about samples.

3.4.4. Transmission Electron Microscopy

For more micro-structured detailed imaging, Transmission Electron Microscopy (TEM) imaging of all samples was acquired for particle size determination and morphology analysis using a JEOL JEM-1400 microscope with an accelerating voltage of 80 kV. Samples were deposited on a 300-mesh holey carbon film copper grids by dispersing a small amount in ethanol and adding a few drops of the suspension over the TEM grids. TEM grids were dried in air and used for imaging. Particle size measurements were performed with ImageJ particle size analysis software.

3.4.5. X-Ray Diffraction

The crystallinity and atomic structure of the nanomaterials were determined through X-ray diffraction analysis. Diffraction patterns were obtained using a Bruker D8 ADVANCE X-ray diffractometer equipped with a ceramic copper target X-ray tube. In XRD, the crystalline nanomaterial is bombarded with a beam of X-rays and diffracted at different angles along its crystal planes (h,k,l) at different angles defined by Braggs' law ($n\lambda = 2d \sin \theta$). The intensities of the diffracted X-rays are measured and plotted against Bragg's angle 2θ to generate a diffraction pattern for the crystalline nanomaterial. These diffraction patterns give crystallographic information about the nanomaterials and can also be used qualitatively and quantitatively to identify and measure the average particle sizes (using Scherer's equation).

3.4.6. X-Ray Photoelectron Spectroscopy

X-ray photoelectron spectroscopy (XPS) measurements were performed using a Thermo Fisher Scientific K-alpha$^+$ spectrometer utilising a micro-focused monochromatic Al X-ray source operating at 72 W (6mA x 12 kV) and with the 400-micron spot mode, which averages over an elliptical area of approximately 400 x 600 microns. Data was recorded at pass energies of 150 eV for survey scans and 40 eV for a high-resolution scan with 1 eV and 0.1 eV step sizes. The charge neutralisation of the sample was achieved using a combination of both low-energy electrons and argon ions. Data analysis was performed using CasaXPS (v2.3.24) using Scofield sensitivity factors and an electron escape depth dependence of -0.6 after subtraction of a Shirley-type background.

3.4.7. Raman Spectroscopy

Raman spectroscopy measurements were performed on a Jobin Yvon Labram HR laser Raman microprobe equipped with a 473 nm laser to investigate samples' mineralogy and organic nature.

3.4.8. Fourier-Transform Infrared Microscopy

The molecular fingerprint of the nanomaterials was obtained as a Fourier –Transform Infrared (FTIR) spectra through a IR Affinity-1S Fourier transform infrared spectrophotometer instrument. The sample is irradiated with Infrared (IR) radiation, and subsequently measuring its absorbance and transmittance of the IR radiation. The resulting spectrum depicts the molecular fingerprint of the nanomaterial, and spectrum data is analysed using Origin Pro.

3.4.9. Thermogravimetric Analysis

The thermal stability and fraction of volatile components in the nanocomposites was determined by a Mettler Toledo TGA/DSC 3^+ STAR System instrument under air with a heating rate of 10 °C min^{-1}.

3.5. Electrochemical Measurements and Techniques

3.5.1. Electrode Fabrication

The as-synthesised materials in this project were fabricated into electrodes using the following formulations:

Table 6: Percentage composition of electrode materials

	Active Material	Carbon black	Binder	Solvent	Sample label number
wt % Composition	75 %	20 %	5 % PTFE	Ethanol	**3-6**
w/v ratio	1			10 De-ionised water	**1, 2 & 7**

Sample ID 1= NMT350, 2= NMT450, 3= MnO_2, 4= All MnO2-rGO, 5= TiO_2, 6= TiO_2-rGO, 7= All NMT-CYR

The as-prepared nanomaterials (samples 1 & 2) were prepared into slurries with the formulations in **Table 6** using an Agate mortar and pestle. The slurry was deposited using a doctor blade on Al or/and Cu foil as current collectors and dried first in the air for 24 h, and in a vacuum oven at 110 °C for an hour to ensure all solvents were removed.

Other as-synthesised samples (NMT-CYR, MnO_2 and TiO_2 nanocomposites) were mixed with carbon black and polytetrafluoroethylene (PTFE) in a ratio of 75:20:5, dispersed in ethanol, and further combined to form a homogenous chewing-gum like texture. With a circular punch, the paste was cut into electrodes with a mass loading of 70.8 mg cm^{-2}. All electrodes were dried under vacuum at 80 °C for 24 h. In an argon-filled glove box, all electrodes were assembled into a coin cell with a Celgard separator and 1M $LiPF_6$ in EC/DMC (1:1 v/v) electrolytes. The coin cell was sealed with a crimping machine and tested for electrochemical analysis.

3.5.2. NMT Electrodes Fabrication

The MXene/TiO_2 nanocomposite was mixed with de-ionised water in a ratio of 1:10 w/v and stirred for 12 hrs to form a homogenous and viscous slurry. The slurry was coated onto a Cu foil substrate (of thickness 9 um) using a laboratory-scale doctor blade machine, without any binders or conductive additives. The MXene tape was air-dried for 24 h, and further vacuum-dried at 110 °C for 60 minutes to ensure all water was removed. Samples were cut out with a circular punch to an area of 0.2 cm^2 and an average mass loading of 2.6 mg cm^{-2}.

3.5.4. Cyclic Voltammetry

Cyclic Voltammetry (CV) was used in this study to investigate the behaviour of electrochemically active species in the as-synthesised electrode materials. CV provides an insight into the reactions occurring in the bulk and near-surface of the electrode material, providing an understanding of the kinetics and thermodynamics of the redox and electron-transfer reactions involved.

During a typical CV operation, a potential is applied to an electrode containing the active species immersed in an electrolyte solution and the generated current is measured. The applied potential is swept in opposite directions within a selected voltage range to produce current. The measured current is due to the flow of electrons in the electrochemical cell caused by diffusion of electroactive species.

In this research, a two-electrode configuration was employed where active materials served as the working electrode, and Li disc served as the counter and reference electrode.

For a capacitive material, the value of specific capacitance was calculated from CV using **Eq. 16** [209].

$$C_s = \frac{\int I dV}{\Delta V * m * v} \qquad \text{Eq. (16)}$$

Where IdV is the area under the CV curve, ΔV is the potential window (V), m is the mass (g), and v is the scan rate (mV s^{-1}).

3.5.6. Galvanostatic Charge-Discharge (GCD)

GCD was used to investigate the cycling performance of the electrode material. In a typical charge and discharge setup, the cell is charged and discharged between two voltage points a constant applied current. The charge and discharge cycles were carried out between 0 to 3 V. The capacitance values from GCD curves were calculated using **Eq. 17** [209].

$$C_s = \frac{I \int (1/V(t) dt}{m} \qquad \text{Eq. (17)}$$

Where C_s is the specific capacitance in F/g, I/m is the current density (A g^{-1}), V(t) is the potential as a function of t, and t is the discharge time.

Chapter 4: Continuous Hydrothermal Flow Synthesis and Application of TiO_2-Graphene Nanocomposites in LIBs

4.1. Introduction

Energy storage systems with performances superior to the lead-acid batteries includes supercapacitors (SCs) and lithium-ion batteries (LIBs). Supercapacitors provide high power, fast charge/discharge cycles, and long cycle life, while LIBs offer a higher energy density than SCs but suffer from low power density. However, the performance of these energy storage systems depends greatly on their electrode material composition. Materials such as transition metal oxides (TMOs)[204], conductive polymers[210], carbonaceous materials like graphite[211], carbon nanotubes (CNTs)[212], MXene[192], graphene[80] and CQDs[213] have been explored extensively as electrode materials owing to their compatibility with electrolytes, chemical stability and high electronic conductivities.

In the development of green electrode materials for electrochemical energy storage technology, TiO_2 has received vast attention as a negative electrode material owing to its abundance, low cost, and environmental friendliness. In addition, TiO_2 exhibit good cyclic stability, high lithium insertion/extraction voltage (1.5 V vs. Li^+/Li) and low volume expansion during Li^+ intercalation[84,204,205]. However, TiO_2 as a stand-alone electrode material is limited in electrochemical performance by its low electronic conductivity (approx. 10^{-12} S cm^{-1})[214,215]. This limitation can be observed in the abrupt decrease in specific capacitance as scan rate increases.

Carbonaceous electrode materials include activated carbon, carbon nanotubes, carbon quantum dots, graphite etc[7]. These carbon materials have been extensively explored as electrode materials for energy storage applications; where they offer high specific area, excellent stability, and high electronic conductivity, but suffer from low specific capacitance[216]. For example, in the commercialised LIBs; graphite anodes have been explored economically due to its abundance and low cost[211]. Carbon quantum dots (CQDs) are zero-dimensional (0D) carbon nanomaterials that offer fast electron transfer and high surface area when used as an electrode material. CQDs are a great choice in nano-engineering of materials for electrochemical energy storage owing to their non-toxic nature and unique properties due to size. CQDs are produced through pyrolysis of organic compounds, hydrothermal, chemical, electrochemical and microwave-assisted synthetic methods[217].

Graphene, another carbon-based material is an extensively researched 2D material in electrochemical energy storage technology due to its superior properties, compared to its other carbonaceous counterparts. These properties include higher mechanical strength, large surface area and an improved electrical conductivity due to its zero-band gap[31,55,149,218]. Since its discovery in 2004 by Geim and co-workers[26], graphene has been developed by numerous researchers as an electrode material for LIBs due to its high electrical conductivity and excellent mechanical properties[219–221]. However, restacking of graphene sheets due to the strong π-π interactions and Van der Waals forces that reduces its surface area has been a challenge in its exploration as an electrode material[54]. Incorporating other electrochemically active materials between graphene sheets can help avoid a collapse of graphene sheets and increase its surface area.

A prospective solution to these challenges would be the coupling of TiO_2 with carbonaceous materials such as graphene to form composites. This strategy combines the pros of all composite materials as an advantageous strategy in overcoming their individual cons as an active electrode material. For example, combining TiO_2 and graphene as nanocomposites to effectively keep graphene sheets separated; providing the composites with more active sites, large specific surface area and fast electron transport kinetics[222]. To do this, CHFS was employed as a synthetic methodology in making TiO_2-graphene composites.

Using the described CHFS approach in **chapter 3**, a flow of supercritical water in **F1**, TiO_2 and graphene precursors in **F2**, and NH_3 as an auxiliary feed in **F3** at 20 mL min^{-1}, 5 mL min^{-1} and 10 mL min^{-1} respectively were introduced into the continuous hydrothermal flow reactor set at 450 °C and 3600 psi (**Fig. 3.1**). The experimental conditions for all the synthesised materials are shown in chapter 3 **(Table 5)**.

4.2. Results and Discussion

The morphologies and microstructure of the as-synthesised TiO_2 composites were studied through transmission electron microscopy (TEM) and scanning electron microscopy (SEM). Particle size measurements were obtained from high-resolution TEM (HRTEM) images of 50 TiO_2 nanoparticles using Image J software. Therein, a network of TiO_2 nanoparticles **(Fig. 4.1a)** with an average size of 6.17 ± 1.24 nm can be seen to be interconnected and well dispersed on the surface of graphene sheets. Also observed in the HRTEM images are dark patches which are as a result of overlapping TiO_2 nanoparticles. The HRTEM **(Fig. 4.1b&d)** and selected area diffraction (SAED) pattern **(Fig. 4.1c)** shows the crystalline nature of the nanocomposite with crystalline lattice fringes corresponding to the lattice planes of anatase TiO_2 **(Fig. 4.1b)**. A lattice fringe spacing of 0.354 nm was measured from the nanospheres and attributed to the (101) planes of anatase TiO_2 **(Fig. 4.1d)**[113,192,223,224]. An inset in **Fig. 4.1c** shows the selected area diffraction pattern of (101) planes of anatase TiO_2 nanoparticles with polycystalline reflections[225].

.

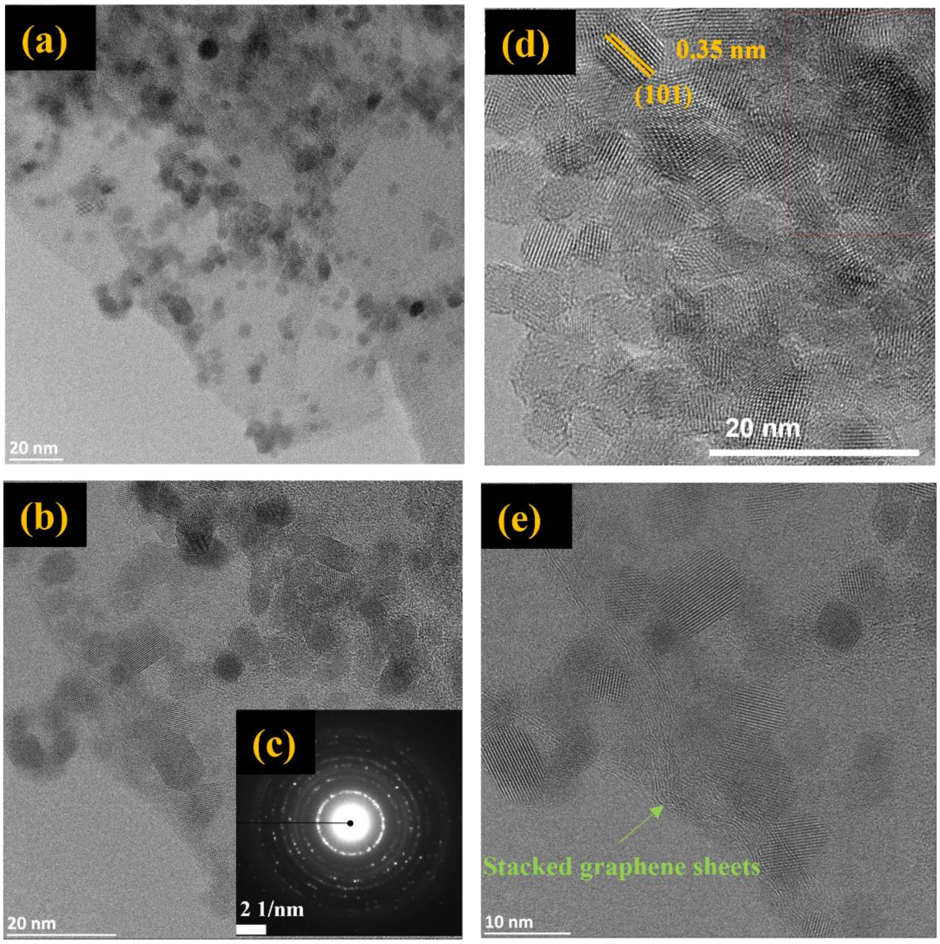

Fig.4.1(a) TEM image of TiO_2 nanoparticles dispersed on graphene sheet **(b)** TEM image & **(c)** SAED pattern of TiO_2 nanoparticles **(d)** HRTEM image showing lattice planes of TiO_2 **(e)** HRTEM image of TiO_2-rGO nanocomposites showing graphene sheets (TEM images taken by Dr. Tobias Heil)

The Raman spectra of TiO_2 and TiO_2-rGO nanocomposites are shown in **Fig. 4.2 (a)**. The observed Raman peak at 145 cm^{-1} is assigned to anatase TiO_2 that is present in the sample. TiO2-rGO also show characteristic D and G Raman bands at 1327 and 1597 cm^{-1}, and are attributed to the presence of defects and sp^2 graphitic structure respectively.

To analyse the crystal structure of the TiO_2 and TiO_2-rGO nanocomposites, X-ray diffraction (XRD) patterns were obtained **(Fig. 4.2b)**. Both samples show diffraction peaks at 2θ = 25.4°, 38.1°, 48.2°, 54.5°, and 62.9°, which are indexed as the (101), (004), (200), (105) and (204) planes of anatase TiO_2 respectively [192,214,226], which confirms the presence of anatase phase of TiO_2 in the sample. It is important to note the masking effect of a characteristic rGO diffraction peak expected at 26.0° by the (101) plane of TiO_2 at 25.4°[227,228].

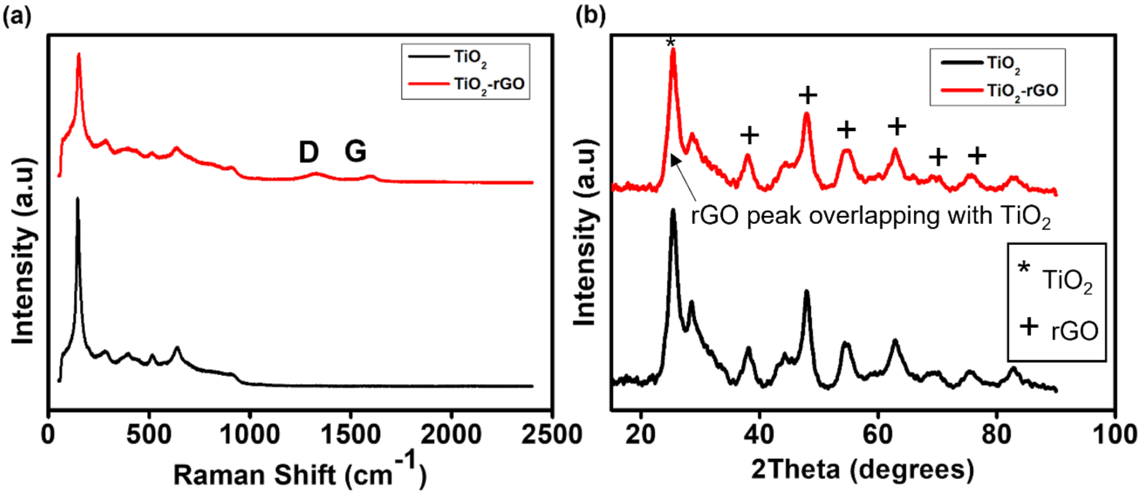

Fig. 4.2 (a) Raman spectra showing defects (D band), sp^2 graphitic structure (G band) and **(b)** XRD patterns showing crystallinity of TiO_2 and TiO_2-rGO nanocomposites

The elemental composition and chemical state of as-synthesised TiO_2-rGO were determined by Xray Photoelectron Spectroscopy (XPS). **Fig. 4.3** show the survey spectrum and characteristic elemental spectra of constituent atoms that indicates the presence of Titanium, Oxygen, Carbon and Nitrogen in the CHFS prepared nanocomposite. Two peaks of Ti $2p_{1/2}$ and $Ti2p_{3/2}$ were observed at 465.2 eV and 459.4 eV respectively, with a separation of 5.8 eV. The presence of $Ti2p_{3/2}$ component and the split separation value confirms the presence of titanium oxide with a +4 oxidation state (TiO_2), while an absence of peak at 457.6 eV was indicative of no presence of Ti^{3+} in the nanocomposite[95]. The O1s spectrum showed two peaks centred at 530.6 eV and 531.9 eV which corresponds to crystal lattice oxygen species O^{2-} and oxygen vacancies respectively. The C1s peaks are observed at 284.5 eV, 285.2 eV, 286.9 eV and 289.4 eV which are attributed to C=C, C−C, C−O and C=O groups respectively[229]. Also present in the nanocomposites are N1s peaks from the doping process through CHFS where peaks at 400.6 eV and 398.3 eV corresponding to protonated pyridinic nitrogen and pyrollic/amino N-H groups respectively [192,230].

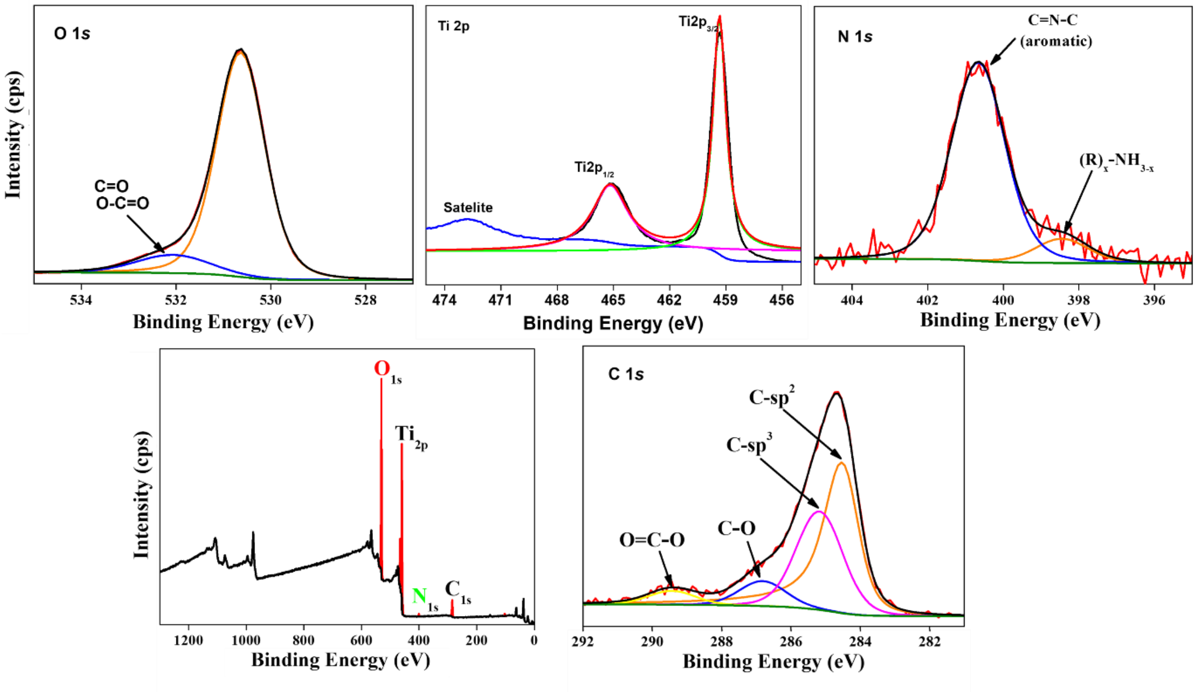

Fig. 4.3 XPS showing (O1s), (Ti2p), (N1s), (C1s) and Survey spectrum of TiO_2-rGO nanocomposite (XPS spectra collected by David Morgan, fittings done by Uthman Alli)

To perform a quantitative analysis of the TiO_2-rGO composite, thermogravimetric analysis (TGA) was conducted. The composite was heated under air flow with the heating rate of 10 °C min^{-1} to a temperature of 1100 °C. The TGA **(Fig. 4.4a)** and derivative gravimetric analysis (DGA) **(Fig. 4.4b)** curves show an initial mass loss of approximately 6.0 wt.% between 25 °C and 127 °C owing to evaporation and dehydration of adsorbed water molecules from the material, and a further mass loss of 4.8 wt.% between 127 °C and 354°C which is attributed to loss of oxygen functionalities in rGO. A significant mass loss of 8.8 wt.% was also observed between 350 °C and 550 °C due to the pyrolysis of carbon structure. The weight loss is stabilised at 80.5 wt.% at temperatures between 605 °C and 1100 °C, indicating that the composite consists of 19.5 wt.% rGO. This weight composition of TiO_2 to rGO corresponds to the concentration and volume of precursors put into the CHFS reactor with a 80% conversion yield of 0.2 M Ti^{4+} precursor to TiO_2, and 70% conversion yield of 2 mg ml^{-1} GO to rGO. The DGA showed the exact temperature in the sample where pyrolysis of carbonic structures took place (488°C).

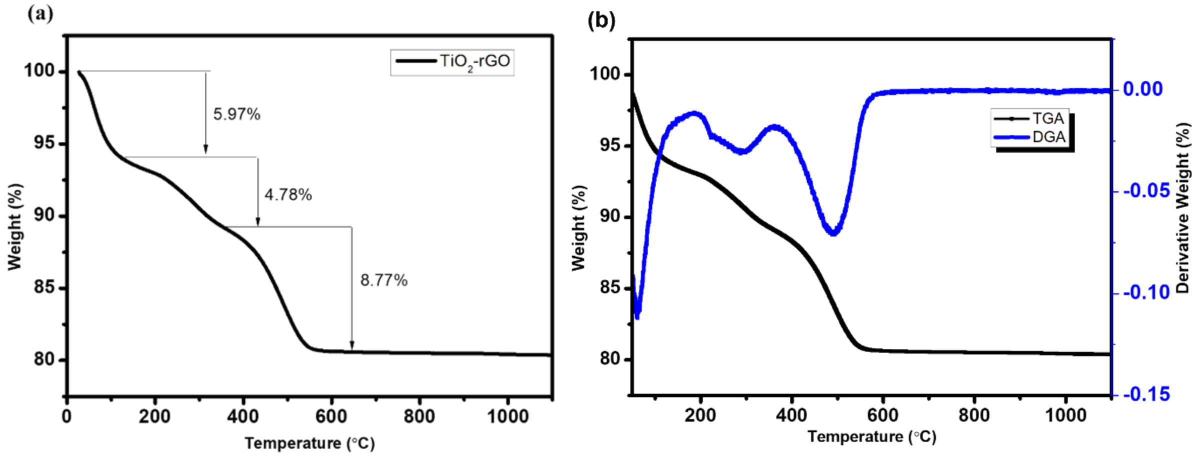

Fig. 4.4(a) TGA curve quantification and **(b)** TGA, DGA curves of TiO_2-rGO nanocomposite after heat treatment in air

The electrochemical performance of TiO_2-rGO nanocomposites was studied via cyclic voltammetry (CV) and galvanostatic charge-discharge (GCD) measurements to understand the electrochemical processes of charge storage occurring in the active material and its cyclic stability respectively. A CV of the TiO_2-rGO electrodes was performed using an MTI Corporation quick assembly split coin Cell in 1M $LiPF_6$ in EC/DMC (1:1 v/v) electrolyte and scanned at 0.1 mV s^{-1} over a potential range of 0 - 3 V versus Li/Li^+. The CV curves were recorded by an EC-Lab electrochemical workstation. The CV analysis of the TiO_2-rGO electrode was conducted to identify the storage mechanism(s) in the electrode. The shape of the CV showed both capacitive and faradaic behaviour due to observable rectangular CV shape and distinct peaks respectively. The faradaic peaks are reactions owing to Li^+ intercalation and de-lithiation into the active material. This is often referred to as a pseudocapacitive storage behaviour[209]. The CV curves **(Fig 4.5a)** showed that the lithiation and de-lithiation processes occurred over the potential range of 1 – 2 V with significant broad peaks observed at 2.1 V during the anodic scan and 1.3 V during the cathodic scan which corresponds to the changes in the valence states from Ti^{4+}/Ti^{3+} during Li^+ insertion/removal into and/or from TiO_2.

The galvanostatic charge-discharge (GCD) cycling of the TiO_2-rGO was performed with a CR-2032-coin cell made up of the TiO_2-rGO electrode as the working electrode, a Celgard separator and a Lithium disc as the counter electrode. The cell was assembled in an Argon-filled glove box with an oxygen concentration < 1 ppm and charged initially at a current density of 2 mA g^{-1} over a potential window of 0 - 2 V (vs Li^+/Li). The GCD data was recorded by a Deregellera charge-pack. TiO_2-rGO was first charged and discharged for 5 cycles at 0.2 mA g^{-}

^{1}. The discharge curve analysis showed a nearly linear voltage-time profile which depicts a pseudocapacitance storage mechanism from a combination of double layer capacitance and surface redox reactions. This calculated capacity exceeds that reported for TiO_2-rGO nanoparticles [231]. As a result, the as-synthesised TiO_2-rGO was further charged and discharged at different current densities to determine the rate performance of the nanocomposite (**Fig. 4.5c**), and for more cycles to evaluate its cyclic stability (**Fig. 4.5d**).

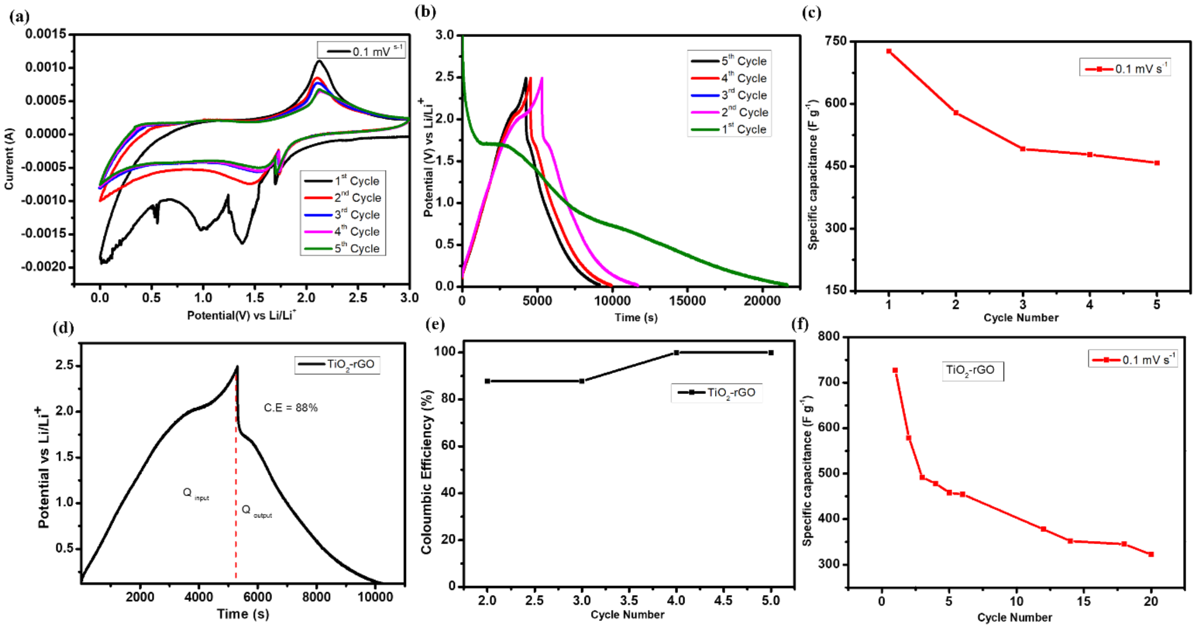

Fig. 4.5 (a) CV profile at 0.1 mV s^{-1} from 1st to 5th cycle of TiO_2-rGO electrode **(b)** GCD performance of TiO_2-rGO for 5 cycles **(c)** initial CV cycling performance of TiO_2-rGO electrode obtained at 0.1 mV s^{-1} **(d)** GCD plot showing C.E illustration **(e)** Coulombic efficiency of TiO_2-rGO and **(f)** CV cycling performance for 20 cycles at 0.1 mV s^{-1}.

The nanocomposite delivered a high capacitance of 727 F g^{-1} at 0.1 mV s^{-1}, which remained 63% of the initial value after 5 cycles of charge and discharge **(Fig. 4.5c)**. Further cycling of as-synthesised TiO_2-rGO electrode delivered up to 322 F g^{-1} after 20 cycles (**Fig. 4.5d**). The dispersion of hydrothermally grown TiO_2 nanoparticles on the surface of reduced graphene oxide sheets plays an important role in improving the specific capacity and cycle performance of TiO_2-rGO composite. This is evident in the observed improved electrochemical performance of TiO_2-rGO nanocomposites as compared to the control sample TiO_2. The control TiO_2 sample showed a lower capacitance of 169 F g^{-1} at 0.1 mV s^{-1} during the first cycle, and retained a capacitance of 56 F g^{-1} after 5 cycles of charge and discharge **(Fig. 4.6a-c)**.The dispersion of TiO_2 nanoparticles on rGO sheets (as seen in HRTEM images) also reduce the agglomeration of TiO_2 nanoparticles, and anchored on rGO sheets, thereby providing sites for electrochemical reactions to take place[214]. The good electrochemical performance of TiO_2-rGO can be attributed to the CHFS enhanced specific surface area, structural orientation, and structural stability of the nanocomposite during the cycling process.

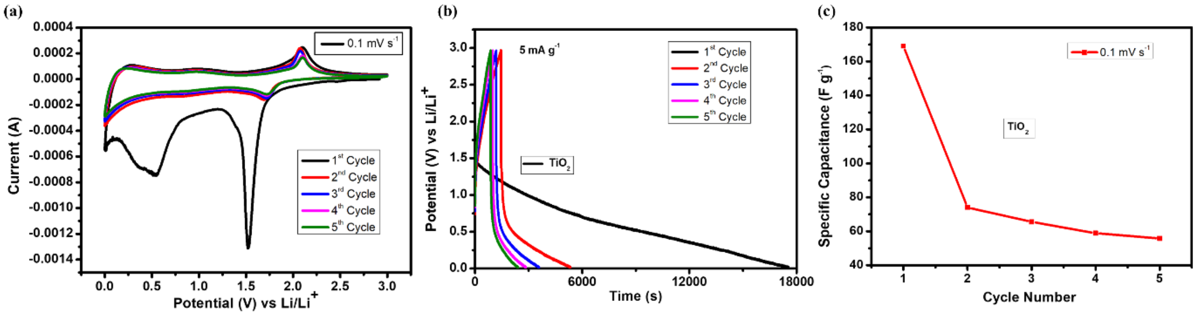

Fig. 4.6 (a) CV profile at 0.1 mV s^{-1} from 1st to 5th cycle of TiO_2 electrode **(b)** GCD performance of TiO_2 for 5 cycles **(c)** CV cycling performance of TiO_2 electrode obtained at 0.1 mV s^{-1}.Similarly, variation of the ratio of TiO_2 to rGO in the composites was conducted and tested for its electrochemical performance. Therein, the ratio of TiO_2 to rGO in the nanocomposites was 1:2. CV measurements obtained showed that 1:2 TiO_2-rGO delivered a capacitance of 130 F g^{-1} on the first cycle and 84 F g^{-1} after 5 cycles at 0.1 mV s^{-1} **(Fig. 4.7 a-c)**. This drop in performance is owing to the agglomeration of rGO nanosheets due to insufficient TiO_2 nanoparticles in the nanocomposite. This performance shows that TiO_2 nanoparticles are essential contributors to the electrochemical performance of TiO_2-rGO nanocomposites by keeping graphene sheets separated for access of electrolyte ions and storage of Li^+ ions.

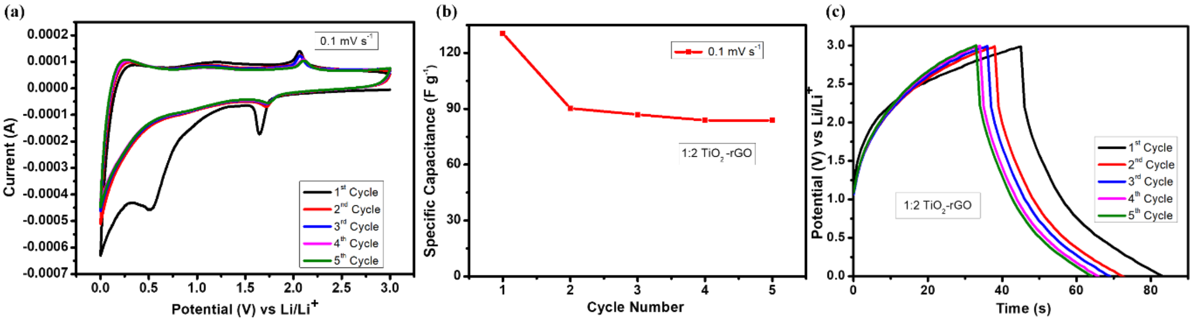

Fig. 4.6 (a) CV profile at 0.1 mV s^{-1} from 1st to 5th cycle of 1:2 TiO_2-rGO electrode **(b)** CV cycling performance of TiO_2-rGO electrode obtained at 0.1 mV s^{-1}. **(c)** GCD performance of TiO_2-rGO for 5 cycles

To evaluate the ratio of the charge removed (Q_{output}) to the charge used to restore the original capacity of the material (Q_{input}), it is represented by the term coulombic efficiency (C.E). It represents the ratio of the amounts of charge output to the charge input at a constant current charge and discharge process which helps to understand the reversibility of the electrode material and predict the lifespan of the electrode [232]. This was obtained from the GCD plot and evaluated using **Eq. 18**. The C.E obtained for TiO_2-rGO nanocomposites was 88% as shown in **Fig. 4.5e**.

$$C.E = Q_{output} / Q_{input} \qquad \text{Eq. (18)}$$

4.3. Conclusion

In summary, a TiO_2-rGO composite was produced via a continuous hydrothermal synthetic method as a green synthetic process route to produce in-situ; TiO_2 nanoparticles dispersed on the surface of rGO sheets. By combining the advantages of rGO and TiO_2, the as-synthesised nanocomposite was fabricated into electrodes and delivered a reversible capacity of 727 F g^{-1} after 5 cycles at 0.1 mV s^{-1}. This work demonstrates the use of TiO_2-rGO as a prospective energy storage material when used as a Lithium-ion battery anode.

Chapter 5: Continuous Hydrothermal Synthesis of MnO_2 and reduced Graphene Oxide as Nanocomposites Electrodes for Lithium-Ion Batteries

5.1. Introduction

Manganese (IV) oxide (MnO_2) is a transition metal oxide with high energy density and makes it suitable for application as components of electrode materials for supercapacitors. It is naturally abundant at a low cost with no environmental concerns[59]. These transition metal oxides have large capacitance and exhibit large redox reactions occurring at the surface of the electrodes. There have been several reports on synthesis of different morphologies of MnO_2; needles, rods and birnessite amongst others on the surface of graphene sheets. MnO_2 is a material with high theoretical capacitance of 1,380 F g^{-1}[79,233]. MnO_2 energy storage mechanisms includes reversible redox processes, cation adsorption-desorption and ion intercalation[79]. MnO_2 /Graphene (Gr) nanocomposites combine the electric double layer capacitance of graphene and the pseudocapacitance of MnO_2 to obtain improved capacitance values as compared to graphene-based electrodes.

Through a facile direct redox reaction between potassium permanganate and carbon nanotubes (CNTs), MnO_2 /CNTs were prepared by Wang and co-workers, and a specific capacitance value of 162 F g^{-1} at 0.2 A g^{-1} was obtained[68]. Other works have also been done such as dispersion of MnO_2 needles on the surface of GO where a capacitance of 197.2 F g^{-1} due to limited electronically conductive channels[80,234]. To enhance the electrochemical performance of MnO_2/rGO electrodes, a novel continuous hydrothermal synthesis of MnO_2 /rGO nanocomposite is introduced in this research to produce homogeneously dispersed MnO_2 nanoparticles on the surface of graphene sheets in a single step. This will possibly enable better electrical conductivity of graphene, increased surface area, decreased diffusion path, hence increasing the pseudocapacitive reaction and offer much improved capacitance[80,235].

Herein, MnO_2/rGO nanocomposites were synthesised through a continuous hydrothermal synthetic process described in Chapter 3, using respective material precursors in **Table 5**. The as-sythesised materials were collected, dried, analysed, fabricated into electrodes and tested for electrochemical performance. The samples; MnO_2, 1:1 MnO_2/rGO, 1:2 MnO_2/rGO and 1:3 MnO_2/rGO were labelled as **A**, **B**, **C** and **D** respectively.

5.2. Results and Discussion

MnO_2/Gr composite was prepared by a thermal and chemical oxidation of manganese (Mn^{2+}) in its metal salt with hydrogen peroxide to manganese (Mn^{4+}) in its oxide forms and a subsequent reduction of graphene oxide (GO) to reduced graphene oxide (rGO). The morphologies of the composites were observed by transmission electron microscopy (TEM) and scanning electron microscopy (SEM) in **Figs. 5.1 and 5.2** respectively. Details of the characterisation show needle-like MnO_2 nanoparticles with an average diameter of 15.71 ± 2.98 nm randomly dispersed across the surface of the graphene sheets. The graphene sheet is a thin sheet structure which may be folded with dispersions of MnO_2 nanoneedles around the sheet (Fig S4). These nanoneedles help to promote separation of the graphene sheets and helps to provide effective contact between the graphene sheets and MnO_2 needles to ensure effective transfer of electrolyte ions and electrons as an electrode material for a supercapacitor[235]. It is also observed that the MnO_2 nanoneedles also formed clusters when lower volumetric ratio of graphene oxide is used (**Fig. 5.1 b**). However, when higher volumetric ratio of GO was used MnO_2 nanoneedles are randomly distributed over the surface of graphene sheets (**Fig. 5.1d**). This provides an explanation that graphene sheets are needed to anchor MnO_2 nanoneedles. Graphene sheets have different functional groups such as epoxy, hydroxyl, carbonyl and carboxyl groups on their surface which serve as anchor sites for nanoneedle MnO_2 to adhere to their surface. MnO_2 also exhibit interconnected sheet-like morphology (forming a network like structure) as seen in the TEM images taken for Sample A (**Fig. 5.1a**) with an amorphous structure observed in its SAED pattern (**Fig. 5.1e**). The thickness of the nanoneedles were measured to be 12.73 nm, 18.5 nm, 12.7 nm and 18.9 nm in samples **A**, **B**, **C** and **D** respectively. In addition, needle-like morphology of MnO_2 is also found to be present in the TEM images **(Fig. 5.1)**, exhibiting a single crystalline diffraction pattern as seen in **Fig. 5.1f**. From the SAED pattern (**Fig. 5.1g**), it is observed that MnO_2/Gr has a polycrystalline structure due to presence of concentric circles. The hexagonal diffraction pattern of graphene can be confirmed on SAED when only graphene sheets without MnO_2 nanoneedles are examined under the electron microscope (**Fig. 5.3b**). An interlayer distance between sheets of graphene is measured from the edges to be 0.31± 0.06 nm (**Fig. 5.3c**) and an inter-atomic distance of 0.237± 0.029 nm on the surface of the graphene sheet (**Fig. 5.3a**). The HRTEM image of as-synthesised MnO2 nanoneedles gives an interplanar (d) spacing of 0.24 nm which corresponds to the 211 plane of tetragonal MnO_2[236,237] **(Fig. 5.4c**). These measurements were obtained using Image J software to analyse the TEM images.

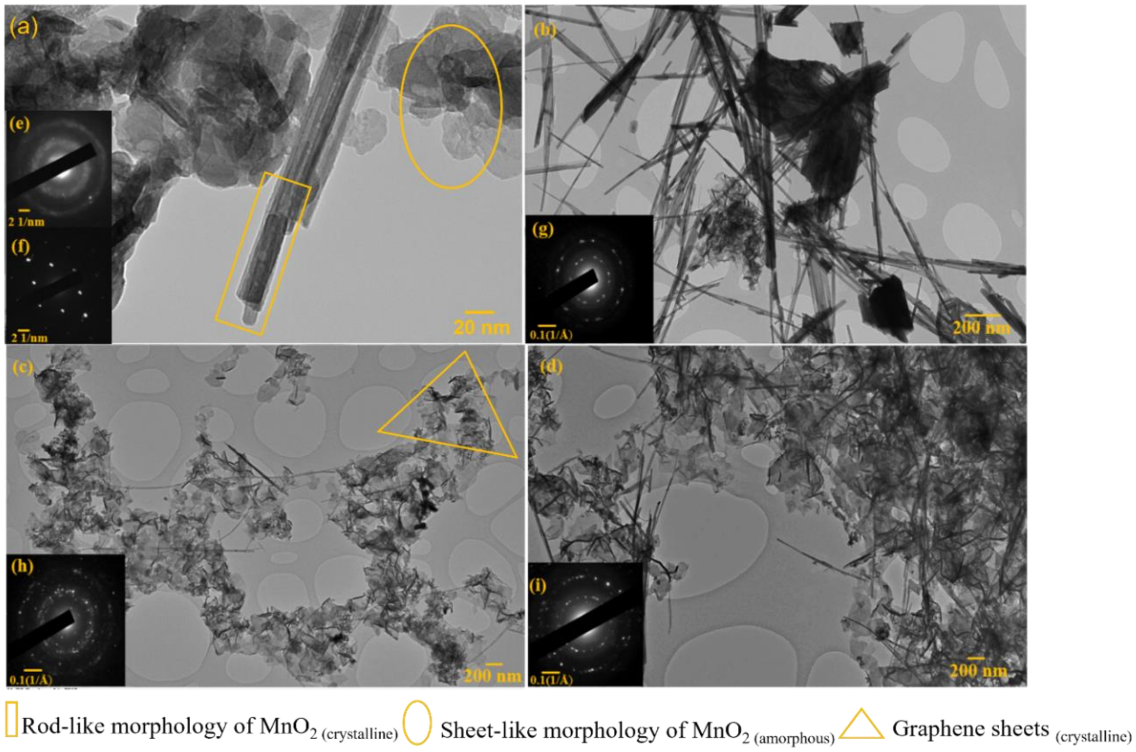

Fig. 5.1 Respective TEM and SAED images of **(a)** MnO_2 **(b)** 1:1 MnO_2/Gr **(c)** 1:2 MnO_2/Gr & **(d)** 1:3 MnO_2/Gr showing the sheet-like and rod-like morphologies of MnO_2, and graphene sheets in the nanocomposites

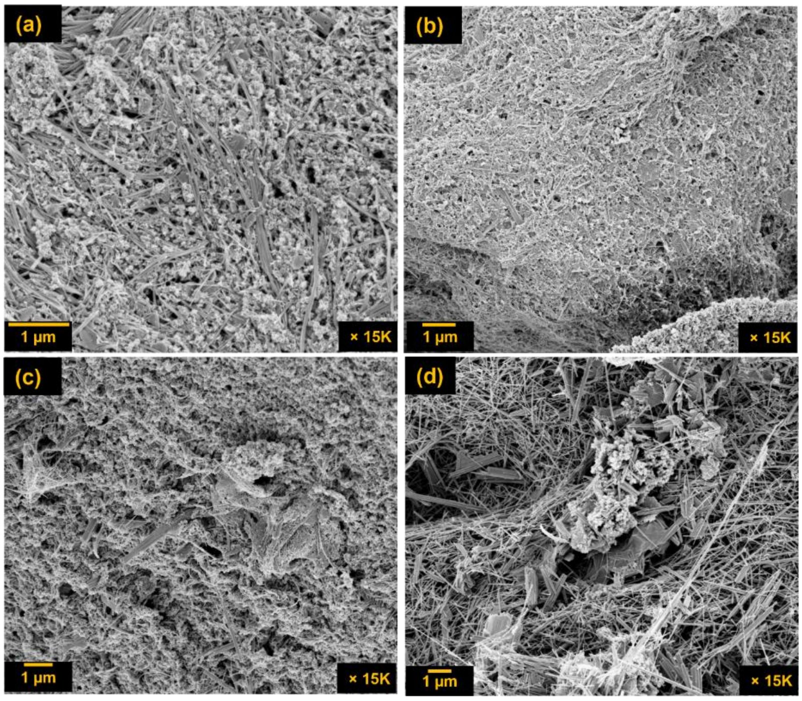

Fig. 5.2 SEM images showing morphology of **(a)** MnO_2 **(b)** 1:1 MnO_2/rGO **(c)** 1:2 MnO_2/rGO & **(d)** 1:3 MnO_2/rGO

The hexagonal diffraction pattern of graphene can be confirmed on SAED when only graphene sheets without MnO_2 nanoneedles are examined under the electron microscope (**Fig. 5.3b**). An interlayer distance between sheets of graphene is measured from the edges to be 0.31± 0.06 nm (**Fig. 5.3c**) and an inter-atomic distance of 0.24± 0.03 nm on the surface of the graphene sheet (**Fig. 5.3a**). The HRTEM image of as-synthesised MnO_2 nanoneedles gives an interplanar (d) spacing of 0.24 nm which corresponds to the 211 plane of tetragonal MnO_2[236,237] **(Fig. 5.4c**).

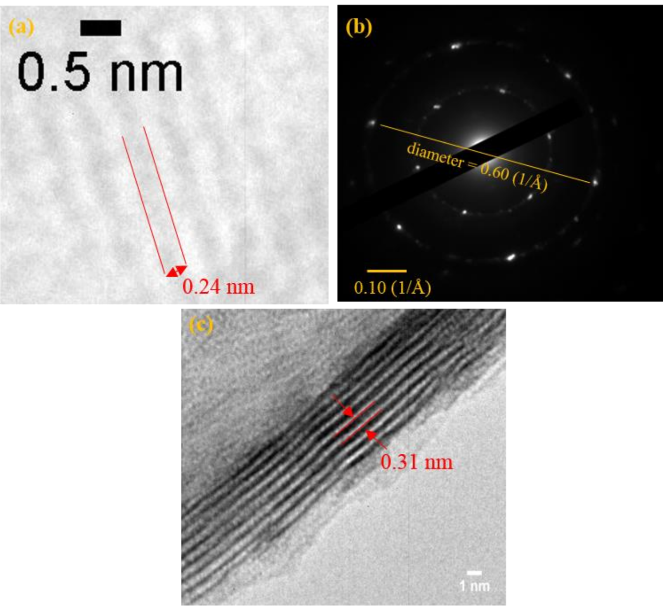

Fig. 5.3 HRTEM image of graphene sheet in sample B **(a)** under a high magnification (x400K) and **(b)** the corresponding SAED image **(c)** HRTEM image of stacked graphene sheets

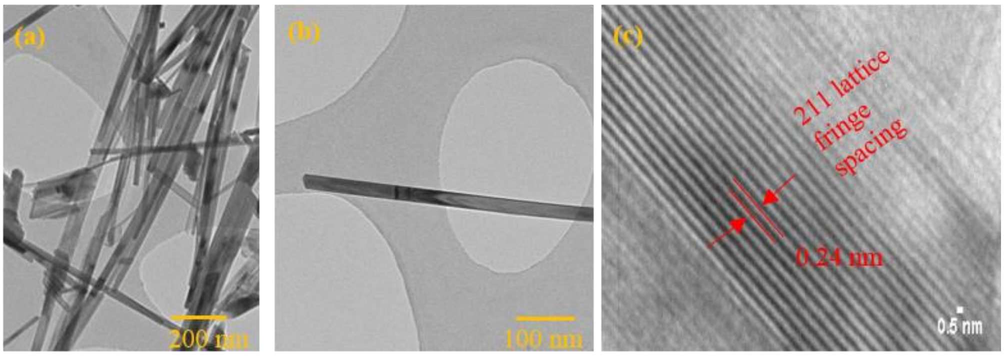

Fig. 5.4 (a), (b) TEM image of MnO_2 needles in sample B and **(c)** the corresponding HRTEM image.

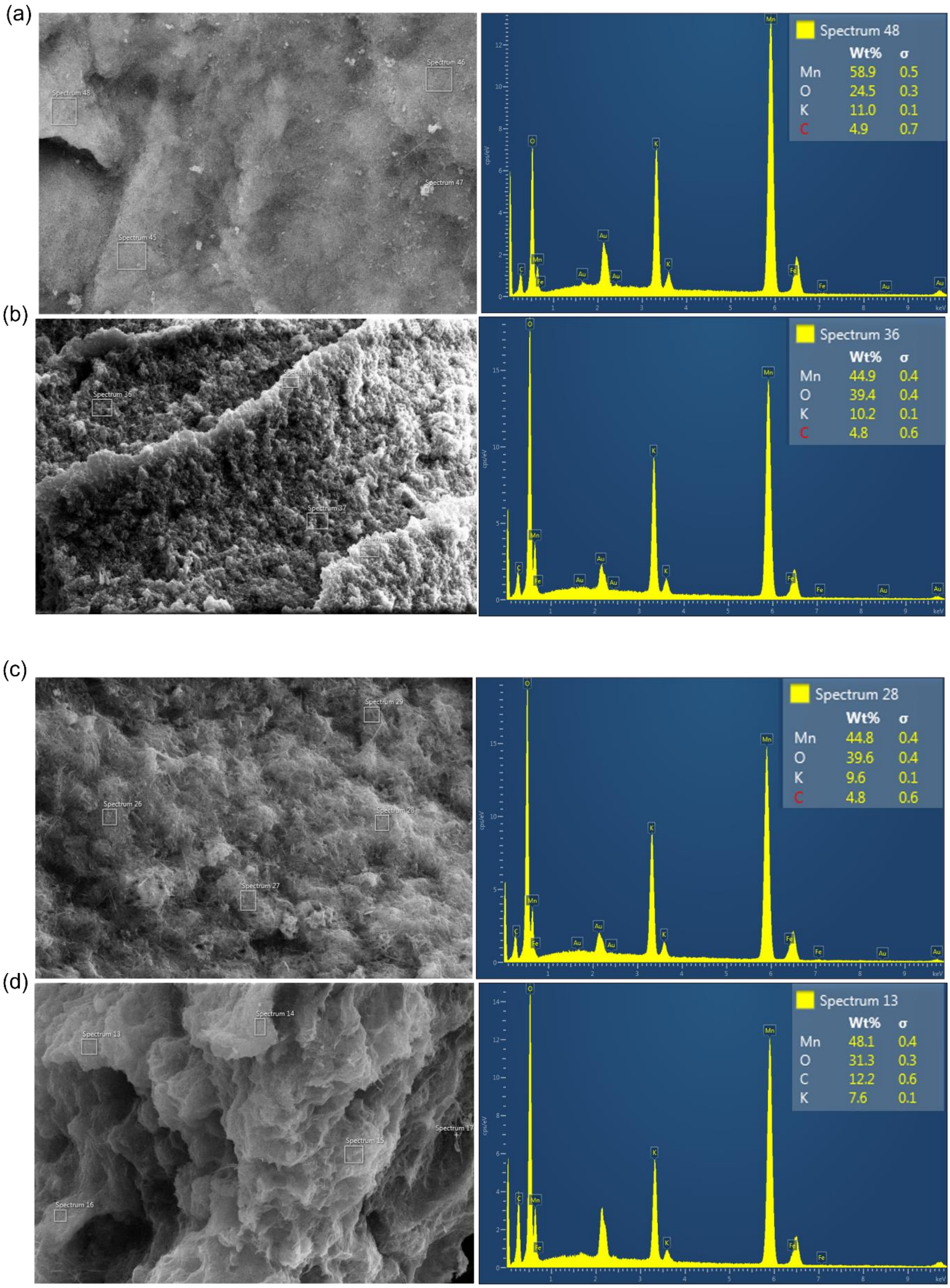

Fig. 5.5 EDS-SEM Images of **(a)** MnO_2 **(b)** 1:1 MnO_2-rGO **(c)** 1:2 MnO_2-rGO & **(d)** 1:3 MnO_2-rGO showing respective elemental mapping

SEM micrograph and Energy-Dispersive X-Ray Spectroscopy (EDS) analysis was also performed on all samples to determine chemical elements present in the sample (**Fig. 5.5**). It is observed that the percentage of carbon (C) increases with an increase in the volume ratio of graphene in the samples. The percentage of carbon in MnO_2 was from the preparation of the MnO_2 sample. The percentage elemental composition of manganese is also observed to decrease from MnO_2 to 1:1 MnO_2-rGO and 1:2 MnO_2-rGO, and 1:3 MnO_2-rGO composites. Potassium (K) is also present in sample from reactants used in synthesising samples (KOH). Gold (Au) peaks in sample is due to gold sputtering of samples prior to SEM analysis. Trace amounts of Iron (Fe) contamination is also observed in sample. However, its percentage composition in sample is negligible.

X-Ray Photoelectron Spectroscopy (XPS) analysis was performed for as-synthesised MnO_2-rGO composites as shown in **Fig. 5.6**. The XPS survey spectrum indicates that the materials are mainly composed of manganese, potassium, carbon and oxygen present in the samples. The manganese (Mn) signals in MnO_2-rGO samples indicate the anchoring of manganese oxide nanostructures on the functional groups present on the surface of graphene sheets through electrostatic forces[238]. There are three possible oxides that can be formed across the surface of graphene sheets. These include MnO, Mn_2O_3 and MnO_2 with oxidation states of +2, +3 and +4 respectively. The absence of satellite features at 647 eV confirms that no MnO is present in the samples[239]. A much narrower $Mn2p_{3/2}$ peak with an identifiable shape at the top of the peak (**Fig. 5.6a**) confirms the presence of MnO_2[239]. Further analysis shows the Mn^{4+} 2p3/2 peak centred at 641.88 eV and $Mn2p_{1/2}$ peak at 653.68 eV with a spin-energy separation of 11.8 eV, suggesting the formation of MnO_2. In addition to the curve fitting of Mn2p peaks, the Mn3s peak **(Fig. 5.6d)** splits into to peaks and their peak separation values can be used to elucidate the oxidation state[239].

Based on the calculated binding energy difference and identifiable shape at the top of Mn $2p_{3/2}$ peak, results show that the as-synthesised nanocomposites contain some Mn^{4+} suggesting the presence of MnO_2 nanoparticles[239].

The C_{1s} peak has a broad asymmetric tail which corresponds to high concentration of sp^2 carbon with a binding energy at 284 eV **(Fig 5.6c)**. The low intensity peak above 290 eV are also observed which are assigned to K_{2p} peaks due to potassium (K) present in the sample from the reagents used (KOH) **(Fig. 5.6b)**. There is a 14 % average concentration of K present in all samples.

(a) MnO_2

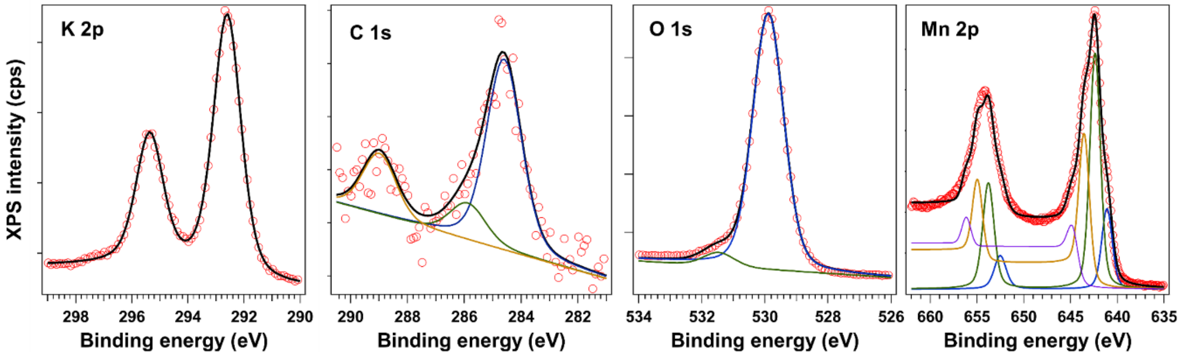

(b) 1:1 MnO_2-rGO

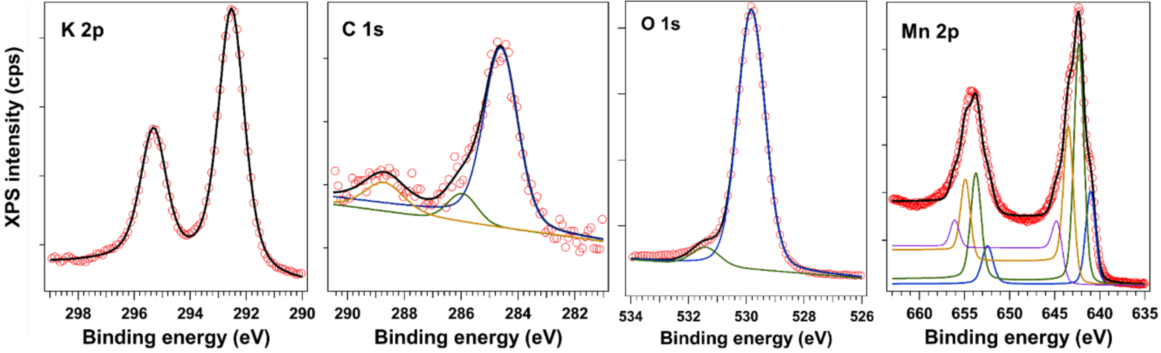

(c) 1:2 MnO_2-rGO

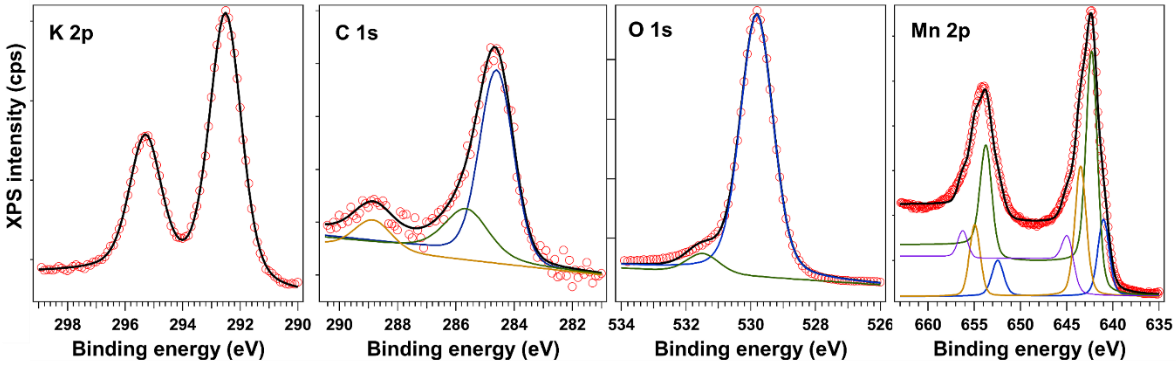

(d) 1:3 MnO_2-rGO

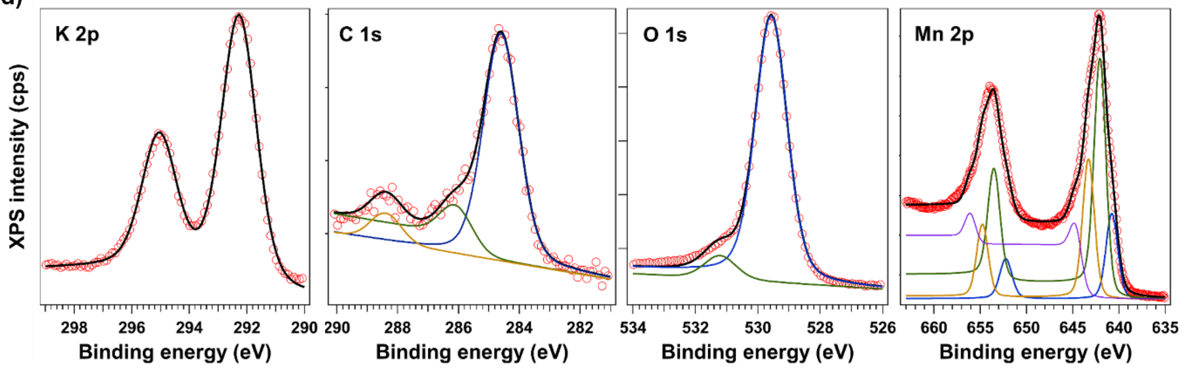

Fig. 5.6: XPS spectra showing Mn_{2p}, K_{2p}, C_{1s} and Mn_{2p} regions for the as- synthesised samples of MnO_2 and MnO_2-rGO nanocomposites (XPS data measured and fittings done by Dana Popescu, National Institute of Materials Physics, Magurele -Romania).

Table 7 showing the percentage elemental compositions in as-synthesised materials.

	MnO_2 (%)	1:1 MnO_2-rGO (%)	1:2 MnO_2-rGO (%)	1:3 MnO_2-rGO (%)
C 1s	1.8	3.3	3.9	4.8
O 1s	45.0	44.5	47.0	45.5
K 2p	12.2	14.1	12.0	12.0
Mn 2p	41.0	38.0	37.1	37.7

A summary of the elemental compositions of carbon, oxygen, potassium and manganese in all asynthesised materials is summarised in Table 7. Therein, the percentage composition of carbon increased as the mass ratio of graphene increased from 1 to 3 in the nanocomposite. Manganese on the otherhand had the highest ratio in MnO_2 nanoparticles, and decreased as the mass ratio of rGO increased. For further quantitative analysis, TGA and DGA curves **(Fig, 5.7a&b** respectively**)** of 1-3 MnO_2-rGO showed an initial mass loss of 8.77% between room temperature and 150 °C due to loss of surface water through evaporation and dehydration. A further mass loss of 7.44% was observed between 150 °C and 880 °C which is attributed to the phase transformation of MnO_2 to Mn_2O_3 and loss of carbonic structures in rGO to produce CO_2 and water vapour. From TGA analysis, the 1:3 MnO_2-rGO composite has a 16.21 % rGO composition. When compared to other samples, the TGA showed that more mass is lost from the sample as the amount of MnO_2 present in the sample increases (this is consistent with XPS data in Table 7). From the TGA, it is observed that 1:3 MnO_2-rGO and 1:1 MnO_2-rGO have the highest mass loss (3.6% and 1.3%, respectively) in the region between 150 °C and 880 °C due to phase transformation of MnO_2 to MnO_2O_3.The derivative plot **(Fig. 5.7b)** showed a further loss of carbonic structures, steam generation, and phase transformation of Mn_2O_3 to Mn_3O_4 at 883 °C.

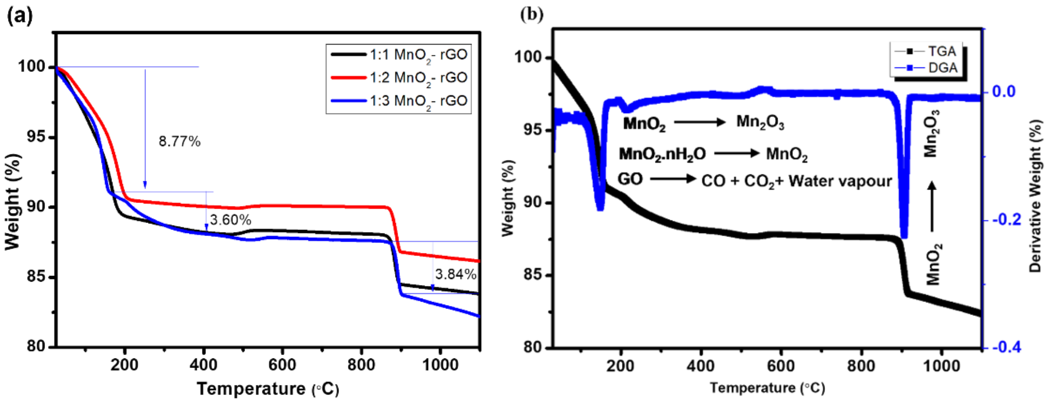

Fig. 5.7(a) TGA and DGA curves (b) TGA curve quantification of 1:3 MnO_2-rGO composite

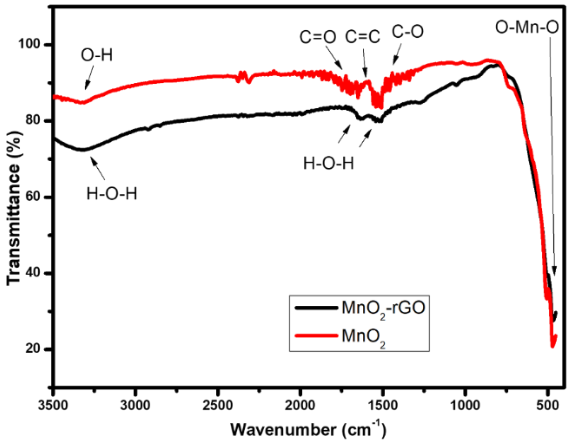

Fig. 5.8 FTIR spectra of MnO_2 & MnO_2-rGO

Fig. 5.8 shows the FTIR spectra of as-synthesised samples of MnO_2 and MnO_2/rGO to further confirm their compositions. Characteristic bands typical of rGO, for example; O-H broad peak due to OH stretching mode[127] at about 3400 cm^{-1} resulting from absorbed water molecules and alcohol groups. The band at 1750 cm^{-1} region is due to the C=O stretching vibrations of the carbonyl group. MnO_2-rGO spectrum also show a band at 1570 cm^{-1} due to C=C vibrations similar to unoxidized graphitic domain peak. Peaks at 1250 cm^{-1} represents C-OH stretch of alcohol group[127]. This FTIR spectrum also show how graphene oxide has been reduced by KOH to reduced graphene oxide (rGO). Typical oxides and hydroxides of metal nanoparticles show absorption peaks in the fingerprint region. The bands at 518 cm^{-1} and 480 cm^{-1} corresponds to Mn-O bending vibrations[240], while the broad band at 3400 cm^{-1} is the H-O-H stretching frequency and the weak bands between 1450 cm^{-1} and 1650 cm^{-1} are the H-O-H bending vibrations of the absorbed water molecule[241].

BET surface area analysis of all samples were determined by the adsorption and desorption of nitrogen gas on the surface of the material using BET theory of multilayer adsorption and desorption. Values of 98.59 m^2 g^{-1}, 39.82 m^2 g^{-1}, 54.37 m^2 g^{-1} and 65.59 m^2 g^{-1} were obtained for sample **A**, **B**, **C** and **D** respectively. The variation in observed BET surface areas could be due to the differences in particle morphology, aspect ratio and degrees of agglomeration that these materials exhibit.

Raman spectra below (**Fig. 5.9a**) shows the peaks of MnO_2 nanoparticles arising at 570 cm^{-1} and 634 cm^{-1}. The characteristic peak at 634 cm^{-1} is due to the MnO_6 symmetric stretching vibrations while the peak at 570 cm^{-1} is generally attributed to the Mn-O stretching vibration in the MnO_6 layer[240–243]. Characteristic D and G bands of graphene is not clearly visible in the spectrum. This can be either attributed to the laser wavelength used or due to the very low percentage of graphene present in samples.

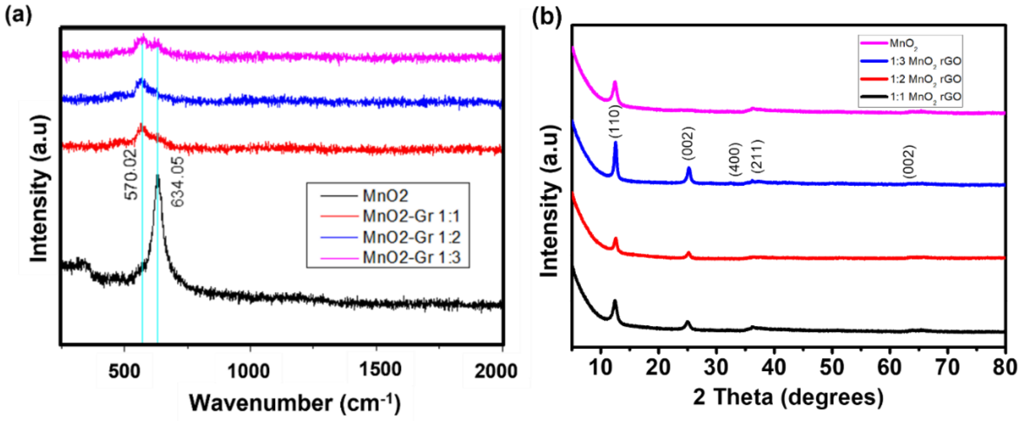

Fig. 5.9 (a) Raman scattering and **(b)** XRD patterns showing molecular vibrations and phase compositions of MnO_2 and MnO_2-rGO composites respectively

XRD characterisation of MnO_2 and MnO_2-rGO materials were conducted to analyse the crystal phase of the samples **(Fig. 5.9b)**. Diffraction peaks at 2θ values of 12.57, 36.3 and 37.2 that are attributed to (110), (400) and (211) crystal planes respectively. These diffraction peaks are ascribed to that of α- MnO_2 crystal phase of the tetragonal crystal system (JCPDS Card No: 44-0141).

In order to study the electrochemical properties of rGO and MnO_2 in the nanocomposites, the sample with the highest rGO ratio and surface area **(Sample D)** was selected. The as-synthesised MnO_2 and MnO_2-rGO nanocomposite (1:3) was prepared into a slurry and rolled on Cu foil. Using Li disc as a counter electrode and MnO_2-rGO as the working electrode, the cell was assembled in a two-electrode split cell configuration with 1M $LiPF_6$ in EC/DMC (1:1 v/v) electrolyte for electrochemical analysis via cyclic voltammetry and galvanostatic charge-discharge techniques.MnO_2-rGO showed an almost rectangular current-potential CV shape indicating a capacitive behaviour of the nanocomposite (**Fig. 5.10a**). The deviation from a rectangular shape was due to faradaic pseudocapacitance contribution from MnO_2. The specific capacitance of the nanocomposite was calculated using **Eq.16**. The nanocomposite showed a specific capacitance of 9 F g^{-1} and stabilised at 6 F g-1 after 5 cycles at a scan rate of 0.5 mV s^{-1}. The low specific capacitance value of as-synthesised MnO_2-rGO 1:3 can be attributed to the aggregation of rGO sheets which limits electrochemical activity of MnO_2-rGO nanocomposites. This agglomeration is observed in the TEM images of MnO_2-rGO nanocomposites (Fig. 5.1b-d), and can also limit the pseudocapacitive performance of MnO_2 in the nanocomposite due to limited access to intercalating ions during charge and discharge processes. This result also agrees with reported literature where the electrochemical performance of MnO_2 based electrodes has been observed to decrease owing to the low conductivity of MnO_2[244]. Typically, a large voltage window helps to increase the specific energy of the pseudocapacitor. However, the large potential range of 0 – 3 V used could limit the reversible lithiation and de-lithiation process of MnO_2- rGO electrode, thereby reducing its capacitive performance. This is also evident in literature studies as most potential range used are between a narrow window of 0 and 1 V, where MnO_2-rGO are electrochemically stable[245,246]. The poor performance of the as-synthesised MnO_2-rGO could also be attributed to variation in morphology which affects the surface properties such as access to surface area and electrochemically active sites that contributes to the overall performance of the electrode material. Past studies have also reported low capacitance values for hydrothermally synthesised MnO_2-rGO composites where no distinct redox peaks were observed. The GCD is shown in **Fig. 5.10c**, where a non-linear GCD curve with no plateau is observed, demonstrating a pseudocapacitive behaviour of MnO_2-rGO nanocomposite and a capacitance retention rate of 62% after 5 cycles **(Fig, 5.10b)**. Also, the GCD curve **(Fig. 5.10c)** show some deviation from linearity within 1.0 -1.5 V before returning to a linear behaviour. Such reactions could be parasitic which affects the capacitance of the electrode material.

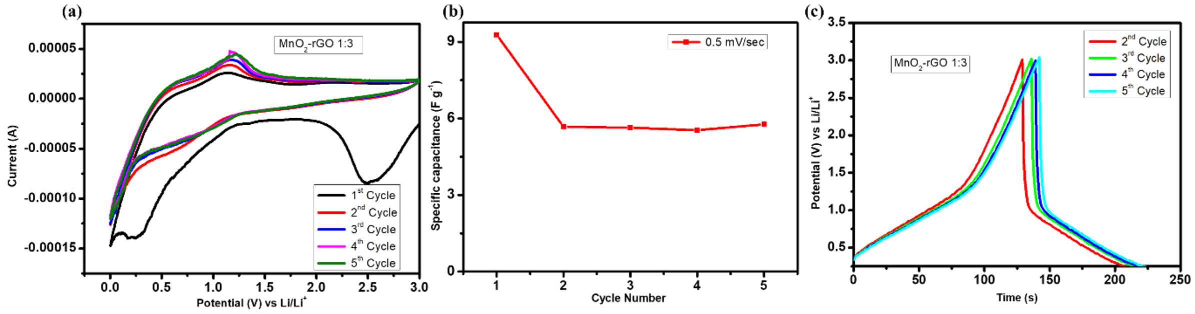

Fig. 5.10 **(a)** Cyclic voltammetry at 0.5 mV s^{-1} **(b)** Cyclic stability of MnO$_2$-rGO 1:3 **(c)** Galvanostatic charge-discharge curves of MnO$_2$-rGO 1:3.

The CV curves of MnO$_2$ nanoparticles is shown in **Fig. 5.10b** obtained at 0.5 mV s^{-1} within a potential window of 0 to 3 V. The CV curve is generally rectangular indicating a capacitive behaviour during the charge and discharge cycles. Also observed in the CV curves are redox peaks attributed to the faradaic reactions of MnO$_2$[247]. The specific capacitance was calculated using Eq. 16. The area under the CV curve showed that CHFS synthesised MnO$_2$ nanoparticles had a specific capacitance of 36 F g^{-1}. This value exceeds that of 1:3 MnO$_2$-rGO owing to the absence of agglomerated rGO sheets, thereby allowing pseudocapacitive process of MnO$_2$ electrode to occur which contributes to its specific capacitance. The GCD curves also show a deviation from linear voltage-time relationship also indicating pseudocapacitive behaviour of MnO$_2$ which is in accordance with the redox peaks observed in the CV curves.

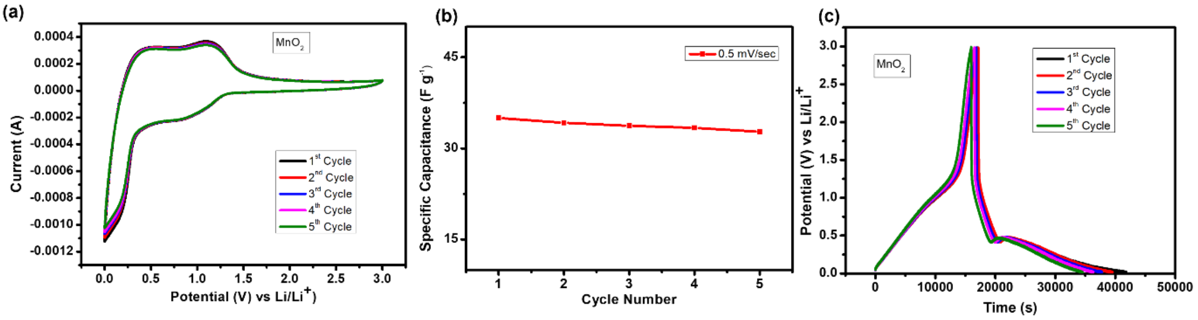

Fig. 5.11 **(a)** Cyclic voltammetry at 0.5 mV s^{-1} **(b)** Cyclic stability of MnO$_2$ **(c)** Galvanostatic charge-discharge curves of MnO$_2$

5.3. Conclusion

In summary, a novel experimental study was carried out to synthesize MnO_2 and MnO_2-rGO nanoparticles via continuous hydrothermal flow synthesis approach. Different volumetric ratios of MnO_2 and graphene oxide solutions were used to investigate changes in their morphology and chemical composition, that could improve its electrochemical performance. MnO_2-rGO in a 1:3 volumetric ratio showed more anchored MnO_2 nanoneedles on the surface of graphene sheets. This also showed that more graphene concentration prevented aggregation of MnO_2 into clusters as observed in the SEM images of 1:1 MnO_2-rGO nanocomposites. Despite the successful synthesis of MnO_2-rGO nanocomposites through a continuous hydrothermal process, its electrochemical performance was quite poor owing to the low conductivity of MnO_2 and inaccessible active sites for electrochemical reactions such as lithiation and de-lithiation processes to take place. Agglomeration of MnO_2 needles was observed from SEM and TEM images which limits the performance of the nanocomposites. To explore more on the as-synthesised nanomaterials, future works and recommendations are provided below.

Chapter 6: In-situ Continuous Hydrothermal Synthesis of TiO_2 Nanoparticles on Conductive N-Doped MXene Nanosheets for Li-Ion Storage

Declarations: This chapter has been published. Information bout co-authors is stated on page xiii

6.1. Introduction

The small ionic size, low molecular weight and density of lithium makes it suitable to intercalate into layered materials. These processes of intercalation and de-intercalation of lithium ions into electrode materials contributes to the high energy density and excellent cycling stability of lithium-ion batteries (LIBs), making LIB technology one of the dominant current battery technology. [248,249]. The light weight of lithium and its ease of intercalation offers LIBs high volumetric energy density. Despite these exciting properties, costs, power performance, safety and environmental concerns of the components of LIBs are the problems facing the LIB industry.

Through shuttling of lithium ions from the cathode to the anode and vice-versa during charge and discharge, energy is stored in the LIB. A typical LIB comprises of three components; the anode (usually graphite), the cathode (typically lithium metal oxides, e.g., $LiCoO_2$), and an electrolyte (non-aqueous) that allows for reversible lithiation and de-lithiation over a wide potential range. Lithium metal oxides (LMOs) as cathode materials offer high chemical potential (vs Li/Li^+), while graphite as an anode material is naturally abundant, low cost, and has a layered structure suitable for intercalation[250].

Carbon-based (graphite) LIBs have long cycles of charge and discharge. However, cyclic performance is challenged by the use of standard polymeric binders in the electrode fabrication process. Example of such binders are poly (vinylidene difluoride (PVDF); a poly-fluoroalkyl (PFA) compound classified as a "forever chemical" due to its longevity in the environment. In the electrode fabrication of LIBs, the use of N-methyl-2-pyrrolidone (NMP); a toxic solvent is employed in slurry processing the electrodes[251–254] which negatively impacts both the environmental friendliness and cost of battery manufacturing currently.To eradicate this problem of forever chemical usage, an aqueous processing of MXenes into a stable colloidal suspension is employed. The negatively charged MXene sheets enables preparation of stable colloidal MXene suspension which enables its application as Li-ion anodes as a potential means to eliminate forever chemicals from the fabrication process of LIB electrodes. [255–257].

To overcome this, the solution is MXene. MXenes have high electronic conductivity (6500 S cm^{-1}), enabling them to serve as an active material and a current collector[12,48]. Examples of MXenes include $Ti_3C_2T_x$, Ti_2CT_x, Ti_3CNT_x, $Nb_4C_3T_x$, etc. [48,99]. Reversible redox reactions occurring at the titanium surface (Ti) in MXenes provide a pseudo-capacitance, thereby increasing the faradaic performance of a MXene electrode[103]. A tapped density of 4 g cm^{-3} exhibited by MXenes reduces the electrode's mass loading compared to 2D graphene (0.4 g cm^{-3}). A reported high volumetric capacitance of up to 900 Fcm^{-3} in MXenes attracts increasing interest in energy storage applications[12,48]. In addition, MXenes enable aqueous processing due to its excellent hydrophilic surface. This eliminates the use of toxic electrode processing solvents such as NMP. However, the stability of MXenes in an aqueous solution, re-stacking of its nanosheets, and limited control of its surface functionalities limit the full use of its properties. A potential solution is through the surface and chemical functionalisation of 2D MXenes with metal oxides such as titanium (iv) oxide (TiO_2) or doping with heteroatoms such as nitrogen[43]. The growth of TiO_2 nanoparticles between MXene sheets prevents re-stacking, thereby keeping sheets separated. During the doping process, the dopant (nitrogen) behaves like an electron donor. It replaces carbon in the crystal lattice of the semiconducting material by generating an extra valence electron in modulating the conductivity of the semiconductor material.

As such, the development of more environmentally sustainable electrode compositions must be progressive that utilise the excellent hydrophilic surface properties of MXenes in aqueous processing and electrode fabrication to eradicate the use of toxic organic solvents[199].

When MXenes are oxidised during exposure to water, air or heat treatment, titania (TiO_2) is produced on the surface of MXenes. This oxidation process is uncontrolled and undesired. Titania is naturally abundant, non-toxic and inexpensive[84]. TiO_2 is often explored as in various applications such as energy storage[200,201] photocatalysis[86,202,203] and water treatment[202,203]. The volume expansion ($<4\%$) of TiO_2 during lithiation process contributes to its long life cycle. [204,258,259]. However, TiO_2 is challenged in performance by its poor electrical conductivity and sluggish Li-ion diffusion within the material[204,205]. To overcome this challenge, exploring nano-TiO_2 is a potential route to improve the surface area and reduced diffusion distance for Li-ion transport compared to bulk materials[204]. Furthermore, combining TiO_2 nanoparticles with highly conductive 2D materials such as MXenes has the potential to boost performance significantly while simultaneously eliminating the need for conventional fluorinated polymeric binders[204].

Through a unique route of synthesis, advanced modifications of 2D materials by varying morphologies, improving surface area and surface functionalisation can be used as an advantage. These modifications change the material structure by size tuning and engineering defects in the material, thereby causing a change in the electronic and optoelectronic properties[39]. Furthermore, it is advantageous to combine the properties and modified functionalities of 2D MXenes and TiO_2 nanoparticles as electrode materials to enhance electrochemical performance, as stand-alone materials do not have enough properties to render practical functions. Despite these exciting technologies, the current approaches in the synthesis of materials face challenges, including toxic precursors, non-uniformity of particle size distribution, lengthy manufacturing time, and energy costs. Due to this, there is a need to adopt synthetic strategies that overcome these challenges by providing a rapid, clean and scalable material synthesis process while delivering high-performance materials.

Continuous Hydrothermal Flow Synthesis (CHFS) is employed here as a favorable methodology that offers a single-step process of delivering water-soluble precursors with a flow of supercritical water at 374 °C and 22.4 MPa for homogeneously producing highly crystalline nanostructures[39,164,166,260]. This method exploits the properties of supercritical water, such as its reduced dielectric constant and increased dissociation to H^+ and OH^- ions which facilitate the rapid synthesis of various metal oxides through hydrolyses, dehydration, and precipitation[171]. CHFS methodology delivers fine particles, single crystals, and metal oxides by controlling the reaction medium's viscosity, density, and dielectric constant through changes in the reaction temperature and pressure. This hands-on approach offers control over the particle size, morphology, and crystal structure of as-synthesised materials[12,166,171,173,261]. Compared to traditional methods, CHFS saves time (within a fraction of a second) and energy in delivering quality and reproducible homogenous materials[163,167,261–263]. In addition, the CHFS process has a low environmental impact, as shown in the synthesis of graphene quantum dots[33].

6.2. Results and Discussion

Firstly, Ti_2C MXene was prepared via method described and detailed in methodology chapters. The SEM images of the starting MAX phase material, etched Ti_2C and delaminated Ti_2C MXene are shown in **Fig. 4.1 (a), (b) and (c)** respectively.

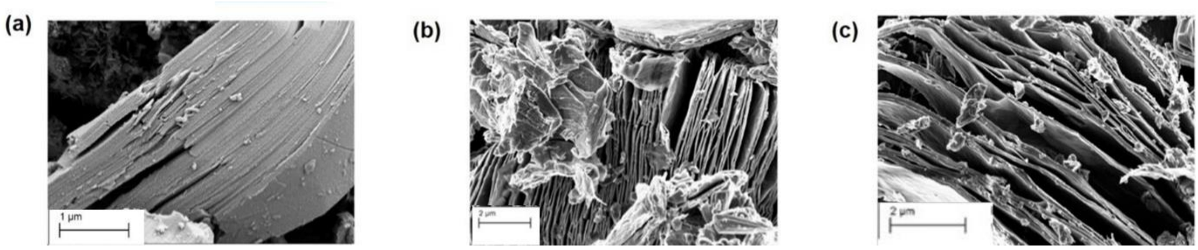

Fig. 6.1 SEM images showing **(a)** starting MAX phase material **(b)** *m*-MXene **(c)** *d*-MXene

A rapid synthesis approach that delivers MXenes (also served as TiO_2 precursor) and ammonia (N-source) continuously into a supercritical environment in synthesising N-doped MXenes decorated with TiO_2 nanoparticles was explored. The as-synthesised materials were collected and characterised for various analyses.

SEM and TEM analyses were used to investigate the effect of the hydrothermal treatment on the structure and morphology of Ti_2C and TiO_2. As shown in the SEM images **(Fig. 6.2)**, as-prepared N-MXene/TiO_2 (NMT) composites exhibit accordion-like and separated sheet structures with spherical nanoparticles distributed across the surface of the sheets. These nanoparticles were formed in both NMT350 and NMT450 samples due to the supercritical environment created during hydrothermal treatment at 350°C and 450°C, which can be related to the oxidation of MXene to TiO_2.

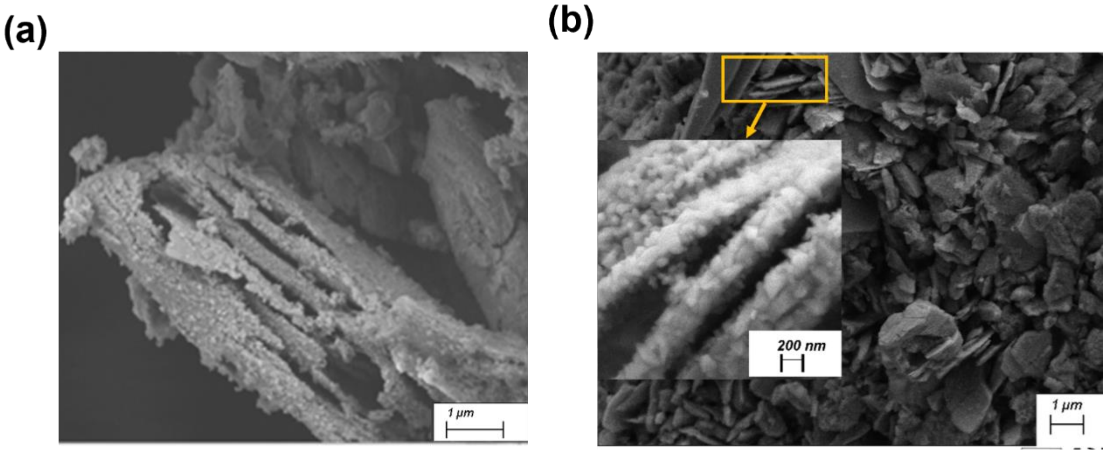

Fig. 6.2. SEM images of (a) NMT nanocomposites at different reaction temperatures showing (b) spherical TiO_2 nanoparticles formed on the edges of MXene sheets

The surface of the MXene sheets appears rough after hydrothermal treatment due to the formation of spherical nanoparticles on its surface compared to pre-treated delaminated MXenes **(Fig. 6.1c).** Oxidation of MXene sheets starts from the edges due to the presence of these spherical nanoparticles around the edges (inlet **Fig. 6.2**), which later extends to the core as reaction temperature increases to 450°C. The structure of the N-doped MXene/TiO_2 (NMT) composites shows a sandwich arrangement with TiO_2 nanoparticles embedded in between MXene sheets. This arrangement helps keep MXene sheets separated, thereby making them accessible for intercalation of Li^+ ions and promoting its surface area access to electrolyte ions.

A variation of morphologies such as cubes, sheets and spheres were observed in the TEM images of NMT hybrids. The high-resolution (HRTEM) images and measurements of lattice fringes show a random distribution of anatase TiO_2 nanoparticles on the MXene sheets in a sandwich arrangement **(Fig. 6.3)**. This observation confirms the conversion of MXenes to TiO_2 during the continuous hydrothermal treatment. HRTEM images further show that Ti_2CT_x exists in single and few-layered nanosheets with TiO_2 nanoparticles grown on the surface of MXene and amorphous carbon **(Fig. 6.3g)**. HRTEM also reveals the lattice planes of anatase TiO_2, Ti_2C MXene, and carbonaceous carbon **(Fig. 6.3b, 6.3d & 6.3f)** with parallel fringe spacings of 0.35 nm and 1.30 nm for TiO_2 and Ti_2C MXene which agrees with SEM and XRD results. TEM images also reveal the flake-like morphology of MXene with TiO_2 nanocrystals nucleated on its surface, with amorphous and crystalline carbonaceous carbon also present. A d-spacing of 0.33 nm is also measured in the HRTEM image, which can be attributed to graphitic carbon[155]. The selected area electron diffraction (SAED) pattern shows that MXene retained the hexagonal diffraction spots (inlet image in **Fig. 6.3c**)[34,249,264,265].

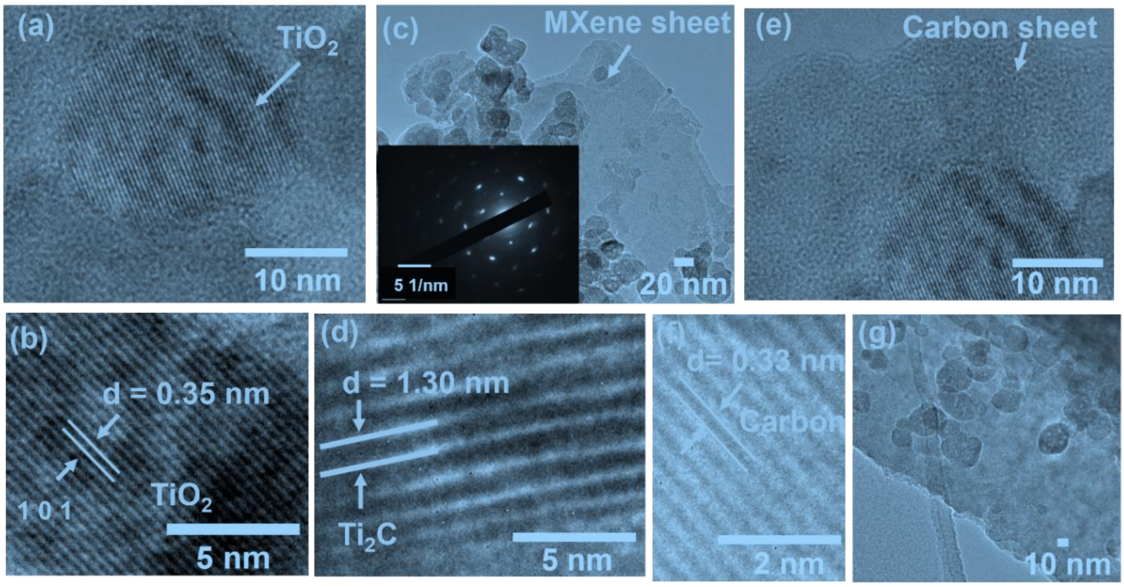

Fig. 6.3 (a-b) & (d-f) HRTEM images **(c)** TEM and **(c inlet)** SAED pattern of NMT nanocomposites showing lattice fringes of Ti_2C and TiO_2

XPS analysis was carried out to determine the elemental composition and surface chemistry of the NMT nanocomposites. The acquired survey spectrum **(Fig. 6.4a)** for each sample shows the presence of titanium (Ti), carbon (C), nitrogen (N), oxygen (O), and fluorine (F). The High-resolution Ti 2p spectrum of NMT samples was fitted with four doublet pairs (Ti $2p_{3/2}$ and Ti $2p_{1/2}$) with a fixed area ratio equal to 2:1 and a doublet separation of 5.7 eV, note for clarity, the fits of the Ti 2p spectra are shown offset from the photoelectron speaks after subtraction of a Shirley background. The Ti $2p_{3/2}$ components are positioned at 458.9 eV, 458.0 eV, 455.7 eV and 454.6 eV. The Ti $2p_{3/2}$ component centred at 458.9 eV is dominant associated with Ti^{4+} ions, indicating the presence of TiO_2, and the lower binding Ti $2p_{3/2}$ component at 458.0 eV is associated with reduced charge state titanium ions (Ti_xO_y). The Ti $2p_{3/2}$ component centred at 455.7 eV represents sub-stoichiometric titanium oxides or oxycarbides, and the Ti $2p_{3/2}$ component centred at 454.6 eV is assigned to Ti-C bonds present in the composites[226,266]'[267]. Ti_2C was not completely converted to TiO_2; this can be seen in the XPS spectrum of C1s core level showing the presence of Ti-C bonds due to component located at 281.1 eV along with other components at 288.6 eV, and 284.7 eV corresponding to (O-C=O and C-F), C-O and C-C (sp_2) bonds respectively[226,268]. The presence of the N 1s signal further confirms the exciting chemistry of functionalising MXene using CHFS via doping with nitrogen atoms to enhance its electronic properties. The high-resolution N 1s spectrum could be fitted with two peaks centred at 400.8 eV and 399.1 eV corresponding to protonated pyridinic nitrogen and pyrrolic nitrogen respectively[261,269]. An absence of Ti-N peaks at 350 °C indicates that the nitrogen doping process did not begin until about a temperature of 400 °C **(Fig. 6.4a & 6.4c)**. Elemental analysis **(Fig. 6b)** shows that NMT nanocomposites contain an approximate average of 42.50 wt % oxygen, 29.50 wt % carbon, 20.73 wt % titanium, 2.30 wt % aluminium, 1.87 wt % nitrogen, 2.42 wt % fluorine, and 0.62 wt % chlorine, confirming that NMT nanocomposites are nitrogen-doped and carbon-rich.

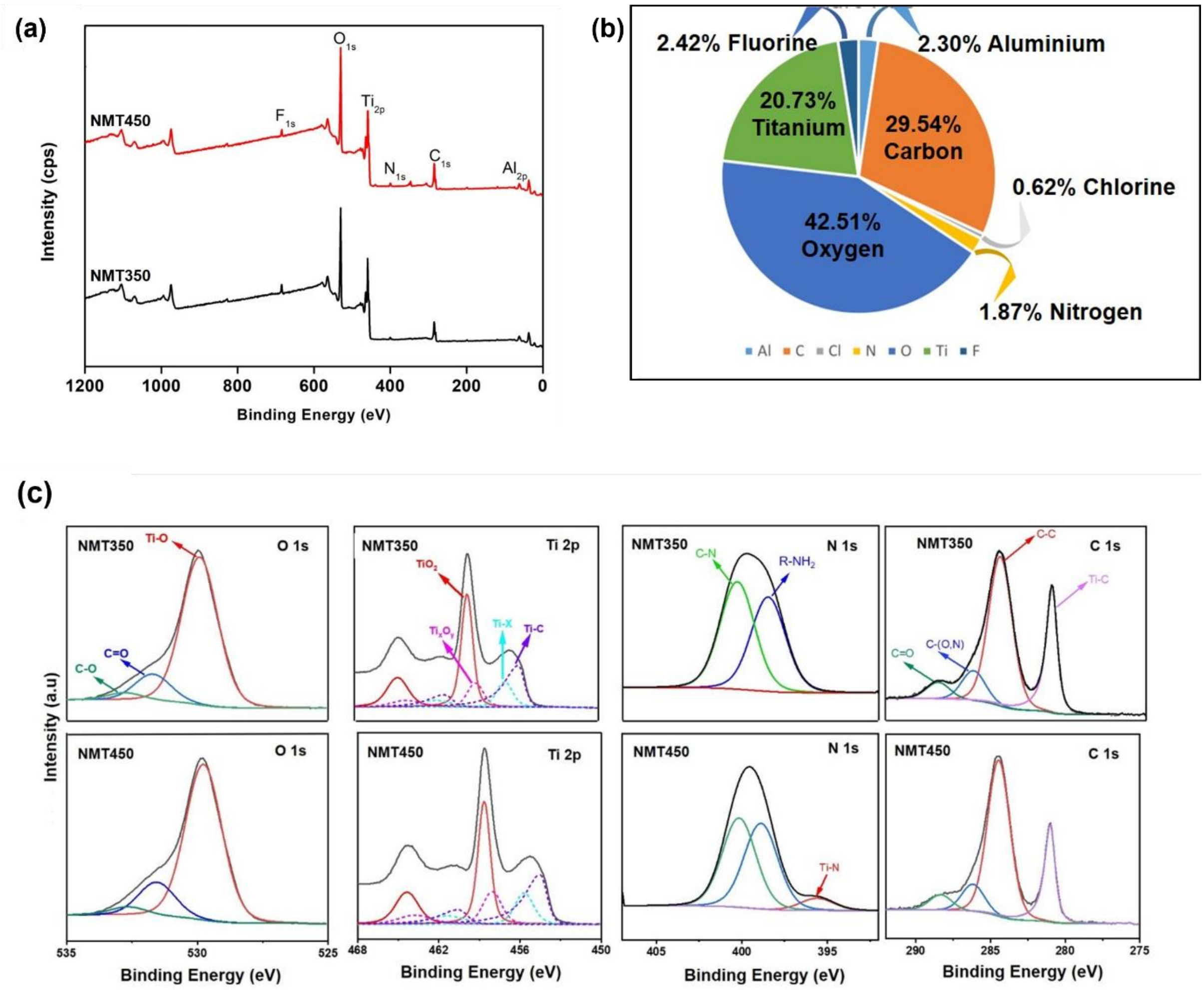

Fig. 6.4. (a) XPS survey scans **(b)** XPS elemental quantification **(c)** High-resolution spectra of C(1s), N(1s), O(1s) and Ti(2p) core levels showing the chemical bonding states in NMT nanocomposites (Measurements and fittings done by Dr. David Morgan)

To determine the crystalline phase structures, present in the NMT nanocomposites and the effect of hydrothermal treatment on the d-spacing of Ti_2C, XRD analysis **(Fig. 6.5a)** was carried out. Relatively sharp diffraction peaks of crystalline TiO_2 were observed at 2theta = 25.3°, 37.2°, 47.8° and 54.1°, which corresponds to the (101), (004), (200), and (105) peaks of anatase TiO_2 (JCPDS Card no. 21-1271)[226,268,270]. The intensity of these peaks (especially 101 peaks) can be observed to increase as temperature increases from 350 °C to 450 °C, indicating more TiO_2 being formed. However, the (002) peak of Ti_2C MXene shifts to a lower angle of 2 theta = 7° as compared to the starting material (*d*-MXene), indicating an increase in interlayer distance resulting from TiO_2 formation in between MXene sheets after heating[264]. A peak at 14.5° is also observed and can be attributed to carbonaceous carbon. According to the Scherrer equation, the average size of TiO_2 nanoparticles in NMT350 and NMT450 is 32 nm and 34 nm, respectively. The XRD pattern also shows that the (002) diffraction peaks of Ti_2AlC broadened with a shift towards lower angles, indicating an increase in *d*-spacing in the MXene sample due to removal of Al layer. In addition, (002) peak is the dominant peak, indicating the majority of the NMT nanocomposite is the MXene phase.

To observe the change in the electronic properties and vibrational modes of untreated Ti_2C and NMT nanocomposites, the Raman technique was used. The Raman spectra below **(Fig. 6.5b)** show the constituents of the prepared samples. A prominent Raman peak centred at 149 cm^{-1} corresponds to anatase TiO_2, whose intensity increases as temperature increases, signifying more TiO_2 formation[265],[270]. Also shown are three Raman peaks centred at 250 cm^{-1}, 410 cm$^{-1,}$ and 612 cm^{-1} attributed to vibrations from Ti_2C[271]. These peaks are observed to exhibit a redshift as temperature increases owing to thinning of MXene layers. D and G peaks at 1347 cm^{-1} and 1588 cm$^{-1,}$ respectively, indicate the formation of graphitic carbon during the hydrothermal process, which increases with temperature[268]. The G band is attributed to the E_{2g} vibration modes of sp^2 carbon atoms associated with the graphitic core, while the D band represents the sp^3 carbon atoms.

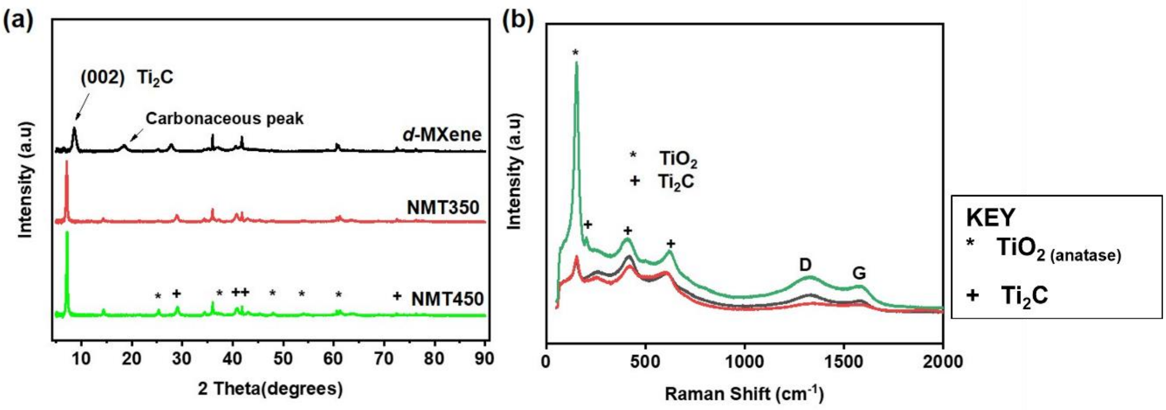

Fig. 6.5(a) XRD patterns and **(b)** Raman spectra of NMT nanocomposites showing phases and vibrational modes respectively

TiO_2 nanoparticles have been produced in situ through a one-step hydrothermal process from MXene and ammonia as a starting precursor. MXenes (containing Ti atoms) is oxidised during the hydrothermal method and form TiO_2 on the edges of the MXene sheets, and the surface defects are produced after the etching process. As the hydrothermal process proceeds, the nucleus of the TiO_2 particles grows due to the diffusion of Ti atoms from the MXene surface. Ti-C bonds are broken during this process, C-C bonds are formed, and an anticipated CO_2 is released during the reaction process as supported by precedence from literature[268]. A combination of all these processes results in the formation of TiO_2 nanoparticles on the surface of N-doped MXene sheets.

Unlike conventional anode material preparation, the NMT nanocomposites were fabricated through aqueous processing into electrodes as a binder-free Li-ion anode material without addition of polymeric binders or conductive agents. In a 1:10 w/v ratio, NMT materials were dispersed in de-ionised water and stirred for 12 hours. The viscous slurries were coated onto Cu foil substrate and dried.

A conventional method, using a two-electrode cell configuration and 1M $LiPF_6$ in EC/DMC (1:1 v/v) electrolyte, was employed for electrochemical characterisation of NMT samples. Cyclic Voltammetry (CV) and Galvanostatic charge- discharge (GCD) measurements were carried out over a voltage range of 0 – 3 V versus Li/Li^+. **Fig. 6.6a and Fig. 6.6b** shows the cyclic voltammogram of NMT350 and NMT450 electrodes respectively at a sweep rate of 0.1 mV s^{-1}.

The CV curves show broad peaks in the range of 1.0 V to 2.0 V occurring during the lithiation and de-lithiation process associated with the reversible intercalation of Li^+ in Ti_2C. During the first cycle, a distict lithiation peak was observed at 0.6 V which disappears on subsequent cycles due to the formation of solid electrolyte interphase (SEI) layer. Also evident in the CV curves is the reversible insertion of lithium in TiO_2 with a coincident peak at 2.0 V indicating oxidation of the TiO_2[85,272].

Through galvanostatic cycling at a current density of 30 mA g^{-1}, the cycling stability of NMT electrodes was assessed (**Fig. 6.6e and 6.6f**). Results show that both NMT350 and NMT450 electrodes offer excellent capacity retention over 50 cycles. NMT350 showed an increase in initial gravimetric capacity of 305 mAh g^{-1} to 339 mAh g^{-1}, while NMT450 showed an increase from an initial gravimetric capacity of 313 mAh g^{-1} to 339 mAh g^{-1}. This trend has previously been reported for TiO_2 and other transition metal-based anodes[223,273]. This increment in capacity can be attributed to the repeated intercalation and de-intercalation of Li^+ in Ti_2C that creates an increase in the interlayer spacing and consequently increases the lithiation capacity of the material[111,274,275]. The efficiency with which charge is transferred in these NMT-based electrode materials was measured. An increment in coulumbic efficiency from an initial value of 40.2 % and 19.4 % to an average of 99.1 % and 99.8 % in NMT350 and NMT450 respectively was observed for the last ten cycles (**Fig. 6.6h**).

The differential capacity (**Fig. 6.6c and 6.6d**) and voltage profiles (**Fig. 6.6e and 6.6f**) of the NMT350 and NMT450 electrodes describes the electrochemical processes occurring for cycles 10, 30, and 50, where the slope of the voltage profiles show that Li^+ is stored over a wide potential range.

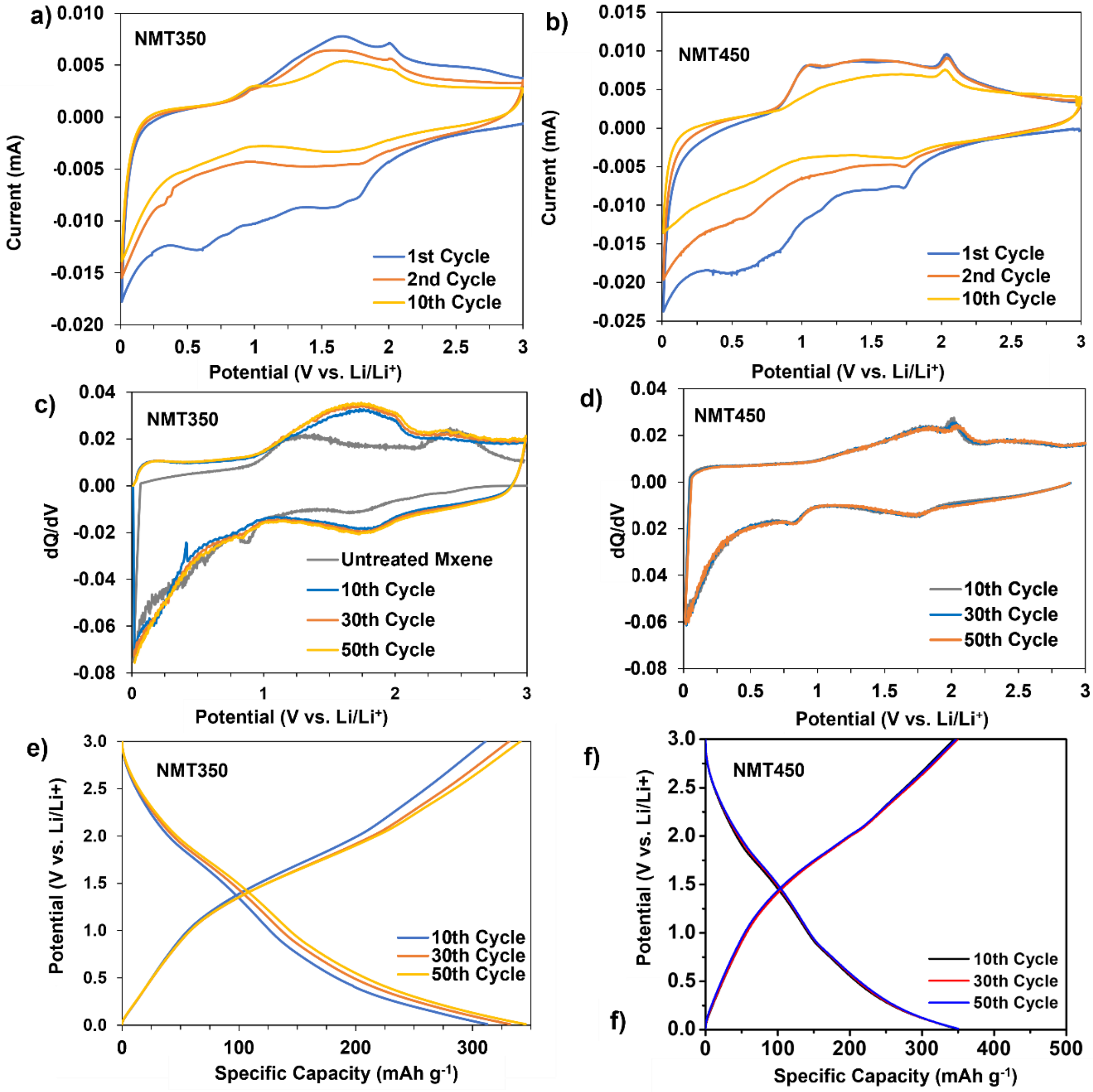

Fig. 6.6(a &b) Cyclic voltammogram of the 1st, 2nd and 10th cycle of NMT half-cell using a sweep rate of 0.1 mV/s in the potential range of 0 – 3 V. **(c & d)** Differential capacity plots of the NMT electrodes derived from the voltage profiles in e & f). **(e & f)** Voltage profiles of the 10th, 30th and 50th cycles of the NMT350 electrode cycled in c & d).

The differential capacity plot for the untreated MXene (**Fig. 6.6d**) showed a less prominent peak between 1.0 V and 2.0 V, indicating the restriction of Li^+ ions to the interlayer spacing due to the absence of TiO_2 that keeps the Ti_2C sheets separated. In contrast, the differential capacity of NMT electrodes (**Fig. 6.6d & 6.6f**) exhibit a dominant and broad peak between 1.0 V and 2.0 V during charge and discharge cycles. This potential region can be associated with the insertion of lithium into anatase TiO_2 and intercalation of Li^+ in Ti_2C.

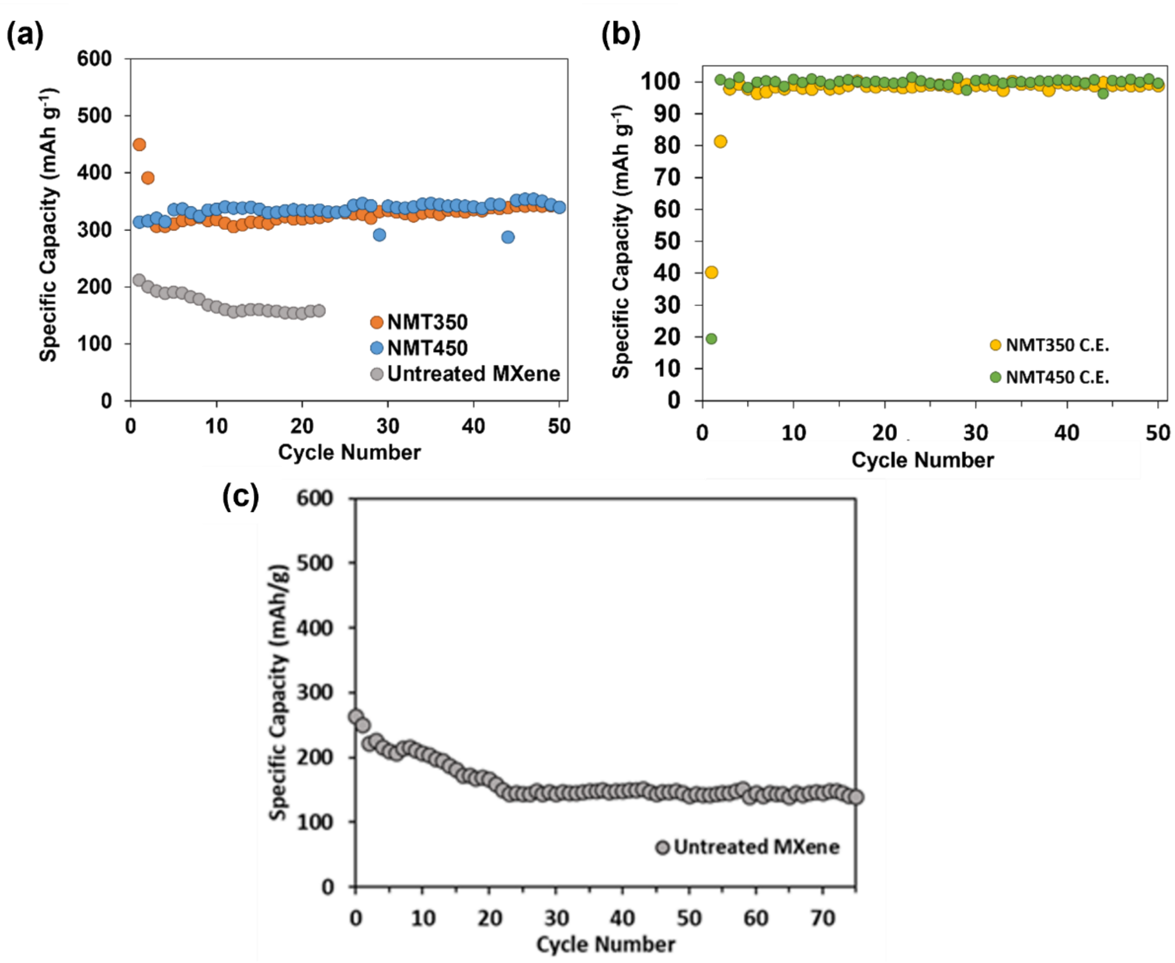

Fig. 6.7 (a) Specific charge and discharge capacities of untreated MXene and NMT electrodes **(h)** coulombic efficiencies of the NMT electrode over 50 cycles using a current density of 30 mA g^{-1} in the potential region of 0 – 3 V. **(i)** Complete specific charge and discharge capacity of untreated MXene electrode over 75 cycles using a current density of 30 mA g^{-1} in the potential region of 0 – 3 V.

GCD measurements were also performed for the untreated MXene precursor material. From this analysis, the electrochemical performance of the NMT electrodes was superior to the untreated MXene precursor material which showed a lower initial capacity of 212 mAh g^{-1} and poorer capacity retention (**Fig. 6.6g**). In contrast to untreated MXene precursor, NMT electrodes showed enhanced gravimetric capacity due to the sandwich arrangement of the nanocomposite, where TiO_2 nanoparticles are embedded between Ti_2C sheets, thereby increasing the accessibility of Li^+ ions through separation of the Ti_2C sheets (**Fig. 6.2**). In addition, TiO_2 also exhibit electrochemical activity and contributes to the capacity of the NMT nanocomposite through reversible insertion and removal of Li^+ ions during charge and discharge cycles.

It is evident from literature that the surface area of MXenes can be enhanced via oxidation or delamination that concurrently creates an increase in its specific capacity[155,226]. As a result, the processing of MXene material via CHFS route enhances the material's specific capacity and capacity retention due to the enhancing properties of TiO_2, compared to untreated delaminated MXene.

6.3.Conclusion

One of the aims of this doctoral study was to synthesise and functionalise 2D MXene through the continuous hydrothermal synthetic route. In this research work, functionalising MXenes via N-doping and growing of TiO_2 nanocrystals has been investigated for energy storage applications. Herein, a controlled single-step hydrothermal synthesis of NMT nanocomposites was developed using aqueous solutions of Ti_2C MXene and ammonia as precursors. Through this method, a means of doping and controlled synthesis of TiO_2 nanoparticles grown on Ti_2C MXene was achieved. The as-synthesised NMT nanomaterials were fabricated into a Li-ion anode material without the use of binders.

The as-synthesised NMT electrodes showed distinct advantages as an electrode material in LIBs, such as improved accessibility of Li^+ ions, increased specific capacity and stable capacity retention, which yield capacitance values (339 mAh g^{-1}) higher than non-delaminated Ti_2C MXenes electrodes, and are more environmentally friendly than conventional graphite-based LIBs.

CHFS shows an environmentally friendly approach in the synthesis of NMT nanocomposites as promising Li-ion anode materials. In addition, through aqueous processing, the electrodes are fabricated, thereby removing the need for toxic solvents in LIBs. From the unique collections of CHFS materials in the development of fast and green hydrothermal technologies, this work adds a significant contribution to the research growth in the energy storage industry.

Chapter 7

Enhanced Electrochemical performance of Hydrothermally Synthesised N-doped TiO_2 -Ti_3C_2 and N-doped TiO_2-Ti_2C MXenes Nanocomposites via Delamination with Cyrene.

7.1. Introduction

One of the fundamental changes in the experimental practices of 2D nanomaterial research is the increasing potential to exfoliate and delaminate single layer nanomaterials from their primary bulk phase material, and the scalability of the process from lab scale to large scale with a high productivity. Exfoliation techniques such as liquid phase exfoliation (LPE) of layered materials have been reported in literature and proven effective in the exfoliation and delamination of layered materials form their bulk counterparts [148–152].

MXenes are derived from their parent bulk MAX phase precursors through chemical exfoliation, intercalation and delamination processes to yield colloidal dispersions of single and few-layered MXenes [48,226,266]. MXenes are hydrophilic; enabling its aqueous processing and show high electrical conductivity and unique morphology. The structure of MXenes also enables the intercalation of various ions and molecules which contributes to its energy storage capacity. MXenes are useful in several applications such as photocatalysis, water desalination, bio sensing and energy storage.

The use of water and bio-based solvents in material engineering offer a friendly material synthesis approach, as they offer similar functionalities compared to their somewhat toxic counterparts. NMP has been reported as a composition in the electrode fabrication of cathode materials[276]. However, NMP's safety and damage to the environment is of concern which has prompted several research into exploring and finding a replacement in the processing of electrode materials. Cyrene could be an alternative intercalant for dipolar aprotic solvents such as NMP and DMF in the MXene delamination process due to its non-toxic and eco-friendly nature. The use of cyrene in electrode fabrication would depend firstly on the solubility of PVDF (a commonly used binder in electrode processing) in cyrene, and if any, a contributing factor of cyrene to easier electrode fabrication, and perhaps enhanced electrode performance. Cyrene has similar properties to NMP and has been studied more recently to explore its green benefit owing to its biodegradability which contributes to a clean environment[156,276,277]. Cyrene has been explored in the processing of 2D materials like graphene, and has been reported to improve the conductivity of graphene inks[278,279].

This chapter reports the structure of cyrene, its properties, and its functionality as an intercalating agent in the delamination of MXenes.

In this research work, exfoliated Ti_3C_2 and Ti_2C MXenes were delaminated using a bio-degradable solvent; cyrene, into single and few-layered MXenes. The cyrene-delaminated MXenes were introduced in separate experiments as precursors to synthesize N-doped MXene-TiO_2 nanocomposites and tested for their electrochemical properties.

7.2. Results and Discussion

7.2.1. Bio-Degradable Solvent-Assisted Delamination of Multi-Layered MXenes.

The morphology and particle analysis of MXCYR were investigated using SEM and TEM respectively. After HF treatment of Ti_2AlC **(Fig. 7.1a)**, the resulting material was exfoliated MXene as seen in **Fig. 7.1b** which is similar to what has been reported in literature[155], where MXene showed an accordion-like morphology as compared to the starting Ti_2AlC material. The addition of cyrene to the exfoliated MXene while concurrently sonicating the mixture resulted in the delamination of MXene layers into few layered and single 2D MXene sheets (**Fig. 7.1c-f**). This is due to the weakening of the Van der Waals forces between the MXene layers through sonication and intercalation, resulting to separation of sheets.

The SEM image in **Fig. 7.1(c)** showed that cyrene successfully delaminated multi-layered MXenes into few-layered and single MXene sheets via sonication. Initially, SEM analysis from preliminary work 1 where probe (**Fig. 7.1d**) and bath (**Fig. 7.1e**) sonication methods were used showed that both methods were successful in obtaining delaminated sheets of MXenes. However, some multi-layered MXenes were observed in both techniques, with more defects present in probe-sonicated MXenes. This prompted an optimisation of the synthetic strategies used in preliminary work 1 by increasing the sonication time to 2 h and 20 h for probe and bath respectively, and volume of cyrene solvent used to 40 ml and 60 ml in both sonication methods. **Figures 7.2a and 7.2b** are SEM images of MXene samples sonicated using a probe with 40 ml and 60 ml of cyrene respectively, and figures **7.2c** and **7.2d** are bath-sonicated MXene samples with 40 ml and 60 ml of cyrene respectively. As observed from these SEM images (**Fig. 7.2a-d**), an increase in the volume of cyrene showed improved delamination of MXene sheets in both probe (**Fig. 7.2b**) and bath (**Fig. 7.2d**) sonication methods, as more single MXene sheets are observed. Similar to observations in preliminary work 1, prolonged sonication time also contributed to improved delamination, and produce MXenes with more defects and smaller flake sizes.

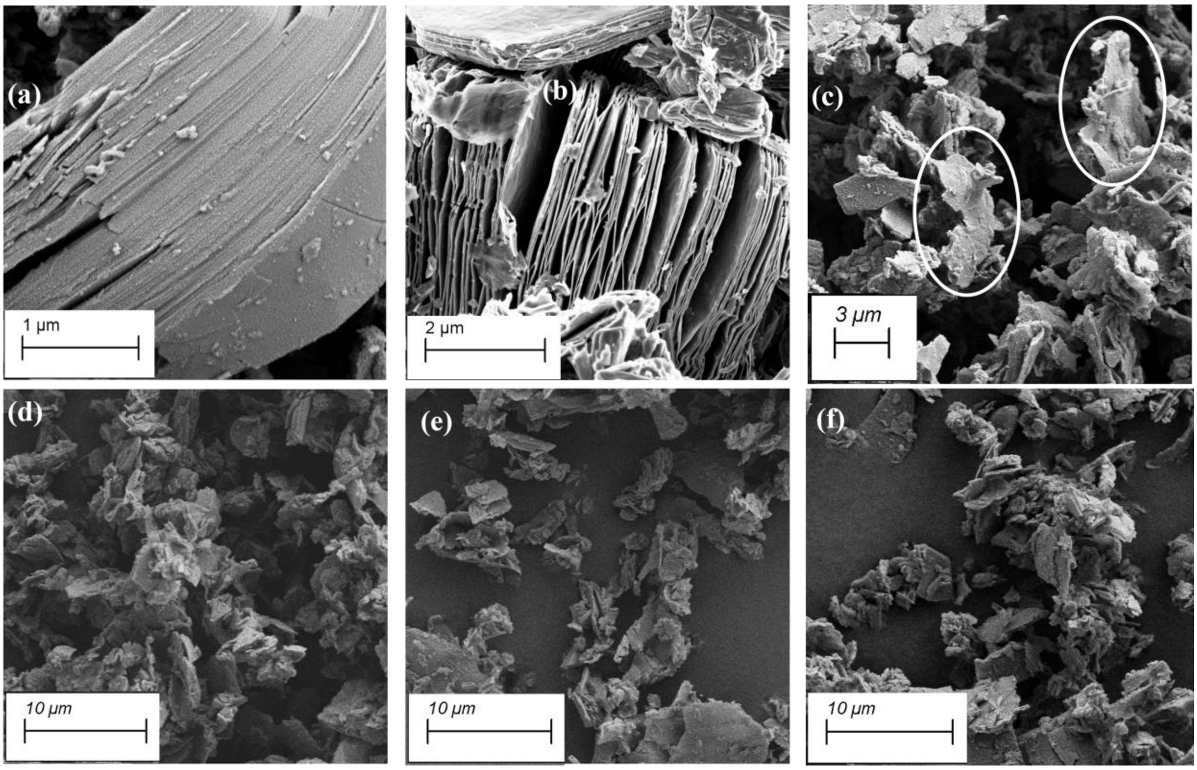

Fig. 7.1 SEM of **(a)** Start-up MAX phase material, **(b)** Accordion-like structure of exfoliated Ti_2C MXene, **(c)** MXCYR showing successful delamination into single few-layered sheets, **(d)** MXCYR delaminated sample via Probe sonication for 30 min, **(e)** MXCYR delaminated sample via bath sonication for 1 h, and **(f)** MXCYR delaminated sample via bath sonication for 3.5 h

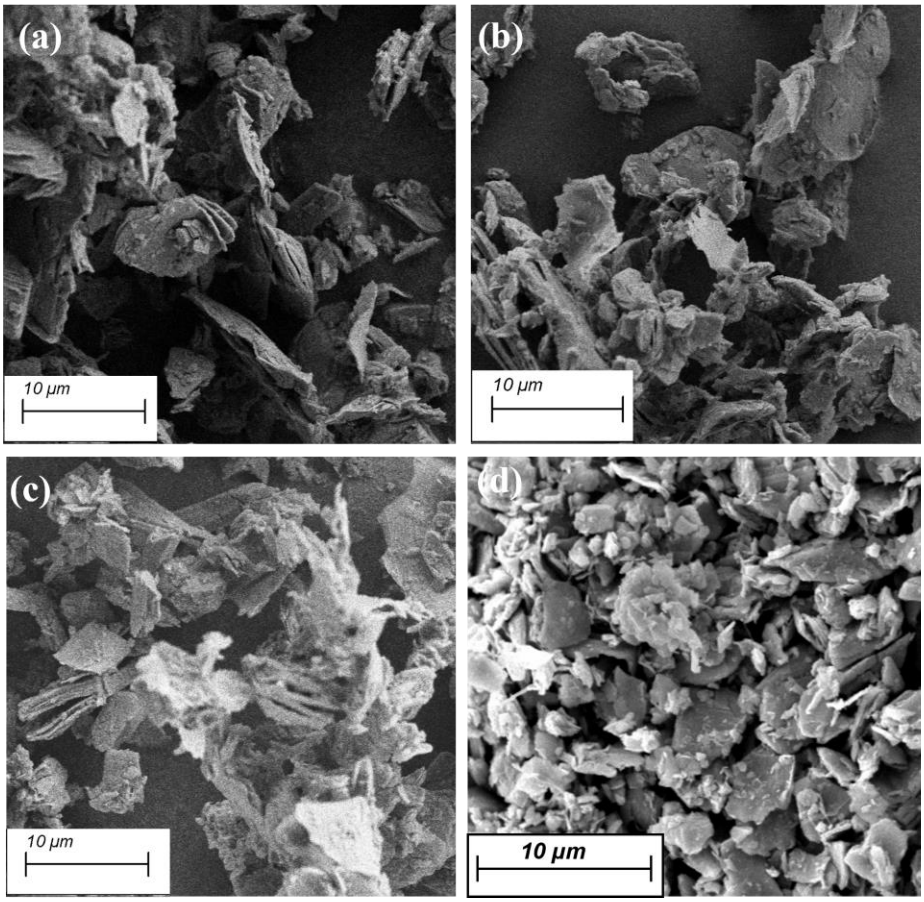

Fig. 7.2 SEM of **(a)** MXCYR sonicated by probe for 2 h in 40 ml cyrene solvent, **(b)** MXCYR sonicated by probe for 2 h in 60 ml cyrene solvent, **(c)** MXCYR sonicated by bath for 24 h in 40 ml cyrene solvent, and **(d)** MXCYR sonicated by bath for 24 h in 60 ml cyrene solvent

The TEM micrographs of MXCYR showed the presence of single and stacked sheets of MXene (**Fig. 7.3a**) after delamination with cyrene. Surface defects **(Fig. 7.3b**) of nanometre sizes were also observed after the delamination process. These defects can be attributed to both concentration of HF acid after etching, and prolonged sonication time of MXene. Surface defects can be advantageous in providing sites for intercalation of ions in MXene which increases the storage capacity, but can also be detrimental by limiting achievable voltage window through electrolyte decomposition[280]. These defects have been reported in functionalised graphene and some MXenes, and can act as nucleation sites for metal oxides in MXene nanocomposites[281,282]. TiO_2 nanoparticles were observed to be randomly distributed across the surface of MXene sheets (**Fig. 7.3c**), attributed to fast oxidation of MXene on exposure to air.

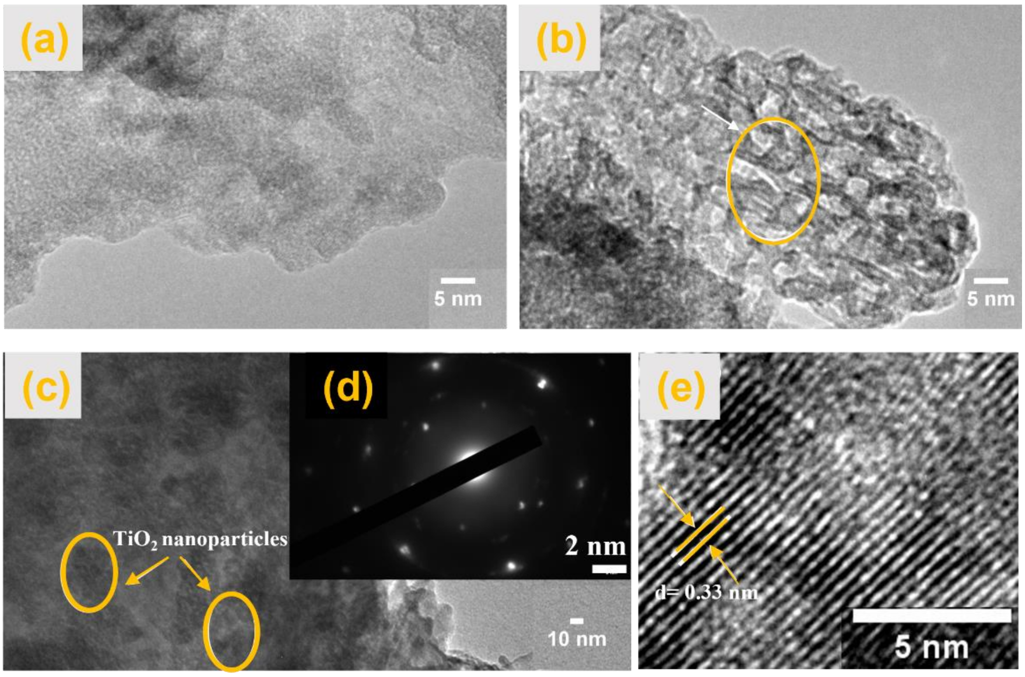

Fig. 7.3 TEM of MXCYR showing **(a)** single and stacked MXene sheets **(b)** MXene sheets with defects marked with arrows **(c)** TiO_2 nanoparticles **(d)** SAED diffraction pattern of MXene sheet **(c)** lattice fringe of Ti_2C MXene

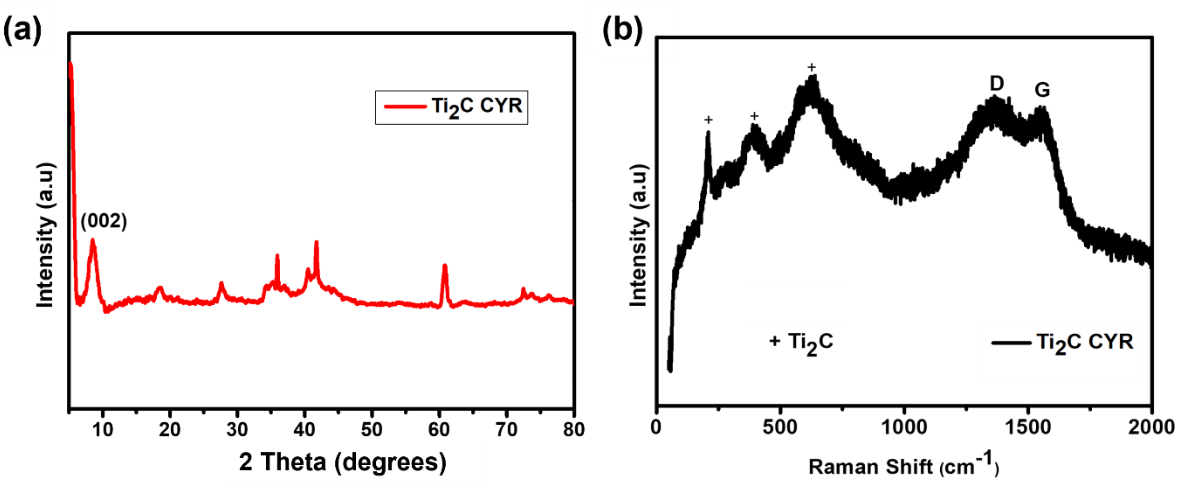

Fig. 7.4 (a) XRD pattern showing crystallinity and (b) Raman spectra with D and G bands of Cyrene-delaminated Ti_2C MXene

The as-synthesised MXCYR material was also confirmed to retain its hexagonal $P6_3/mmc$ structure as seen in the acquired SAED pattern of MXene sheets **(Fig.7.3d)**. This shows that there is no degradation in structure after the cyrene delamination process.

The high-resolution TEM (HRTEM) micrographs also showed the lattice fringe spacing of MXene crystal (**Fig. 7.3e**), where a 0.33 nm d-spacing was measured and corresponds to the lattice of Ti_2C MXenes. This measured value corresponds to that reported in the literature of Ti_2C MXene[262].

XRD pattern of as-prepared for Ti_2CCYR MXene is shown in **Fig. 7.4**, where a shift in the (002) peak of starting un-delaminated MXene is observed downward and broadened. These downward shift in diffraction positions have been previously attributed to intercalation of solvents during the delamination process [283] . Herein, the sharp (002) diffraction peak for un-delaminated MXene at $2\theta = 9.8°$ prior to delamination and shifted downward to 8.95° after delamination process. This confirms a successful delamination of Ti_2C MXenes with a biodegradable solvent (cyrene), and it agrees with the observed SEM and TEM images of single and few-layered Ti_2C MXene sheets. It is also notable that there is no presence of (101) diffraction peak of TiO_2 in the MXCYR sample that could have been attributed to the oxidation of MXenes in cyrene, despite being immersed in cyrene solvent for 20 hours.

Raman spectra in **Fig. 7.4b** described the vibrational modes of Ti_2C MXene where peaks centred at 249 cm^{-1}, 410 cm^{-1} and 612 cm^{-1} are observed and identified as vibrations from Ti_2C. The absence of a peak at 149 cm^{-1} indicates no presence of anatase TiO_2 in the sample from oxidation. Similarly, to XRD analysis, Raman also confirmed no oxidative effect from cyrene assisted delamination on Ti_2C MXenes.

From the above SEM, TEM, XRD and Raman analysis, it confirms the successful delamination of Ti_2C MXenes with cyrene. As a result, the same experimental procedure was extended to Ti_3C_2 MXenes and tested for electrochemical performance

After the successful delamination of Ti_2C MXene with cyrene, etched Ti_3C_2 MXenes were delaminated using similar method to further delaminate multi-layered Ti_3C_2 MXenes into single and few layered MXene sheets. **Fig. 7.5** below shows the SEM image of cyrene delaminated Ti_3C_2 MXene upon treatment with cyrene, where a typical accordion-like morphology is observed and compose of single and few layered Ti_3C_2 sheets. This confirms the successful delamination of MXene with cyrene.

The crystallinity and chemical structure analysis of the delaminated Ti_3C_2 were investigated by XRD and Raman spectroscopy respectively **(Fig. 7.9)**.

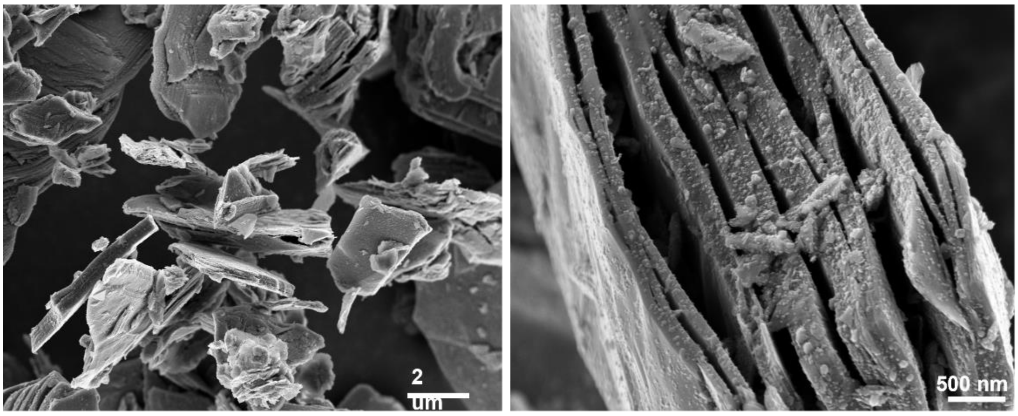

Fig. 7.5 SEM of cyrene-delaminated Ti_3C_2 showing single and multi-layered Ti_3C_2 sheets

With a two-electrode cell configuration, the electrochemical performance of cyrene-delaminated Ti_2C and Ti_3C_2 MXenes were investigated over a potential range of 0 – 3 V versus Li/Li^+. **Fig. 7.6 and Fig. 7.7** show the CV and GCD plots of Ti_2CCYR and Ti_3C_2CYR respectively, where a specific capacitance value of 538 F g^{-1} at 0.1 mV s^{-1} was measured for Ti_2CYR in the first cycle and reduced to 302 F g^{-1} after 5 cycles. This specific capacitance value exceeds that of DMSO delaminated Ti_2C MXenes previously reported in literature [192]. This increment can be attributed to the increase in interlayer spacing of Ti_2C MXene after delamination with cyrene. On the other hand, Ti_3C_2CYR CV profile showed a specific capacitance value of 967 F g^{-1} at 0.1 mV s^{-1} and reduced to 625 F g^{-1} over 5 cycles **(Fig. 7.7)**. Despite reports in literature on the blockage of pores by cyrene[277], which limits the accessible surface area, this improvement in the electrochemical performance of cyrene-delaminated MXenes show otherwise. Such improvement is attributed to the increase in the interlayer spacing between MXene sheets through cyrene introduction between MXene layers. In addition, an improvement in charge transfer also contributed to the increase in electrochemical performance. The enhancement of charge transfer kinetics results from the improved conductivity from cyrene processing of MXenes **(Fig. S3)**. This observation has been reported in the processing of 2D graphene inks[279].

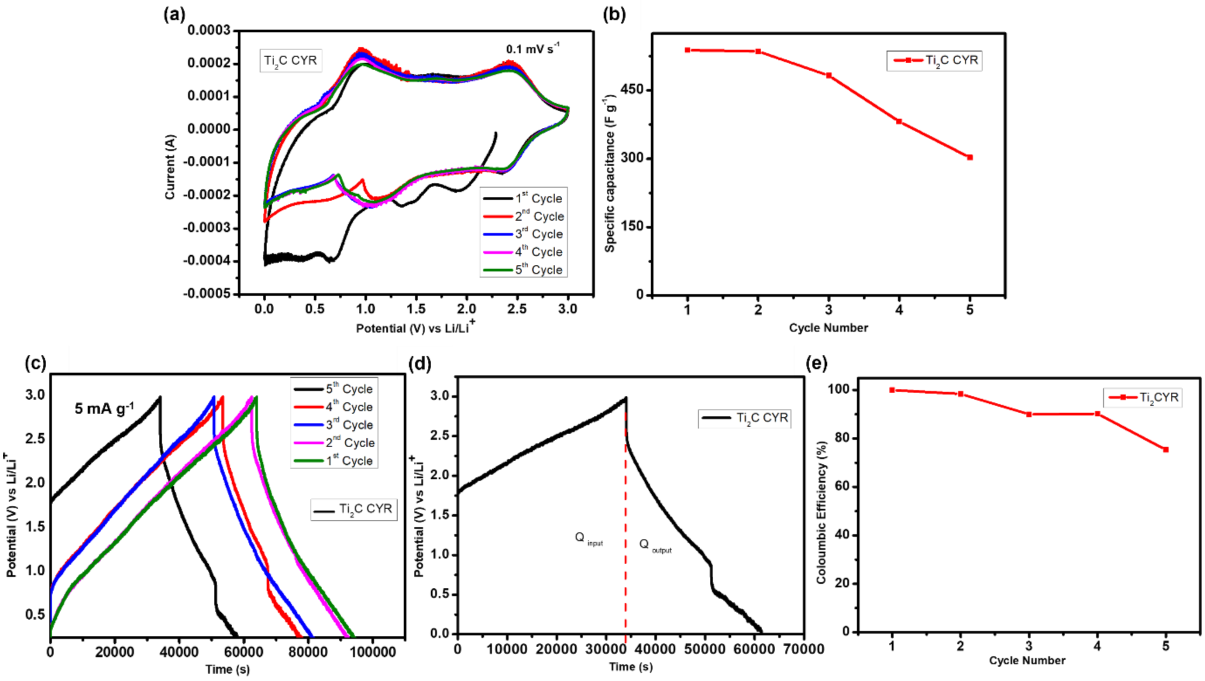

Fig. 7.6 (a) CV profile at 0.1 mV s^{-1} **(b)** Capacitance retention **(c)** GCD plot **(d)** Coulombic efficiency evaluation and **(e)** Coulombic efficiency plot of Ti_2CYR over 5 cycles

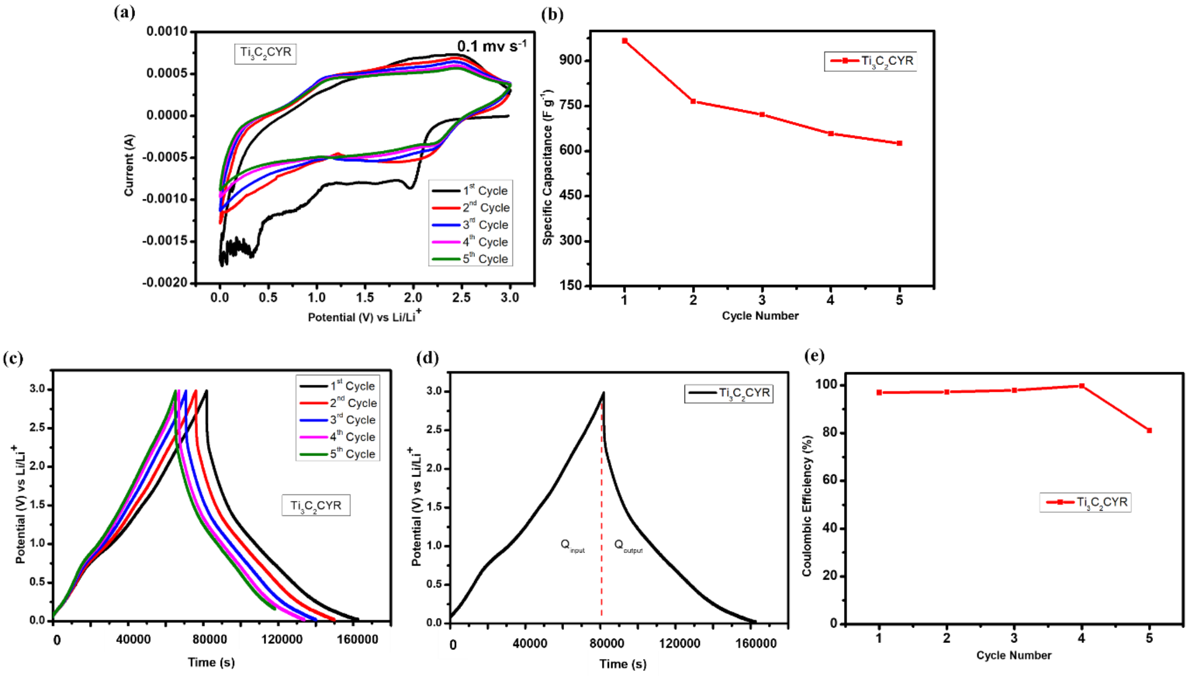

Fig. 7.7 (a) CV profile at 0.1 mV s^{-1} and **(b)** Capacitance retention **(c)** GCD plot **(d)** Coulombic efficiency evaluation and **(e)** Coulombic efficiency plot of Ti_3C_2CYR over 5 cycles

7.2.2. CHFS of NMT nanocomposites using cyrene -delaminated Ti_3C_2 MXenes

Using the HF- assisted MAX phase exfoliation technique described by Gogotsi and co-workers[18], Ti_3C_2 and Ti_2C MXenes were synthesised and further delaminated into single and few-layered MXenes with cyrene as the delaminating agent. Upon electrochemical analysis of both cyrene-delaminated MXenes (Ti_2CCYR and Ti_3C_2CYR), Ti_3C_2CYR showed a better electrochemical performance (967 F g^{-1}) which made it the choice of starting precursor for the preparation of N-doped MXene-TiO_2 nanocomposites.

Ti3C_2CYR MXenes were dispersed in de-ionised water and pumped into the CHFS reactor as a precursor, along with ammonia as a doping agent at a temperature of 350 °C and pressure of 24.8 MPa to synthesise N-doped MXenes decorated with TiO_2 nanoparticles. Through CHFS, MXene is hydrothermally oxidised in a controlled manner to form TiO_2 nanoparticles on its edges and sheet surfaces. During the hydrothermal process, the Ti-C bonds are broken, Ti-O, Ti-N and C-C bonds are formed to produce N-doped MXene TiO_2 nanocomposites.

The as-synthesised nanocomposites were characterised for different analyses, and further formulated into electrodes for electrochemical analysis.

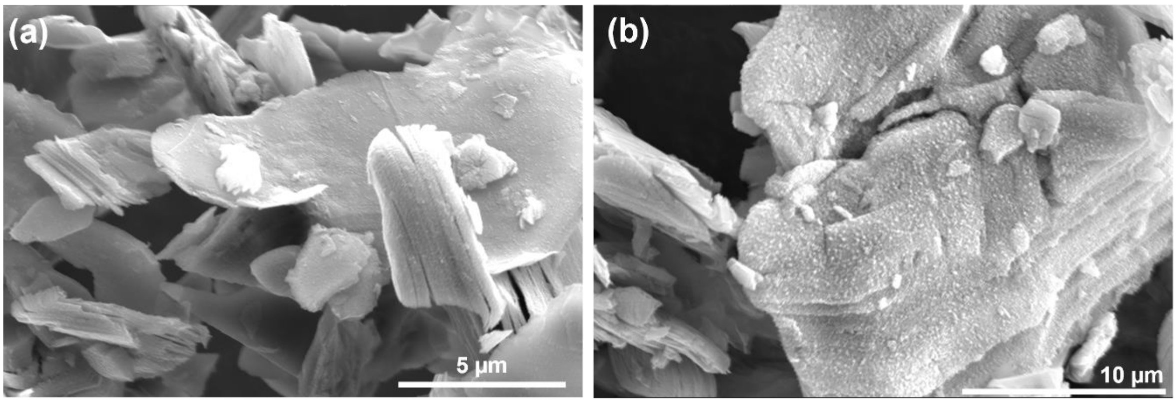

Fig. 7.8 SEM images of (a) N-Ti_3C_2 and (b) N-Ti_2C MXenes

The scanning electron microscopy (SEM) images **(Fig. 7.8)** show the hydrothermal effect on MXenes through the formation of spherical particles on the edges and surfaces of MXene sheets. Therein, both nanocomposites (N-Ti_3C_2-TiO_2 and N-Ti_2C-TiO_2) showed the typical accordion-like structure of separated MXene sheets with spherical particles randomly distributed on the edges and across the surface of the MXene sheets. At this near-supercritical environment created in the CHFS reactor, TiO_2 is hydrothermally formed from a controlled MXene oxidation through adjusting the reaction temperature, pressure and flow rate of the precursors. The nanocomposites also showed a sandwich-like arrangement of TiO_2

nanoparticles embedded between MXene sheets, which is in agreement with previously reported data[192]. This sandwich arrangement has been reported to keep the MXene sheets separated to facilitate intercalation of Li^+ ions and access to electrolyte ions.

Fig. 7.9a show the diffraction peaks of the starting precursor (cyrene delaminated Ti_3C_2 T) prior to CHFS process and N-doped MXenes-TiO_2 nanocomposites after CHFS process (N-Ti_3C_2 TiO_2). It can be observed that the (002) peak of N-Ti_3C_2-TiO_2 shifted towards lower angles compared to that of the starting precursor. This diffraction peak shift confirms the further expansion of the interlayer spacing of MXene which further delaminates MXenes into single and few-layered sheets through intercalation with hydrothermally grown TiO_2 on the surface of MXene sheets. This observation has been reported in the literature of MXenes [226,284]. The XRD spectra also show the presence of a peak at $2\theta = 25°$ that corresponds to the (101) plane of anatase TiO_2 (JCPDS card no. 00-021-1272)[192,268]. However, this diffraction peak is not prominent in the nanocomposites when compared to the (002) diffraction peaks of MXene, making MXene the dominant phase in the nanocomposites. Another distinctive observed in the XRD spectra after CHFS is the carbonaceous peak at $2\theta = 14$ ° resulting from the formation of C-C bonds during the hydrothermal process. This observation is in agreement with reported literature on hydrothermally treated MXenes[192].

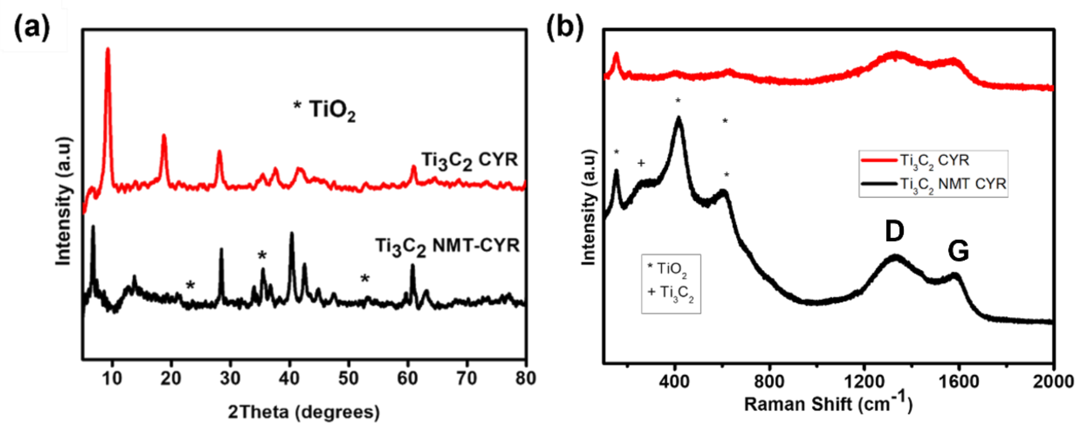

Fig. 7.9 (a) XRD showing the phase composition and **(b)** Raman spectrum of N-Ti_3C_2 and N-Ti_3C_2 MXenes

The typical features in the Raman spectrum of as-synthesised N-MXenes were the vibrational modes of Ti_3C_2 and TiO_2 which are consistent with those reported in literature **(Fig. 7.9b)**. Therein, the as-prepared N-Ti_3C_2 MXene showed typical Raman bands of Ti_3C_2 MXene with D and G bands at 1328 and 1564 cm^{-1} representing graphitic carbon due to the conductive carbide which provides enhanced electrochemical properties by fast charge transfer between carbide layers[285]. In addition, bands of TiO_2 are observed at 144, 394 and 621 cm^{-1} which corresponds to $E_{g(1)}$, B_{1g} and $E_{g(3)}$ vibrational modes of Ti-O bonds respectively[286,287]. The increment in I_D/I_G ratio of $NTi_3C_2TiO_2CYR$ showed presence of structural defects and highly disordered amorphous carbon in the sample which could have been formed during the growth of TiO_2 on the surface of Ti_3C_2 MXene sheets.

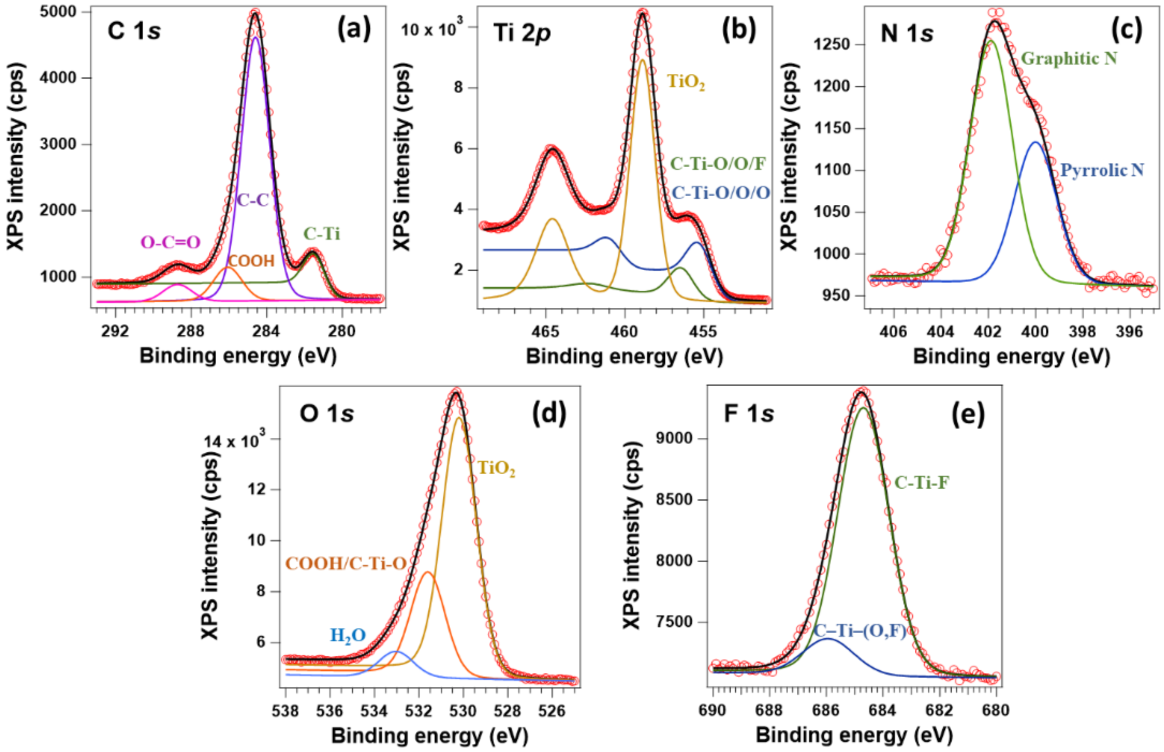

Fig. 7.10 (a) XPS Scan of F(1s), O(1s), Ti(2p) and C(1s) core levels showing the chemical bonding states in NTi_3C_2CYR (XPS data measured and fittings done by Dana Popescu, National Institute of Materials Physics, Magurele -Romania).

XPS analysis of $NTi_3C_2TiO_2CYR$ was conducted to determine its chemical composition and valence states. XPS scan **(Fig. 7.10)** showed the presence of Ti, C, N, O and F in the sample at 22.23%, 32.25%, 3.94%, 36.92% and 4.66% respectively. High-resolution N 1*s* spectrum of Ti_3C_2 NMT-CYR shown in **Fig. 11(c)** was deconvoluted into two peaks at 400.0 eV and 401.9 eV binding energies. The components correspond to pyrrolic nitrogen and graphitic N, respectively[192,288]. The O1s spectra showed three deconvoluted peaks at 530.2, 531.6 and 533.0 eV attributed to C-Ti-O_x, O-Ti-O and C-Ti-OH 1s cores respectively[289]. The Ti 2p peaks were deconvoluted into six main peaks of Ti2$p_{3/2}$ and Ti2$p_{1/2}$ at (455.3, 461.0), (456.6, 462.5) and (458.7, 465) eV, associated with Ti-C, Ti^{2+}, and Ti^{4+} respectively. The Ti_{2p}

associated with +4 oxidation state indicates the presence of TiO_2 in the nanocomposite. Four peaks were fitted from C 1s core associated with C-Ti, C-Ti-O, C-C, and C-O at 281.5, 284.0, 286.2, and 288.5 eV respectively. All fitted peaks are comparable to existing literature[192,288,289].

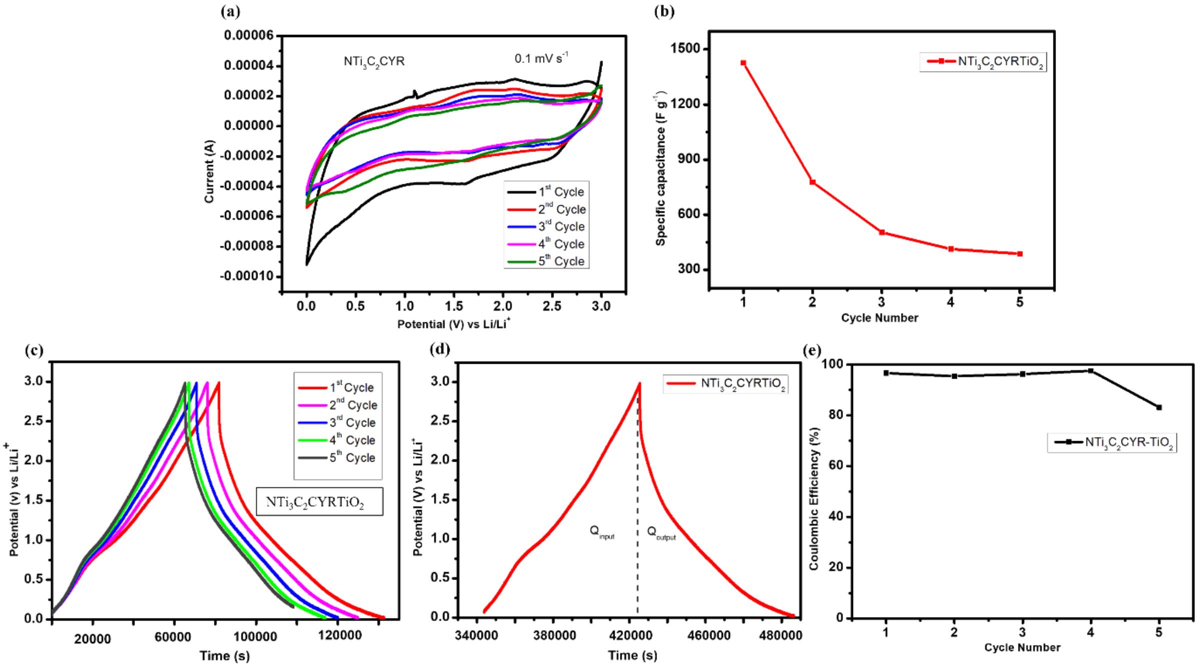

Fig. 7.11(a) CV profile and **(b)** Capacitance retention of $NTi_3C_2CYRTiO_2$ **(c)** GCD plots **(d)** Coulombic efficiency estimation **(e)** Coulombic efficiency plot of $NTi_3C_2CYRTiO_2$ over 5 cycles.

Fig. 7.11a showed the CV curves of $NTi_3C_2CYRTiO_2$ electrode at a scan rate of 0.1 mVs^{-1} for 5 cycles. The MXene nanocomposite is observed to experience a pseudocapacitive behaviour owing to its nearly-rectangular shaped CV, where lithiation and de-lithiation processes in the electrode material are occurring, coupled with surface redox reactions between 1 – 3 V owing to lithium intercalation into TiO_2 and NTi_3C_2 sheets. During the first cycle, an irreversible peak between 0 and 0.52 V occurred due to the formation of SEI, owing to electrolyte decomposition or unwanted reactions between the electrode and electrolyte. This peak was no longer visible on subsequent cycles owing to already formed SEI layer. The peaks at 1.76 V can be attributed to the redox reaction of Ti^{3+}/Ti^{4+} in TiO_2 [285]. Lithiation and de-lithiation peaks in $NTi_3C_2CYRTiO_2$ were also observed between 2.1 and 2.5 V, which agrees with reported literature[111,192,268].

The NTi_3C_2CYR MXene electrode delivered a specific capacitance of 1426 F g^{-1} at 0.1 mV s^{-1} **(Fig. 7.11b)**. The GCD curves **(Fig. 7.11c)** show a slightly linear potential vs. time plot with no plateau, indicating presence of pseudocapacitive storage mechanism owing to surface redox reactions, with a coulombic efficiency of 95% at initial cycling **(Fig. 7.10e)**. However, after 5 cycles of charge and discharge, it showed a poor capacity retention as its capacity reduced to 387 F g-^{1} with a coulombic efficiency of 83%. This low capacitance values could be attributed to the aggregation of TiO_2 nanoparticles which limits lithiation and delithiation processes by limiting access to electrochemically active sites. These aggregated TiO_2 nanoparticles also limits their function as a Li^+ host as compared to well dispersed TiO_2 nanoparticles[285].

7.3. Conclusion

Delaminated MXenes were successfully prepared by the ultrasonication of multi-layered MXenes in cyrene, as an alternative delaminating agent to DMSO. Through a continuous hydrothermal flow process, Ti_3C_2 -TiO_2 nanocomposites were synthesised from the cyrene-delaminated MXenes and nitrogen-doped in-situ using water soluble precursors. The cyrene-delaminated N-doped 2D MXene nanocomposites showed capacitive electrochemical behaviour with a specific capacitance of 387 F g^{-1} and coulombic efficiency of 83% after 5 cycles. This work provides background knowledge into developing cyrene-based MXenes as an environmentally friendly approach in synthesising single and few-layered MXenes that can be modified into composites for enhanced electrochemical properties. The improved capacitance value when compared to the starting precursor (Ti_3C_2CYR) could be attributed to enhanced Li^+ access to the interlayer spacing between 2D MXene sheets owing to expansion of the interlayer distance between MXene sheets which shortened the ion diffusion path, and increased accessibility to electrolyte ions.

Chapter 8

Future direction

2D materials hold a promising future in the engineering of energy storage materials for high energy and power applications. These materials exhibit exciting properties owing to their quantum confinement, and can be researched extensively through functionalisation and enhancement of material into nanocomposites for superior performance. Herein, 2D materials have been explored in energy storage applications with results showing room for improvement in the synthetic methodologies explored. Through CHFS, several nanomaterials and nanocomposites were successfully prepared and functionalised insitu within fraction of a second, saving reasonable time and promoting aqueous processing which limits the use of some toxic solvents that has caused environmental concerns.

The future direction of this research work will involve exploring the influence of mass loading of MnO_2 on rGO sheets. This would involve conducting electrochemical impedance spectroscopy (EIS) studies to understand the influence of MnO_2 on the resistive properties of the nanocomposite as the mass loading of MnO_2 increases. The EIS study will provide a Nyquist plot that describes the solution and bulk resistance of the MnO_2-rGO electrode. Also, another area that probes an investigation would be the choice of electrolyte used as many reported literatures focused more on aqueous based electrolytes which provides a different chemistry of electrochemical reactions. As such, aqueous solutions such as 6M KOH, 1M $LiNO_3$ and 1M Na_2SO_4 can be explored as electrolytes to analyse the electrochemical performance of the as-synthesised MnO_2-rGO nanocomposites. A smaller potential range could be implored in future electrochemical tests as MnO_2-rGO could be storing more and undergo a reversible lithiation and de-lithiation process over a narrow potential window. This is also evident in literature studies as most potential range are between 0 and 1 V. It would also be a good recommendation to improve electrode fabrication process in terms of enhancing the nanocomposite with more conductive carbon black due to low conductivity of MnO_2, which simultaneously improve charge transfer and reduce the weight percentage of the active material. Furthermore, annealing MnO_2-rGO nanocomposites is recommended to improve its physio-chemical and structural properties for use as an electrode material for lithium-ion batteries[290]. Also, exploring other morphological variation of MnO_2 could be beneficial in improving the electrochemical performance of the nanocomposite as MnO_2 with a sheet-like structure has been reported in literature to show improved electrochemical properties due to its larger surface area and more chemical active sites[291]. On the quest of green methodology in producing nanomaterials, CHFS as an advantageous methodology in morphology control and variation of nanomaterials can be employed to produce sheet-like MnO_2 and explore its electrochemical properties. MnO_2 should be combined with green carbon-based materials to produce environmentally friendly composites for use as light-weight electrode materials.

Also, using CHFS an advantage, it would be ideal to explore different morphological variation of TiO_2 and rGO which may offer more electrochemically active sites for charge storage. Furthermore, TiO_2-rGO can be combined with other carbonaceous such as CQDs to offer its high surface area and fast electron transfer kinetics towards improving its electrochemical performance.

The results in this research work showed an absence of TiO_2 diffraction peaks in the XRD pattern of MXCYR. This probes an investigation of the antioxidative effect of cyrene on MXenes. Due to the susceptibility of MXenes to oxidation when exposed to air or aqueous medium, this future study will provide more information on the activities of the different types of MXenes in cyrene, the use of cyrene as a non-toxic antioxidizing delaminant, and processing of MXenes in cyrene as a preferred dispersing medium. Also, incorporating silicon nanostructures into as-synthesised NMT nanocomposites would be highly recommended. Silicon is being extensively researched as a promising electrode material for LIBs owing to its higher theoretical capacity when compared to commercially used carbon-based electrode, and NMT nanocomposites would provide improved structure to overcome the stability of Si during lithiation process. Through my proposed methodology; CHFS, silicon can be introduced into NMT nanocomposites and simultaneously doped in-situ to improve its conductivity, hence enhancing the storage capacity of Li^+ ions. Based on this research work outcome, further optimisation of the delamination route for *m*-MXene is recommended to produce better delaminated MXenes with single or few-layered sheets, which creates more accessible surface area for electrolyte ions and concurrently, Li-ion storage.

This work novelty extends into exploring cyrene in the delamination of hydrothermally synthesised N-doped MXenes- TiO_2 nanocomposites. Following a good electrochemical analysis of NTi3C2CYR nanocomposites, it would be recommended to run the as-synthesised nanocomposite for longer cycles (>1000) and evaluate its electrochemical performance. Similarly, it would be ideal to perform a rate capability test on as-synthesised nanocomposites at increasing scan rates to study the capacitive behaviour and determine the dominant charge storage mechanism in the nanocomposite. This can also be done on GCD at different charge-discharge densities to evaluate the stability of as-synthesised nanocomposites over multiple cycles (>1000). Exploring the performance of the as-synthesised nanocomposites in various electrolytes (e.g., 1M Na_2SO_4, 1M $LiNO_3$, 0.5M H_2SO_4, 6M KOH etc.) will provide means of optimising the electrochemical performance of N-doped cyrene delaminated MXenes for use in metal-ion batteries. Furthermore, electrochemical impedance spectroscopy tests should be carried out on as-synthesised materials prior to running CV and GCD tests to understand the electrical resistance (impedance) of the electrode/electrolyte interface and estimate the capacitance of the nanomaterial.

Lastly, it will be advantageous to explore the different morphologies of MXenes (scrolls, plates, crumpled sheets, spheres)[262], and combine as a nanocomposite with morphologically enhanced TiO_2 (such as tubular, sheets)[292] as a means to (i) probe the effect of morphology on the electrochemical properties of MXene, and (ii) to potentially optimise the electrochemical performance of MXene-TiO_2 nanocomposites owing to the high electrochemical performance of tubular TiO_2.

References

[1] J.-M. Tarascon, M. Armand, Issues and challenges facing rechargeable lithium batteries, Nat. 2001 4146861. 414 (2001) 359–367. https://doi.org/10.1038/35104644.

[2] Jack Loughran, Bad news for batteries: cobalt and lithium supplies ‘critical’ by 2050, (n.d.). https://eandt.theiet.org/content/articles/2018/03/bad-news-for-batteries-cobalt-and-lithium-supplies-critical-by-2050/ (accessed April 4, 2019).

[3] R. Huggins, Energy storage, 2010. https://link.springer.com/content/pdf/10.1007/978-3-319-21239-5.pdf (accessed November 30, 2021).

[4] N. Kularatna, Energy Storage Devices for Electronic Systems: Rechargeable Batteries and Supercapacitors, 2014. https://doi.org/10.1016/C2012-0-06356-9.

[5] M. Endo, T. Maeda, T. Takeda, Y.J. Kim, K. Koshiba, H. Hara, M.S. Dresselhaus, Capacitance and Pore-Size Distribution in Aqueous and Nonaqueous Electrolytes Using Various Activated Carbon Electrodes, J. Electrochem. Soc. 148 (2001) A910. https://doi.org/10.1149/1.1382589/XML.

[6] J. Billaud, F. Bouville, T. Magrini, C. Villevieille, A.R. Studart, Magnetically aligned graphite electrodes for high-rate performance Li-ion batteries, Nat. Energy 2016 18. 1 (2016) 1–6. https://doi.org/10.1038/nenergy.2016.97.

[7] B.J. Landi, M.J. Ganter, C.D. Cress, R.A. DiLeo, R.P. Raffaelle, Carbon nanotubes for lithium ion batteries, Energy Environ. Sci. 2 (2009) 638–654. https://doi.org/10.1039/B904116H.

[8] R. Heimböckel, F. Hoffmann, M. Fröba, Insights into the influence of the pore size and surface area of activated carbons on the energy storage of electric double layer capacitors with a new potentially universally applicable capacitor model, Phys. Chem. Chem. Phys. 21 (2019) 3122–3133. https://doi.org/10.1039/C8CP06443A.

[9] J. Jiang, Y. Li, J. Liu, X. Huang, C. Yuan, X.W. Lou, Recent Advances in Metal Oxide-based Electrode Architecture Design for Electrochemical Energy Storage, Adv. Mater. 24 (2012) 5166–5180. https://doi.org/10.1002/ADMA.201202146.

[10] Q. Zhu, Y. Song, X. Zhu, X. Wang, Ionic liquid-based electrolytes for capacitor

applications, J. Electroanal. Chem. 601 (2007) 229–236. https://doi.org/10.1016/J.JELECHEM.2006.11.016.

[11] B.P. Tripathi, V.K. Shahi, Organic–inorganic nanocomposite polymer electrolyte membranes for fuel cell applications, Prog. Polym. Sci. 36 (2011) 945–979. https://doi.org/10.1016/J.PROGPOLYMSCI.2010.12.005.

[12] U. Alli, S.J. Hettiarachchi, S. Kellici, Chemical Functionalisation of 2D Materials by Batch and Continuous Hydrothermal Flow Synthesis, Chem. - A Eur. J. (2020) 6447–6460. https://doi.org/10.1002/chem.202000383.

[13] C. Tan, X. Cao, X.J. Wu, Q. He, J. Yang, X. Zhang, J. Chen, W. Zhao, S. Han, G.H. Nam, M. Sindoro, H. Zhang, Recent Advances in Ultrathin Two-Dimensional Nanomaterials, Chem. Rev. 117 (2017) 6225–6331. https://doi.org/10.1021/acs.chemrev.6b00558.

[14] D. Deng, K.S. Novoselov, Q. Fu, N. Zheng, Z. Tian, X. Bao, Catalysis with two-dimensional materials and their heterostructures, Nat. Nanotechnol. (2016). https://doi.org/10.1038/nnano.2015.340.

[15] Z.J. Fan, J. Yan, T. Wei, G.Q. Ning, L.J. Zhi, J.C. Liu, D.X. Cao, G.L. Wang, F. Wei, Nanographene-Constructed Carbon Nanofibers Grown on Graphene Sheets by Chemical Vapor Deposition: High-Performance Anode Materials for Lithium Ion Batteries, ACS Nano. 5 (2011) 2787–2794. https://doi.org/10.1021/NN200195K.

[16] Y. Gogotsi, B. Anasori, The Rise of MXenes, ACS Nano. 13 (2019) 8491–8494. https://doi.org/10.1021/ACSNANO.9B06394.

[17] K.I. Bolotin, K.J. Sikes, Z. Jiang, M. Klima, G. Fudenberg, J. Hone, P. Kim, H.L. Stormer, Ultrahigh electron mobility in suspended graphene, Solid State Commun. 146 (2008) 351–355. https://doi.org/10.1016/J.SSC.2008.02.024.

[18] N. M, M. O, C. J, P. V, L. J, H. L, G. Y, B. MW, Two-dimensional transition metal carbides, ACS Nano. 6 (2012) 1322–1331. https://doi.org/10.1021/NN204153H.

[19] H.T. Tan, W. Sun, L. Wang, Q. Yan, 2D Transition Metal Oxides/Hydroxides for Energy-Storage Applications, ChemNanoMat. 2 (2016) 562–577. https://doi.org/10.1002/CNMA.201500177.

[20] G. Wang, L. Zhang, J. Zhang, A review of electrode materials for electrochemical

supercapacitors, Chem. Soc. Rev. 41 (2012) 797–828. https://doi.org/10.1039/C1CS15060J.

[21] D. Pech, M. Brunet, H. Durou, P. Huang, V. Mochalin, Y. Gogotsi, P.L. Taberna, P. Simon, Ultrahigh-power micrometre-sized supercapacitors based on onion-like carbon, Nat. Nanotechnol. 2010 59. 5 (2010) 651–654. https://doi.org/10.1038/nnano.2010.162.

[22] R.P. Feynman, Plenty of Room at the Bottom, (n.d.).

[23] R.F. Frindt, Optical Absorption of a Few Unit-Cell Layers of MoS2, Phys. Rev. 140 (1965) 1962–1965. https://doi.org/10.1103/PhysRev.140.A536.

[24] R.F. Frindt, Single crystals of MoS2 several molecular layers thick, J. Appl. Phys. 37 (1966) 1928–1929. https://doi.org/10.1063/1.1708627.

[25] P. Joensen, R.F. Frindt, S.R. Morrison, Single-layer MoS2, Mater. Res. Bull. 21 (1986) 457–461. https://doi.org/10.1016/0025-5408(86)90011-5.

[26] K.S. Novoselov, A.K. Geim, S. V. Morozov, D. Jiang, Y. Zhang, S. V. Dubonos, I. V. Grigorieva, A.A. Firsov, Electric field in atomically thin carbon films, Science (80-.). 306 (2004) 666–669. https://doi.org/10.1126/science.1102896.

[27] M. Velický, M.A. Bissett, P.S. Toth, H. V. Patten, S.D. Worrall, A.N.J. Rodgers, E.W. Hill, I.A. Kinloch, K.S. Novoselov, T. Georgiou, L. Britnell, R.A.W. Dryfe, Electron transfer kinetics on natural crystals of MoS 2 and graphite, Phys. Chem. Chem. Phys. 17 (2015) 17844–17853. https://doi.org/10.1039/C5CP02490K.

[28] C. Yang, H.F. Wang, Q. Xu, Recent Advances in Two-dimensional Materials for Electrochemical Energy Storage and Conversion, Chem. Res. Chinese Univ. 2020 361. 36 (2020) 10–23. https://doi.org/10.1007/S40242-020-9068-7.

[29] B. Jia, 2D optical materials and the implications for photonics, APL Photonics. 4 (2019) 080401. https://doi.org/10.1063/1.5120030.

[30] T. Hu, X. Mei, Y. Wang, X. Weng, R. Liang, M. Wei, Two-dimensional nanomaterials: fascinating materials in biomedical field, Sci. Bull. 64 (2019) 1707–1727. https://doi.org/10.1016/J.SCIB.2019.09.021.

[31] A. Jayakumar, A. Surendranath, M. PV, 2D materials for next generation healthcare

applications, Int. J. Pharm. 551 (2018) 309–321. https://doi.org/10.1016/j.ijpharm.2018.09.041.

[32] Y. Sun, S. Gao, F. Lei, Y. Xie, Atomically-thin two-dimensional sheets for understanding active sites in catalysis, Chem. Soc. Rev. (2015). https://doi.org/10.1039/c4cs00236a.

[33] M. Zeng, Y. Xiao, J. Liu, K. Yang, L. Fu, Exploring Two-Dimensional Materials toward the Next-Generation Circuits: From Monomer Design to Assembly Control, Chem. Rev. 118 (2018) 6236–6296. https://doi.org/10.1021/acs.chemrev.7b00633.

[34] Q.H. Wang, K. Kalantar-Zadeh, A. Kis, J.N. Coleman, M.S. Strano, Electronics and optoelectronics of two-dimensional transition metal dichalcogenides, Nat. Nanotechnol. 7 (2012) 699–712. https://doi.org/10.1038/NNANO.2012.193.

[35] C. Lan, Z. Shi, R. Cao, C. Li, H. Zhang, 2D materials beyond graphene toward Si integrated infrared optoelectronic devices, Nanoscale. 12 (2020) 11784–11807. https://doi.org/10.1039/D0NR02574G.

[36] J. Cheng, C. Wang, X. Zou, L. Liao, Recent Advances in Optoelectronic Devices Based on 2D Materials and Their Heterostructures, Adv. Opt. Mater. 7 (2019) 1800441. https://doi.org/10.1002/ADOM.201800441.

[37] A. Bolotsky, D. Butler, C. Dong, K. Gerace, N.R. Glavin, C. Muratore, J.A. Robinson, A. Ebrahimi, Two-Dimensional Materials in Biosensing and Healthcare: From In Vitro Diagnostics to Optogenetics and Beyond, ACS Nano. 13 (2019) 9781–9810. https://doi.org/10.1021/ACSNANO.9B03632.

[38] C.W. Lee, J.M. Suh, H.W. Jang, Chemical Sensors Based on Two-Dimensional (2D) Materials for Selective Detection of Ions and Molecules in Liquid, Front. Chem. 7 (2019) 708. https://doi.org/10.3389/FCHEM.2019.00708/BIBTEX.

[39] P.W. Dunne, A.S. Munn, C.L. Starkey, E.H. Lester, The sequential continuous-flow hydrothermal synthesis of molybdenum disulphide, Chem. Commun. 51 (2015) 4048–4050. https://doi.org/10.1039/c4cc10158h.

[40] R. Kurapati, K. Kostarelos, M. Prato, A. Bianco, Biomedical Uses for 2D Materials Beyond Graphene: Current Advances and Challenges Ahead, Adv. Mater. 28 (2016) 6052–6074. https://doi.org/10.1002/adma.201506306.

[41] T. Kuila, S. Bose, A.K. Mishra, P. Khanra, N.H. Kim, J.H. Lee, Chemical functionalization of graphene and its applications, Prog. Mater. Sci. 57 (2012) 1061–1105. https://doi.org/10.1016/j.pmatsci.2012.03.002.

[42] E. Jimenez-Cervantes, J. López-Barroso, A.L. Martínez-Hernández, C. Velasco-Santos, Graphene-Based Materials Functionalization with Natural Polymeric Biomolecules, in: Recent Adv. Graphene Res., IntechOpen, 2016: pp. 257–298. https://doi.org/10.5772/64001.

[43] Y. Wen, T.E. Rufford, X. Chen, N. Li, M. Lyu, L. Dai, L. Wang, Nitrogen-doped Ti3C2Tx MXene electrodes for high-performance supercapacitors, Nano Energy. 38 (2017) 368–376. https://doi.org/10.1016/j.nanoen.2017.06.009.

[44] H. Rui, R. Xing, Z. Xu, Y. Hou, S. Goo, S. Sun, Synthesis, functionalization, and biomedical applications of multifunctional magnetic nanoparticles, Adv. Mater. 22 (2010) 2729–2742. https://doi.org/10.1002/adma.201000260.

[45] S. Vardharajula, S.Z. Ali, P.M. Tiwari, E. Eroğlu, K. Vig, V.A. Dennis, S.R. Singh, Functionalized carbon nanotubes: Biomedical applications, Int. J. Nanomedicine. 7 (2012) 5361–5374. https://doi.org/10.2147/IJN.S35832.

[46] Continuous Hydrothermal Flow Synthesis | Nano2D, (n.d.). https://www.nano2d.co.uk/continuous-hydrothermal-flow-synthe (accessed November 15, 2021).

[47] J. He, L. Tao, H. Zhang, B. Zhou, J. Li, Emerging 2D materials beyond graphene for ultrashort pulse generation in fiber lasers, Nanoscale. 11 (2019) 2577–2593. https://doi.org/10.1039/c8nr09368g.

[48] B. Anasori, M.R. Lukatskaya, Y. Gogotsi, 2D metal carbides and nitrides (MXenes) for energy storage, Nat. Rev. Mater. 2 (2017) 16098. https://doi.org/10.1038/natrevmats.2016.98.

[49] Q. Tang, D.E. Jiang, Stabilization and band-gap tuning of the 1T-MoS<inf>2</inf> monolayer by covalent functionalization, Chem. Mater. 27 (2015) 3743–3748. https://doi.org/10.1021/acs.chemmater.5b00986.

[50] K. Huang, Z. Li, J. Lin, G. Han, P. Huang, Two-dimensional transition metal carbides and nitrides (MXenes) for biomedical applications, Chem. Soc. Rev. 47 (2018) 5109–

5124. https://doi.org/10.1039/c7cs00838d.

[51] S.Z. Butler, S.M. Hollen, L. Cao, Y. Cui, J.A. Gupta, H.R. Gutiérrez, T.F. Heinz, S.S. Hong, J. Huang, A.F. Ismach, E. Johnston-Halperin, M. Kuno, V. V. Plashnitsa, R.D. Robinson, R.S. Ruoff, S. Salahuddin, J. Shan, L. Shi, M.G. Spencer, M. Terrones, W. Windl, J.E. Goldberger, Progress, Challenges, and Opportunities in Two-Dimensional Materials Beyond Graphene, ACS Nano. 7 (2013) 2898–2926. https://doi.org/10.1021/NN400280C.

[52] H. Nakano, M. Ishii, H. Nakamura, Preparation and structure of novel siloxene nanosheets, Chem. Commun. (2005) 2945–2947. https://doi.org/10.1039/B500758E.

[53] H. Nakano, T. Mitsuoka, M. Harada, K. Horibuchi, H. Nozaki, N. Takahashi, T. Nonaka, Y. Seno, H. Nakamura, Soft Synthesis of Single-Crystal Silicon Monolayer Sheets, Angew. Chemie Int. Ed. 45 (2006) 6303–6306. https://doi.org/10.1002/ANIE.200600321.

[54] E. V. Castro, H. Ochoa, M.I. Katsnelson, R. V. Gorbachev, D.C. Elias, K.S. Novoselov, A.K. Geim, F. Guinea, Limits on charge carrier mobility in suspended graphene due to flexural phonons, Phys. Rev. Lett. 105 (2010) 266601–266605. https://doi.org/10.1103/PhysRevLett.105.266601.

[55] Y. Han, Y. Ge, Y. Chao, C. Wang, G.G. Wallace, Recent progress in 2D materials for flexible supercapacitors, J. Energy Chem. 27 (2018) 57–72. https://doi.org/10.1016/j.jechem.2017.10.033.

[56] T. Stauber, N.M.R. Peres, F. Guinea, Electronic transport in graphene: A semiclassical approach including midgap states, Phys. Rev. B - Condens. Matter Mater. Phys. 76 (2007) 205423. https://doi.org/10.1103/PHYSREVB.76.205423/FIGURES/4/MEDIUM.

[57] C.J. Zhang, M.P. Kremer, A. Seral-Ascaso, S.H. Park, N. McEvoy, B. Anasori, Y. Gogotsi, V. Nicolosi, Stamping of Flexible, Coplanar Micro-Supercapacitors Using MXene Inks, Adv. Funct. Mater. 28 (2018) 1705506. https://doi.org/10.1002/adfm.201705506.

[58] P. Wang, Y.J. Zhao, L.X. Wen, J.F. Chen, Z.G. Lei, Ultrasound-microwave-assisted synthesis of MnO2 supercapacitor electrode materials, Ind. Eng. Chem. Res. 53 (2014)

20116–20123. https://doi.org/10.1021/ie5025485.

[59] M. Kim, Y. Hwang, J. Kim, Process dependent graphene/MnO2 composites for supercapacitors, Chem. Eng. J. (2013). https://doi.org/10.1016/j.cej.2013.06.095.

[60] X. Guo, S. Yang, D. Wang, A. Chen, Y. Wang, P. Li, G. Liang, C. Zhi, The energy storage mechanisms of MnO2 in batteries, Curr. Opin. Electrochem. 30 (2021) 100769. https://doi.org/10.1016/J.COELEC.2021.100769.

[61] L. Chen, D. Zhu, Effects of different phases of MnO2 nanorods on the catalytic thermal decomposition of ammonium perchlorate, Ceram. Int. 41 (2015) 7054–7058. https://doi.org/10.1016/J.CERAMINT.2015.02.011.

[62] P. Canepa, G. Sai Gautam, D.C. Hannah, R. Malik, M. Liu, K.G. Gallagher, K.A. Persson, G. Ceder, Odyssey of Multivalent Cathode Materials: Open Questions and Future Challenges, Chem. Rev. 117 (2017) 4287–4341. https://doi.org/10.1021/ACS.CHEMREV.6B00614.

[63] V. Subramanian, H. Zhu, R. Vajtai, P.M. Ajayan, B. Wei, Hydrothermal Synthesis and Pseudocapacitance Properties of MnO2 Nanostructures, J. Phys. Chem. B. 109 (2005) 20207–20214. https://doi.org/10.1021/JP0543330.

[64] J. Tizfahm, M. Aghazadeh, M.G. Maragheh, M.R. Ganjali, P. Norouzi, F. Faridbod, Electrochemical preparation and evaluation of the supercapacitive performance of MnO2 nanoworms, Mater. Lett. 167 (2016) 153–156. https://doi.org/10.1016/J.MATLET.2015.12.158.

[65] R.N. Reddy, R.G. Reddy, Sol–gel MnO2 as an electrode material for electrochemical capacitors, J. Power Sources. 124 (2003) 330–337. https://doi.org/10.1016/S0378-7753(03)00600-1.

[66] Y. Zhang, G.Y. Li, Y. Lv, L.Z. Wang, A.Q. Zhang, Y.H. Song, B.L. Huang, Electrochemical investigation of MnO2 electrode material for supercapacitors, Int. J. Hydrogen Energy. 36 (2011) 11760–11766. https://doi.org/10.1016/J.IJHYDENE.2011.06.020.

[67] J. Yan, Z. Fan, T. Wei, W. Qian, M. Zhang, F. Wei, Fast and reversible surface redox reaction of graphene–MnO2 composites as supercapacitor electrodes, Carbon N. Y. 48 (2010) 3825–3833. https://doi.org/10.1016/J.CARBON.2010.06.047.

[68] H. Wang, C. Peng, F. Peng, H. Yu, J. Yang, Facile synthesis of MnO2/CNT nanocomposite and its electrochemical performance for supercapacitors, Mater. Sci. Eng. B. 176 (2011) 1073–1078. https://doi.org/10.1016/J.MSEB.2011.05.043.

[69] I. Izwan Misnon, R. Jose, Charge storage in the PANI–α-MnO2 polymer–nanocomposite system, Mater. Today Proc. 41 (2021) 513–519. https://doi.org/10.1016/J.MATPR.2020.05.235.

[70] V.H. Nguyen, L.T.N. Huynh, T.H. Nguyen, T.P. Vu, M.L.P. Le, A. Grag, V.M. Tran, Promising electrode material using Ni-doped layered manganese dioxide for sodium-ion batteries, J. Appl. Electrochem. 48 (2018) 793–800. https://doi.org/10.1007/S10800-018-1196-0/FIGURES/11.

[71] A. Ramadoss, S.J. Kim, Improved activity of a graphene–TiO2 hybrid electrode in an electrochemical supercapacitor, Carbon N. Y. 63 (2013) 434–445. https://doi.org/10.1016/J.CARBON.2013.07.006.

[72] C. Xu, X. Wang, J. Zhu, Graphene−Metal Particle Nanocomposites, J. Phys. Chem. C. 112 (2008) 19841–19845. https://doi.org/10.1021/JP807989B.

[73] J. Li, X. Cheng, J. Sun, C. Brand, A. Shashurin, M. Reeves, M. Keidar, Paper-based ultracapacitors with carbon nanotubes-graphene composites, J. Appl. Phys. 115 (2014) 164301. https://doi.org/10.1063/1.4871290.

[74] J.R. Potts, D.R. Dreyer, C.W. Bielawski, R.S. Ruoff, Graphene-based polymer nanocomposites, Polymer (Guildf). 52 (2011) 5–25. https://doi.org/10.1016/J.POLYMER.2010.11.042.

[75] Q. Li, N. Mahmood, J. Zhu, Y. Hou, S. Sun, Graphene and its composites with nanoparticles for electrochemical energy applications, Nano Today. 9 (2014) 668–683. https://doi.org/10.1016/J.NANTOD.2014.09.002.

[76] L. Ji, Z. Lin, M. Alcoutlabi, X. Zhang, Recent developments in nanostructured anode materials for rechargeable lithium-ion batteries, Energy Environ. Sci. 4 (2011) 2682–2699. https://doi.org/10.1039/C0EE00699H.

[77] M.D. Stoller, S. Park, Y. Zhu, J. An, R.S. Ruoff, Graphene-Based Ultracapacitors, Nano Lett. 8 (2008) 3498–3502. https://doi.org/10.1021/NL802558Y.

[78] S.R.C. Vivekchand, C.S. Rout, K.S. Subrahmanyam, A. Govindaraj, C.N.R. Rao,

Graphene-based electrochemical supercapacitors, J. Chem. Sci. 2008 1201. 120 (2008) 9–13. https://doi.org/10.1007/S12039-008-0002-7.

[79] B. Mendoza-Sánchez, J. Coelho, A. Pokle, V. Nicolosi, A 2D graphene-manganese oxide nanosheet hybrid synthesized by a single step liquid-phase co-exfoliation method for supercapacitor applications, Electrochim. Acta. (2015). https://doi.org/10.1016/j.electacta.2015.06.030.

[80] S. Chen, J. Zhu, X. Wu, Q. Han, X. Wang, Graphene oxide-Mno2 nanocomposites for supercapacitors, ACS Nano. (2010). https://doi.org/10.1021/nn901311t.

[81] R. Samal, B. Chakraborty, C.S. Rout, Understanding the phase dependent energy storage performance of MnO2 nanostructures, J. Appl. Phys. 126 (2019) 045112. https://doi.org/10.1063/1.5119688.

[82] M. Zhou, X. Zhang, J. Wei, S. Zhao, L. Wang, B. Feng, Morphology-controlled synthesis and novel microwave absorption properties of hollow urchinlike α-MnO2 nanostructures, J. Phys. Chem. C. 115 (2011) 1398–1402. https://doi.org/10.1021/JP106652X/SUPPL_FILE/JP106652X_SI_001.PDF.

[83] S. Sun, P. Wang, Q. Wu, S. Wang, S. Fang, Template-free synthesis of mesoporous MnO2 under ultrasound irradiation for supercapacitor electrode, Mater. Lett. 137 (2014) 206–209. https://doi.org/10.1016/J.MATLET.2014.08.130.

[84] S.S. El-Deen, A.M. Hashem, A.E. Abdel Ghany, S. Indris, H. Ehrenberg, A. Mauger, C.M. Julien, Anatase TiO2 nanoparticles for lithium-ion batteries, Ionics (Kiel). 24 (2018) 2925–2934. https://doi.org/10.1007/s11581-017-2425-y.

[85] X. Yang, Y. Yang, H. Hou, Y. Zhang, L. Fang, J. Chen, X. Ji, Size-tunable single-crystalline anatase TiO2 cubes as anode materials for lithium ion batteries, J. Phys. Chem. C. 119 (2015) 3923–3930. https://doi.org/10.1021/jp512289g.

[86] K. Hashimoto, H. Irie, A. Fujishima, TiO2 Photocatalysis: A Historical Overview and Future Prospects, Assoc. Asia Pacific Phys. Soc. Bull. 44 (2007) 8269.

[87] D. Su, S. Dou, G. Wang, Anatase TiO2: Better Anode Material Than Amorphous and Rutile Phases of TiO2 for Na-Ion Batteries, Chem. Mater. 27 (2015) 6022–6029. https://doi.org/10.1021/ACS.CHEMMATER.5B02348/SUPPL_FILE/CM5B02348_SI_001.PDF.

[88] M. Landmann, E. Rauls, W.G. Schmidt, The electronic structure and optical response of rutile, anatase and brookite TiO2, J. Phys. Condens. Matter. 24 (2012). https://doi.org/10.1088/0953-8984/24/19/195503.

[89] Y. Qian, J. Du, D.J. Kang, Enhanced electrochemical performance of porous Co-doped TiO2 nanomaterials prepared by a solvothermal method, Microporous Mesoporous Mater. 273 (2019) 148–155. https://doi.org/10.1016/J.MICROMESO.2018.06.056.

[90] L. Kavan, M. Grätzel, J. Rathouský, A. Zukalb, Nanocrystalline TiO2 (Anatase) Electrodes: Surface Morphology, Adsorption, and Electrochemical Properties, J. Electrochem. Soc. 143 (1996) 394–400. https://doi.org/10.1149/1.1836455/XML.

[91] B. Munirathinam, H. Pydimukkala, N. Ramaswamy, L. Neelakantan, Influence of crystallite size and surface morphology on electrochemical properties of annealed TiO2 nanotubes, Appl. Surf. Sci. 355 (2015) 1245–1253. https://doi.org/10.1016/J.APSUSC.2015.08.017.

[92] H. Huang, W.K. Zhang, X.P. Gan, C. Wang, L. Zhang, Electrochemical investigation of TiO2/carbon nanotubes nanocomposite as anode materials for lithium-ion batteries, Mater. Lett. 61 (2007) 296–299. https://doi.org/10.1016/j.matlet.2006.04.053.

[93] Y. Zhang, Y. Yang, H. Hou, X. Yang, J. Chen, M. Jing, X. Jia, X. Ji, Enhanced sodium storage behavior of carbon coated anatase TiO2 hollow spheres, J. Mater. Chem. A. 3 (2015) 18944–18952. https://doi.org/10.1039/C5TA04009D.

[94] C. Ding, T. Nohira, R. Hagiwara, A high-capacity TiO2/C negative electrode for sodium secondary batteries with an ionic liquid electrolyte, J. Mater. Chem. A. 3 (2015) 20767–20771. https://doi.org/10.1039/C5TA04256A.

[95] P. Zheng, T. Liu, Y. Su, L. Zhang, S. Guo, TiO2 nanotubes wrapped with reduced graphene oxide as a high-performance anode material for lithium-ion batteries, Sci. Reports 2016 61. 6 (2016) 1–8. https://doi.org/10.1038/srep36580.

[96] J.S. Lee, K.H. You, C.B. Park, Highly Photoactive, Low Bandgap TiO2 Nanoparticles Wrapped by Graphene, Adv. Mater. 24 (2012) 1084–1088. https://doi.org/10.1002/ADMA.201104110.

[97] L. Sun, Z. Zhao, Y. Zhou, L. Liu, Anatase TiO2 nanocrystals with exposed {001} facets on graphene sheets via molecular grafting for enhanced photocatalytic

activity, Nanoscale. 4 (2012) 613–620. https://doi.org/10.1039/C1NR11411E.

[98] S. Anandan, T. Narasinga Rao, M. Sathish, D. Rangappa, I. Honma, M. Miyauchi, Superhydrophilic Graphene-Loaded TiO2 Thin Film for Self-Cleaning Applications, ACS Appl. Mater. Interfaces. 5 (2012) 207–212. https://doi.org/10.1021/AM302557Z.

[99] M. Naguib, M. Kurtoglu, V. Presser, J. Lu, J. Niu, M. Heon, L. Hultman, Y. Gogotsi, M.W. Barsoum, Two-dimensional nanocrystals produced by exfoliation of Ti 3AlC 2, Adv. Mater. 23 (2011) 4248–4253. https://doi.org/10.1002/adma.201102306.

[100] C. (John) Zhang, V. Nicolosi, Graphene and MXene-based transparent conductive electrodes and supercapacitors, Energy Storage Mater. (2019). https://doi.org/10.1016/j.ensm.2018.05.003.

[101] W. Hong, B.C. Wyatt, S.K. Nemani, B. Anasori, Double transition-metal MXenes: Atomistic design of two-dimensional carbides and nitrides, MRS Bull. 45 (2020) 850–861. https://doi.org/10.1557/MRS.2020.251/FIGURES/7.

[102] J. Yan, C.E. Ren, K. Maleski, C.B. Hatter, B. Anasori, P. Urbankowski, A. Sarycheva, Y. Gogotsi, Flexible MXene/Graphene Films for Ultrafast Supercapacitors with Outstanding Volumetric Capacitance, Adv. Funct. Mater. 27 (2017) 1701264. https://doi.org/10.1002/adfm.201701264.

[103] Z. Fan, Y. Wang, Z. Xie, D. Wang, Y. Yuan, H. Kang, B. Su, Z. Cheng, Y. Liu, Modified MXene/Holey Graphene Films for Advanced Supercapacitor Electrodes with Superior Energy Storage, Adv. Sci. 5 (2018) 18000750. https://doi.org/10.1002/advs.201800750.

[104] X. Xie, M.Q. Zhao, B. Anasori, K. Maleski, C.E. Ren, J. Li, B.W. Byles, E. Pomerantseva, G. Wang, Y. Gogotsi, Porous heterostructured MXene/carbon nanotube composite paper with high volumetric capacity for sodium-based energy storage devices, Nano Energy. 26 (2016) 513–523. https://doi.org/10.1016/J.NANOEN.2016.06.005.

[105] A.E. Allah, J. Wang, Y.V. Kaneti, T. Li, A.A. Farghali, M.H. Khedr, A.K. Nanjundan, B. Ding, H. Dou, X. Zhang, B. Yoshio, Y. Yamauchi, Auto-programmed heteroarchitecturing: Self-assembling ordered mesoporous carbon between two-dimensional Ti3C2Tx MXene layers, Nano Energy. 65 (2019) 103991.

https://doi.org/10.1016/J.NANOEN.2019.103991.

[106] T. Zhou, C. Wu, Y. Wang, A.P. Tomsia, M. Li, E. Saiz, S. Fang, R.H. Baughman, L. Jiang, Q. Cheng, Super-tough MXene-functionalized graphene sheets, Nat. Commun. 2020 111. 11 (2020) 1–11. https://doi.org/10.1038/s41467-020-15991-6.

[107] J. Jimmy, B. Kandasubramanian, Mxene functionalized polymer composites: Synthesis and applications, Eur. Polym. J. 122 (2020) 109367. https://doi.org/10.1016/J.EURPOLYMJ.2019.109367.

[108] Y.-T. Liu, P. Zhang, N. Sun, B. Anasori, Q.-Z. Zhu, H. Liu, Y. Gogotsi, B. Xu, Self-Assembly of Transition Metal Oxide Nanostructures on MXene Nanosheets for Fast and Stable Lithium Storage, Adv. Mater. 30 (2018) 1707334. https://doi.org/10.1002/ADMA.201707334.

[109] J. Yang, W. Bao, P. Jaumaux, S. Zhang, C. Wang, G. Wang, MXene-Based Composites: Synthesis and Applications in Rechargeable Batteries and Supercapacitors, Adv. Mater. Interfaces. 6 (2019) 1802004. https://doi.org/10.1002/ADMI.201802004.

[110] H. Tang, Q. Hu, M. Zheng, Y. Chi, X. Qin, H. Pang, Q. Xu, MXene–2D layered electrode materials for energy storage, Prog. Nat. Sci. Mater. Int. 28 (2018) 133–147. https://doi.org/10.1016/J.PNSC.2018.03.003.

[111] C. Yang, Y. Liu, X. Sun, Y. Zhang, L. Hou, Q. Zhang, C. Yuan, In-situ construction of hierarchical accordion-like TiO2/Ti3C2 nanohybrid as anode material for lithium and sodium ion batteries, Electrochim. Acta. 271 (2018) 165–172. https://doi.org/10.1016/j.electacta.2018.03.118.

[112] J. Low, L. Zhang, T. Tong, B. Shen, J. Yu, TiO2/MXene Ti3C2 composite with excellent photocatalytic CO2 reduction activity, J. Catal. 361 (2018) 255–266. https://doi.org/10.1016/J.JCAT.2018.03.009.

[113] J. Zhu, Y. Tang, C. Yang, F. Wang, M. Cao, Composites of TiO 2 Nanoparticles Deposited on Ti 3 C 2 MXene Nanosheets with Enhanced Electrochemical Performance , J. Electrochem. Soc. 163 (2016) A785–A791. https://doi.org/10.1149/2.0981605JES/XML.

[114] Y. Jiang, T. Sun, X. Xie, W. Jiang, J. Li, B. Tian, C. Su, Oxygen-Functionalized

Ultrathin Ti3C2Tx MXene for Enhanced Electrocatalytic Hydrogen Evolution, ChemSusChem. 12 (2019) 1368–1373. https://doi.org/10.1002/CSSC.201803032.

[115] J. Wang, G. Li, L. Li, Synthesis Strategies about 2D Materials, 2016. https://doi.org/10.5772/63918.

[116] A.K. Geim, K.S. Novoselov, The rise of graphene., Nat. Mater. (2007). https://doi.org/10.1038/nmat1849.

[117] S. Majumdar, P. Sujatha Devi, Synthesis of SnO2 Nanoparticles Using Ultrasonication, AIP Conf. Proc. 1276 (2010) 1. https://doi.org/10.1063/1.3504298.

[118] M. Chhowalla, H.S. Shin, G. Eda, L.J. Li, K.P. Loh, H. Zhang, The chemistry of two-dimensional layered transition metal dichalcogenide nanosheets, Nat. Chem. 2013 54. 5 (2013) 263–275. https://doi.org/10.1038/nchem.1589.

[119] T. Fujita, Y. Ito, Y. Tan, H. Yamaguchi, D. Hojo, A. Hirata, D. Voiry, M. Chhowalla, M. Chen, Chemically exfoliated ReS2 nanosheets, Nanoscale. 6 (2014) 12458–12462. https://doi.org/10.1039/C4NR03740E.

[120] Z. Zeng, Z. Yin, X. Huang, H. Li, Q. He, G. Lu, F. Boey, H. Zhang, Single-Layer Semiconducting Nanosheets: High-Yield Preparation and Device Fabrication, Angew. Chemie Int. Ed. 50 (2011) 11093–11097. https://doi.org/10.1002/ANIE.201106004.

[121] C.C. Piras, S. Fernández-Prieto, W.M. De Borggraeve, Ball milling: a green technology for the preparation and functionalisation of nanocellulose derivatives, Nanoscale Adv. 1 (2019) 937–947. https://doi.org/10.1039/C8NA00238J.

[122] M. Ago, T. Endo, K. Okajima, Effect of Solvent on Morphological and Structural Change of Cellulose under Ball-Milling, Polym. J. 2007 395. 39 (2007) 435–441. https://doi.org/10.1295/polymj.pj2006096.

[123] A.S. Khan, Z. Man, M.A. Bustam, C.F. Kait, M.I. Khan, N. Muhammad, A. Nasrullah, Z. Ullah, P. Ahmad, Impact of Ball-Milling Pretreatment on Pyrolysis Behavior and Kinetics of Crystalline Cellulose, Waste and Biomass Valorization. 3 (2016) 571–581. https://doi.org/10.1007/S12649-015-9460-6.

[124] W. Zhao, M. Fang, F. Wu, H. Wu, L. Wang, G. Chen, Preparation of graphene by exfoliation of graphite using wet ball milling, J. Mater. Chem. 20 (2010) 5817–5819. https://doi.org/10.1039/C0JM01354D.

[125] H. Zhao, H. Zeng, Y. Wu, S. Zhang, B. Li, Y. Huang, Facile scalable synthesis and superior lithium storage performance of ball-milled MoS2–graphite nanocomposites, J. Mater. Chem. A. 3 (2015) 10466–10470. https://doi.org/10.1039/C5TA00472A.

[126] M. Naguib, V.N. Mochalin, M.W. Barsoum, Y. Gogotsi, 25th anniversary article: MXenes: A new family of two-dimensional materials, Adv. Mater. (2014). https://doi.org/10.1002/adma.201304138.

[127] T.F. Emiru, D.W. Ayele, Controlled synthesis, characterization and reduction of graphene oxide: A convenient method for large scale production, Egypt. J. Basic Appl. Sci. (2017). https://doi.org/10.1016/j.ejbas.2016.11.002.

[128] W.S. Hummers, R.E. Offeman, Preparation of Graphitic Oxide, J. Am. Chem. Soc. 80 (2002) 1339. https://doi.org/10.1021/JA01539A017.

[129] D.C. Marcano, D. V. Kosynkin, J.M. Berlin, A. Sinitskii, Z. Sun, A. Slesarev, L.B. Alemany, W. Lu, J.M. Tour, Improved synthesis of graphene oxide, ACS Nano. 4 (2010) 4806–4814. https://doi.org/10.1021/nn1006368.

[130] S. Park, Y. Hu, J.O. Hwang, E.S. Lee, L.B. Casabianca, W. Cai, J.R. Potts, H.W. Ha, S. Chen, J. Oh, S.O. Kim, Y.H. Kim, Y. Ishii, R.S. Ruoff, Chemical structures of hydrazine-treated graphene oxide and generation of aromatic nitrogen doping, Nat. Commun. 2012 31. 3 (2012) 1–8. https://doi.org/10.1038/ncomms1643.

[131] J. Zhang, H. Yang, G. Shen, P. Cheng, J. Zhang, S. Guo, Reduction of graphene oxide viaL-ascorbic acid, Chem. Commun. 46 (2010) 1112–1114. https://doi.org/10.1039/B917705A.

[132] E. Jimenez-Cervantes, J. López-Barroso, A.L. Martínez-Hernández, C. Velasco-Santos, Graphene-Based Materials Functionalization with Natural Polymeric Biomolecules, in: Recent Adv. Graphene Res., 2016: pp. 258–287. https://doi.org/10.5772/64001.

[133] Y. Zhu, C. Cao, S. Tao, W. Chu, Z. Wu, Y. Li, Ultrathin Nickel Hydroxide and Oxide Nanosheets: Synthesis, Characterizations and Excellent Supercapacitor Performances, Sci. Reports 2014 41. 4 (2014) 1–7. https://doi.org/10.1038/srep05787.

[134] M. Thamima, S. Karuppuchamy, Microwave-assisted Synthesis of Zinc Oxide Nanoparticles, Procedia Mater. Sci. 11 (2015) 320–325.

https://doi.org/10.1016/J.MSPRO.2015.11.101.

[135] X. Xiao, H. Wang, P. Urbankowski, Y. Gogotsi, Topochemical synthesis of 2D materials, Chem. Soc. Rev. 47 (2018) 8744–8765. https://doi.org/10.1039/C8CS00649K.

[136] M. Naguib, J. Come, B. Dyatkin, V. Presser, P.L. Taberna, P. Simon, M.W. Barsoum, Y. Gogotsi, MXene: A promising transition metal carbide anode for lithium-ion batteries, Electrochem. Commun. 16 (2012) 61–64. https://doi.org/10.1016/j.elecom.2012.01.002.

[137] Z. Cai, B. Liu, X. Zou, H.M. Cheng, Chemical Vapor Deposition Growth and Applications of Two-Dimensional Materials and Their Heterostructures, Chem. Rev. 118 (2018) 6091–6133. https://doi.org/10.1021/ACS.CHEMREV.7B00536.

[138] D. Wei, Y. Liu, Y. Wang, H. Zhang, L. Huang, G. Yu, Synthesis of n-doped graphene by chemical vapor deposition and its electrical properties, Nano Lett. 9 (2009) 1752–1758. https://doi.org/10.1021/NL803279T/SUPPL_FILE/NL803279T_SI_001.PDF.

[139] Q. Zhang, D. Sando, V. Nagarajan, Cite this, J. Mater. Chem. C. 4 (2016) 4092. https://doi.org/10.1039/c6tc00243a.

[140] A.E. Karu, M. Beer, Pyrolytic Formation of Highly Crystalline Graphite Films, Cit. J. Appl. Phys. 37 (1966) 83911. https://doi.org/10.1063/1.1708759.

[141] T.A. Land, T. Michely, R.J. Behm, J.C. Hemminger, G. Comsa, STM investigation of single layer graphite structures produced on Pt(111) by hydrocarbon decomposition, Surf. Sci. 264 (1992) 261–270. https://doi.org/10.1016/0039-6028(92)90183-7.

[142] J. Coraux, A.T. N'Diaye, C. Busse, T. Michely, Structural Coherency of Graphene on Ir(111), Nano Lett. 8 (2008) 565–570. https://doi.org/10.1021/NL0728874.

[143] S. Hussain, M.W. Iqbal, J. Park, M. Ahmad, J. Singh, J. Eom, J. Jung, Physical and electrical properties of graphene grown under different hydrogen flow in low pressure chemical vapor deposition, Nanoscale Res. Lett. 9 (2014) 1–9. https://doi.org/10.1186/1556-276X-9-546/FIGURES/8.

[144] M. Saeed, J.D. Robson, I.A. Kinloch, B. Derby, C. Da Liao, S. Al-Awadhi, E. Al-Nasrallah, The formation mechanism of hexagonal Mo2C defects in CVD graphene grown on liquid copper, Phys. Chem. Chem. Phys. 22 (2020) 2176–2180.

https://doi.org/10.1039/C9CP05618A.

[145] K.S. Kim, Y. Zhao, H. Jang, S.Y. Lee, J.M. Kim, K.S. Kim, J.H. Ahn, P. Kim, J.Y. Choi, B.H. Hong, Large-scale pattern growth of graphene films for stretchable transparent electrodes, Nat. 2009 4577230. 457 (2009) 706–710. https://doi.org/10.1038/nature07719.

[146] Z. Tu, Z. Liu, Y. Li, F. Yang, L. Zhang, Z. Zhao, C. Xu, S. Wu, H. Liu, H. Yang, P. Richard, Controllable growth of 1–7 layers of graphene by chemical vapour deposition, Undefined. 73 (2014) 252–258. https://doi.org/10.1016/J.CARBON.2014.02.061.

[147] G.J.M. Fechine, I. Martin-Fernandez, G. Yiapanis, R. Bentini, E.S. Kulkarni, R. V. Bof De Oliveira, X. Hu, I. Yarovsky, A.H. Castro Neto, B. Özyilmaz, Direct dry transfer of chemical vapor deposition graphene to polymeric substrates, Carbon N. Y. 83 (2015) 224–231. https://doi.org/10.1016/J.CARBON.2014.11.038.

[148] S. Wang, Y. Zhang, N. Abidi, L. Cabrales, Wettability and surface free energy of graphene films, Langmuir. 25 (2009) 11078–11081. https://doi.org/10.1021/LA901402F/SUPPL_FILE/LA901402F_SI_001.XLS.

[149] Y. Hernandez, V. Nicolosi, M. Lotya, F.M. Blighe, Z. Sun, S. De, I.T. McGovern, B. Holland, M. Byrne, Y.K. Gun'ko, J.J. Boland, P. Niraj, G. Duesberg, S. Krishnamurthy, R. Goodhue, J. Hutchison, V. Scardaci, A.C. Ferrari, J.N. Coleman, High-yield production of graphene by liquid-phase exfoliation of graphite, Nat. Nanotechnol. 2008 39. 3 (2008) 563–568. https://doi.org/10.1038/nnano.2008.215.

[150] C.E. Hamilton, J.R. Lomeda, Z. Sun, J.M. Tour, A.R. Barron, High-Yield Organic Dispersions of Unfunctionalized Graphene, (n.d.). https://doi.org/10.1021/nl9016623.

[151] M. Lotya, Y. Hernandez, P.J. King, R.J. Smith, V. Nicolosi, L.S. Karlsson, F.M. Blighe, S. De, W. Zhiming, I.T. McGovern, G.S. Duesberg, J.N. Coleman, Liquid phase production of graphene by exfoliation of graphite in surfactant/water solutions, J. Am. Chem. Soc. 131 (2009) 3611–3620. https://doi.org/10.1021/ja807449u.

[152] S.P. Economopoulos, G. Rotas, Y. Miyata, H. Shinohara, N. Tagmatarchis, Exfoliation and chemical modification using microwave irradiation affording highly functionalized graphene, ACS Nano. 4 (2010) 7499–7507.

https://doi.org/10.1021/NN101735E/SUPPL_FILE/NN101735E_SI_001.PDF.

[153] A. Ciesielski, P. Samorì, Graphene via sonication assisted liquid-phase exfoliation, Chem. Soc. Rev. 43 (2013) 381–398. https://doi.org/10.1039/C3CS60217F.

[154] T. Hasan, F. Torrisi, Z. Sun, D. Popa, V. Nicolosi, G. Privitera, F. Bonaccorso, A.C. Ferrari, Solution-phase exfoliation of graphite for ultrafast photonics, Phys. Status Solidi. 247 (2010) 2953–2957. https://doi.org/10.1002/PSSB.201000339.

[155] M. Naguib, O. Mashtalir, M.R. Lukatskaya, B. Dyatkin, C. Zhang, V. Presser, Y. Gogotsi, M.W. Barsoum, One-step synthesis of nanocrystalline transition metal oxides on thin sheets of disordered graphitic carbon by oxidation of MXenes, Chem. Commun. 50 (2014) 7420–7423. https://doi.org/10.1039/c4cc01646g.

[156] J. Sherwood, M. De bruyn, A. Constantinou, L. Moity, C.R. McElroy, T.J. Farmer, T. Duncan, W. Raverty, A.J. Hunt, J.H. Clark, Dihydrolevoglucosenone (Cyrene) as a bio-based alternative for dipolar aprotic solvents, Chem. Commun. 50 (2014) 9650–9652. https://doi.org/10.1039/C4CC04133J.

[157] A. Misefari, Investigation of the spectroscopic, chemical and physical properties of Cyrene and its hydrate, (2017). https://etheses.whiterose.ac.uk/18284/ (accessed March 5, 2022).

[158] Z.Y. Ma, Z.L. Yu, Z.L. Xu, L.F. Bu, H.R. Liu, Y.B. Zhu, B. Qin, T. Ma, H.J. Zhan, L. Xu, H.A. Wu, H. Ding, S.H. Yu, Origin of Batch Hydrothermal Fluid Behavior and Its Influence on Nanomaterial Synthesis, Matter. 2 (2020) 1270–1282. https://doi.org/10.1016/J.MATT.2020.02.015.

[159] P.W. Dunne, A.S. Munn, C.L. Starkey, T.A. Huddle, E.H. Lester, Continuous-flow hydrothermal synthesis for the production of inorganic nanomaterials, Philos. Trans. R. Soc. A Math. Phys. Eng. Sci. 373 (2015) 20150015. https://doi.org/10.1098/rsta.2015.0015.

[160] C. Xu, Continual and Batch Hydrothermal Synthesis of Metal Oxide Nanoparticles and Metal Oxide-Activated Carbon Nanocomposites, 2006.

[161] K. Byrappa, M. Yoshimura, Handbook of Hydrothermal Technology, in: Handb. Hydrothermal Technol., 2013: pp. 1–81. https://doi.org/10.1016/C2009-0-20354-0.

[162] R. Younas, S. Hao, L. Zhang, S. Zhang, Hydrothermal liquefaction of rice straw with

NiO nanocatalyst for bio-oil production, Renew. Energy. 113 (2017) 532–545. https://doi.org/10.1016/j.renene.2017.06.032.

[163] S. Kellici, J. Acord, J. Ball, H.S. Reehal, D. Morgan, B. Saha, A single rapid route for the synthesis of reduced graphene oxide with antibacterial activities, RSC Adv. 4 (2014) 14858–14861. https://doi.org/10.1039/c3ra47573e.

[164] I.-A. Baragau, N.P. Power, D.J. Morgan, T. Heil, R.A. Lobo, C.S. Roberts, M. Titirici, S. Dunn, S. Kellici, Continuous Hydrothermal Flow Synthesis of Blue-Luminescent, Excitation-Independent N-doped Carbon Quantum Dots as Nanosensors, J. Mater. Chem. A. (2020). https://doi.org/10.1039/C9TA11781D.

[165] G.P. Evans, M.J. Powell, I.D. Johnson, D.P. Howard, D. Bauer, J.A. Darr, I.P. Parkin, Room temperature vanadium dioxide–carbon nanotube gas sensors made via continuous hydrothermal flow synthesis, Sensors Actuators, B Chem. 255 (2018) 1119–1129. https://doi.org/10.1016/j.snb.2017.07.152.

[166] S. Kellici, J. Acord, N.P. Power, D.J. Morgan, P. Coppo, T. Heil, B. Saha, Rapid synthesis of graphene quantum dots using a continuous hydrothermal flow synthesis approach, RSC Adv. 7 (2017) 14716–14720. https://doi.org/10.1039/c7ra00127d.

[167] S. Kellici, J. Acord, A. Vaughn, N.P. Power, D.J. Morgan, T. Heil, S.P. Facq, G.I. Lampronti, Calixarene Assisted Rapid Synthesis of Silver-Graphene Nanocomposites with Enhanced Antibacterial Activity, ACS Appl. Mater. Interfaces. 8 (2016) 19038–19046. https://doi.org/10.1021/acsami.6b06052.

[168] R. Saada, S. Kellici, T. Heil, D. Morgan, B. Saha, Greener synthesis of dimethyl carbonate using a novel ceria-zirconia oxide/graphene nanocomposite catalyst, Appl. Catal. B Environ. 168–169 (2015) 353–362. https://doi.org/10.1016/j.apcatb.2014.12.013.

[169] R. Saada, O. AboElazayem, S. Kellici, T. Heil, D. Morgan, G.I. Lampronti, B. Saha, Greener synthesis of dimethyl carbonate using a novel tin-zirconia/graphene nanocomposite catalyst, Appl. Catal. B Environ. 226 (2018) 451–462. https://doi.org/10.1016/j.apcatb.2017.12.081.

[170] V. Middelkoop, T. Slater, M. Florea, F. Neațu, S. Danaci, V. Onyenkeadi, K. Boonen, B. Saha, I.A. Baragau, S. Kellici, Next frontiers in cleaner synthesis: 3D printed

graphene-supported CeZrLa mixed-oxide nanocatalyst for CO 2 utilisation and direct propylene carbonate production, J. Clean. Prod. 214 (2019) 606–614. https://doi.org/10.1016/j.jclepro.2018.12.274.

[171] A.J. Hunt, T.M. Attard, Supercritical and Other High-pressure Solvent Systems, Royal Society of Chemistry, Cambridge, 2018. https://doi.org/10.1039/9781788013543.

[172] M. Claverie, M. Diez-Garcia, F. Martin, C. Aymonier, Continuous Synthesis of Nanominerals in Supercritical Water, Chem. - A Eur. J. 25 (2019) 5814–5823. https://doi.org/10.1002/chem.201805435.

[173] J.A. Darr, J. Zhang, N.M. Makwana, X. Weng, Continuous Hydrothermal Synthesis of Inorganic Nanoparticles: Applications and Future Directions, Chem. Rev. 117 (2017) 11125–11238. https://doi.org/10.1021/acs.chemrev.6b00417.

[174] S. Kellici, J. Acord, N.P. Power, D.J. Morgan, P. Coppo, T. Heil, B. Saha, Rapid synthesis of graphene quantum dots using a continuous hydrothermal flow synthesis approach, 7 (2017) 14716–14720. https://doi.org/10.1039/C7RA00127D.

[175] S. Kellici, J. Acord, K.E. Moore, N.P. Power, V. Middelkoop, D.J. Morgan, T. Heil, P. Coppo, I.A. Baragau, C.L. Raston, Continuous hydrothermal flow synthesis of graphene quantum dots, React. Chem. Eng. (2018). https://doi.org/10.1039/c8re00158h.

[176] S. Kellici, J. Acord, K.E. Moore, N.P. Power, V. Middelkoop, D.J. Morgan, T. Heil, P. Coppo, I.A. Baragau, C.L. Raston, Continuous hydrothermal flow synthesis of graphene quantum dots, React. Chem. Eng. 3 (2018) 949–958. https://doi.org/10.1039/c8re00158h.

[177] P. Caramazana-González, P.W. Dunne, M. Gimeno-Fabra, M. Zilka, M. Ticha, B. Stieberova, F. Freiberg, J. McKechnie, E.H. Lester, Assessing the life cycle environmental impacts of titania nanoparticle production by continuous flow solvo/hydrothermal syntheses, Green Chem. 19 (2017) 1536–1547. https://doi.org/10.1039/c6gc03357a.

[178] B.G. Pollet, I. Staffell, J.L. Shang, Current status of hybrid, battery and fuel cell electric vehicles: From electrochemistry to market prospects, Electrochim. Acta. 84 (2012) 235–249. https://doi.org/10.1016/j.electacta.2012.03.172.

[179] P.F. Ribeiro, B.K. Johnson, M.L. Crow, A. Arsoy, Y. Liu, Energy Storage systems for Advances Power Applications, Proc. IEEE. (2001). https://doi.org/10.1109/5.975900.

[180] P. Simon, Y. Gogotsi, B. Dunn, Where do batteries end and supercapacitors begin?, Science (80-.). (2014). https://doi.org/10.1126/science.1249625.

[181] M.A.V. F.R.S., R.H.S.J.B.B.K.B. P.R.S., I. On the electricity excited by the mere contact of conducting substances of different kinds, Http://Dx.Doi.Org/10.1080/14786440008562590. 7 (2010) 289–311. https://doi.org/10.1080/14786440008562590.

[182] P. Kurzweil, Gaston Planté and his invention of the lead–acid battery—The genesis of the first practical rechargeable battery, J. Power Sources. 195 (2010) 4424–4434. https://doi.org/10.1016/J.JPOWSOUR.2009.12.126.

[183] D. (Dietrich) Berndt, Maintenance-free batteries: lead-acid, nickel/cadmium, nickel/hydride, (1993) 362.

[184] U. Köhler, C. Antonius, P. Bäuerlein, Advances in alkaline batteries, J. Power Sources. 127 (2004) 45–52. https://doi.org/10.1016/J.JPOWSOUR.2003.09.006.

[185] Q. Cao, H.P. Zhang, G.J. Wang, Q. Xia, Y.P. Wu, H.Q. Wu, A novel carbon-coated LiCoO2 as cathode material for lithium ion battery, Electrochem. Commun. 9 (2007) 1228–1232. https://doi.org/10.1016/J.ELECOM.2007.01.017.

[186] R. Ruffo, C. Wessells, R.A. Huggins, Y. Cui, Electrochemical behavior of LiCoO2 as aqueous lithium-ion battery electrodes, Electrochem. Commun. 11 (2009) 247–249. https://doi.org/10.1016/J.ELECOM.2008.11.015.

[187] L. Fan, R. Ma, Q. Zhang, X. Jia, B. Lu, Graphite Anode for a Potassium-Ion Battery with Unprecedented Performance, Angew. Chemie - Int. Ed. 58 (2019) 10500–10505. https://doi.org/10.1002/ANIE.201904258.

[188] B. Scrosati, Recent advances in lithium ion battery materials, Electrochim. Acta. 45 (2000) 2461–2466. https://doi.org/10.1016/S0013-4686(00)00333-9.

[189] H.J. Becker, Low voltage electrolytic capacitor, (1954).

[190] M. Sakai, Energy Storage Devices and Systems, 2013.

[191] M. Yoshio, R.J. Brodd, A. Kozawa, Lithium-ion batteries: Science and technologies,

2009. https://doi.org/10.1007/978-0-387-34445-4.

[192] U. Alli, K. McCarthy, I.-A. Baragau, N.P. Power, D.J. Morgan, S. Dunn, S. Killian, T. Kennedy, S. Kellici, In-situ continuous hydrothermal synthesis of TiO2 nanoparticles on conductive N-doped MXene nanosheets for binder-free Li-ion battery anodes, Chem. Eng. J. (2021) 132976. https://doi.org/10.1016/j.cej.2021.132976.

[193] J.R. Miller, A.F. Burke, Electrochemical capacitors: Challenges and opportunities for real-world applications, Electrochem. Soc. Interface. 17 (2008) 53–57. https://doi.org/10.1149/2.F08081IF/PDF.

[194] M. Vangari, T. Pryor, L. Jiang, Supercapacitors: Review of Materials and Fabrication Methods, J. Energy Eng. 139 (2013) 72–79. https://doi.org/10.1061/(asce)ey.1943-7897.0000102.

[195] R.B. Rakhi, Preparation and properties of manipulated carbon nanotube composites and applications, Nanocarbon Its Compos. Prep. Prop. Appl. (2019) 489–520. https://doi.org/10.1016/B978-0-08-102509-3.00016-X.

[196] M.F. El-Kady, V. Strong, S. Dubin, R.B. Kaner, Laser scribing of high-performance and flexible graphene-based electrochemical capacitors, Science (80-.). 335 (2012) 1326–1330. https://doi.org/10.1126/SCIENCE.1216744/SUPPL_FILE/EL-KADY-SOM.PDF.

[197] N. Casado, D. Mecerreyes, Chapter 1 Introduction to Redox Polymers: Classification, Characterization Methods and Main Applications, RSC Polym. Chem. Ser. 2021-January (2020) 1–26. https://doi.org/10.1039/9781788019743-00001.

[198] Z. Zhao, G.F. Richardson, Q. Meng, S. Zhu, H.C. Kuan, J. Ma, PEDOT-based composites as electrode materials for supercapacitors, Nanotechnology. 27 (2015) 042001. https://doi.org/10.1088/0957-4484/27/4/042001.

[199] S. Lim, H. Park, J. Yang, C. Kwak, J. Lee, Stable colloidal dispersion of octylated Ti3C2-MXenes in a nonpolar solvent, Colloids Surfaces A Physicochem. Eng. Asp. 579 (2019) 123648. https://doi.org/10.1016/j.colsurfa.2019.123648.

[200] T. Song, U. Paik, TiO2 as an active or supplemental material for lithium batteries, J. Mater. Chem. A. 4 (2015) 14–31. https://doi.org/10.1039/c5ta06888f.

[201] B. Qiu, M. Xing, J. Zhang, Mesoporous TiO2 nanocrystals grown in situ on graphene

aerogels for high photocatalysis and lithium-ion batteries, J. Am. Chem. Soc. 136 (2014) 5852–5855. https://doi.org/10.1021/ja500873u.

[202] B.A. Bhanvase, T.P. Shende, S.H. Sonawane, A review on graphene–TiO2 and doped graphene–TiO2 nanocomposite photocatalyst for water and wastewater treatment, Environ. Technol. Rev. 6 (2017) 1–14. https://doi.org/10.1080/21622515.2016.1264489.

[203] S.Y. Lee, S.J. Park, TiO2 photocatalyst for water treatment applications, J. Ind. Eng. Chem. 19 (2013) 1761–1769. https://doi.org/10.1016/j.jiec.2013.07.012.

[204] Y. Li, C. Ou, Y. Huang, Y. Shen, N. Li, H. Zhang, Towards fast and ultralong-life Li-ion battery anodes: embedding ultradispersed TiO2 quantum dots into three-dimensional porous graphene-like networks, Electrochim. Acta. 246 (2017) 1183–1192. https://doi.org/10.1016/j.electacta.2017.06.152.

[205] S. Moitzheim, S. De Gendt, P.M. Vereecken, Investigation of the Li-Ion Insertion Mechanism for Amorphous and Anatase TiO 2 Thin-Films, J. Electrochem. Soc. 166 (2019) A1–A9. https://doi.org/10.1149/2.1091816jes.

[206] L. Zhang, X.S. Zhao, Carbon-based materials as supercapacitor electrodes, Chem. Soc. Rev. 38 (2009) 2525–2531. https://doi.org/10.1039/b813846j.

[207] M. Armand, F. Endres, D.R. Mac Farlane, H. Ohno, B. Scrosati, Ionic-liquid materials for the electrochemical challenges of the future, Mater. Sustain. Energy A Collect. Peer-Reviewed Res. Rev. Artic. from Nat. Publ. Gr. (2010) 129–137. https://doi.org/10.1142/9789814317665_0020.

[208] R. Kötz, M. Carlen, Principles and applications of electrochemical capacitors, Electrochim. Acta. 45 (2000) 2483–2498. https://doi.org/10.1016/S0013-4686(00)00354-6.

[209] T.S. Mathis, N. Kurra, X. Wang, D. Pinto, P. Simon, Y. Gogotsi, Energy Storage Data Reporting in Perspective—Guidelines for Interpreting the Performance of Electrochemical Energy Storage Systems, Adv. Energy Mater. 9 (2019) 1902007. https://doi.org/10.1002/aenm.201902007.

[210] L. Nyholm, G. Nyström, A. Mihranyan, M. Strømme, L. Nyholm, G. Nyström, A. Mihranyan, M. Strømme, Toward Flexible Polymer and Paper-Based Energy Storage

Devices, Adv. Mater. 23 (2011) 3751–3769. https://doi.org/10.1002/ADMA.201004134.

[211] J. Xu, Y. Dou, Z. Wei, J. Ma, Y. Deng, Y. Li, H. Liu, S. Dou, Recent Progress in Graphite Intercalation Compounds for Rechargeable Metal (Li, Na, K, Al)-Ion Batteries, Adv. Sci. 4 (2017) 1700146. https://doi.org/10.1002/ADVS.201700146.

[212] L. Sun, X. Wang, Y. Wang, Q. Zhang, Roles of carbon nanotubes in novel energy storage devices, Carbon N. Y. 122 (2017) 462–474. https://doi.org/10.1016/j.carbon.2017.07.006.

[213] M. Javed, A.N.S. Saqib, Ata-ur-Rehman, B. Ali, M. Faizan, D.A. Anang, Z. Iqbal, S.M. Abbas, Carbon quantum dots from glucose oxidation as a highly competent anode material for lithium and sodium-ion batteries, Electrochim. Acta. 297 (2019) 250–257. https://doi.org/10.1016/j.electacta.2018.11.167.

[214] U. Farooq, F. Ahmed, S.A. Pervez, S. Rehman, M.A. Pope, M. Fichtner, E.P.L. Roberts, A stable TiO 2 –graphene nanocomposite anode with high rate capability for lithium-ion batteries, RSC Adv. 10 (2020) 29975–29982. https://doi.org/10.1039/D0RA05300G.

[215] S. Pervez, D. Kim, C.H. Doh, U. Farooq, A. Yaqub, J.H. Choi, Y.J. Lee, M. Saleem, High areal capacity for battery anode using rapidly growing self-ordered TiO2 nanotubes with a high aspect ratio, Mater. Lett. 137 (2014) 347–350. https://doi.org/10.1016/j.matlet.2014.09.032.

[216] W.J. Bernard, J.W. Cook -, F. Zastavnik, L. Pyl, J. Gu, al -, A. Gill, S.J. Benton, V. Man Tran, A. The Ha, M. Loan Phung Le, Capacitance behavior of nanostructured ϵ-MnO2/C composite electrode using different carbons matrix, Adv. Nat. Sci. Nanosci. Nanotechnol. 5 (2014) 025005. https://doi.org/10.1088/2043-6262/5/2/025005.

[217] Y. Wang, A. Hu, Carbon quantum dots: synthesis, properties and applications, J. Mater. Chem. C. 2 (2014) 6921–6939. https://doi.org/10.1039/C4TC00988F.

[218] H. Zhang, Ultrathin Two-Dimensional Nanomaterials, ACS Nano. 9 (2015) 9451–9469. https://doi.org/10.1021/acsnano.5b05040.

[219] G. Zhou, F. Li, H.M. Cheng, Progress in flexible lithium batteries and future prospects, Energy Environ. Sci. 7 (2014) 1307–1338. https://doi.org/10.1039/C3EE43182G.

[220] B. Liu, J.G. Zhang, G. Shen, Pursuing two-dimensional nanomaterials for flexible lithium-ion batteries, Nano Today. 11 (2016) 82–97. https://doi.org/10.1016/J.NANTOD.2016.02.003.

[221] M. Mao, J. Hu, H. Liu, Graphene-based materials for flexible electrochemical energy storage, Int. J. Energy Res. 39 (2015) 727–740. https://doi.org/10.1002/ER.3256.

[222] T. Xia, W. Zhang, Z. Wang, Y. Zhang, X. Song, J. Murowchick, V. Battaglia, G. Liu, X. Chen, Amorphous carbon-coated TiO2 nanocrystals for improved lithium-ion battery and photocatalytic performance, Nano Energy. 6 (2014) 109–118. https://doi.org/10.1016/j.nanoen.2014.03.012.

[223] M. Mao, F. Yan, C. Cui, J. Ma, M. Zhang, T. Wang, C. Wang, Pipe-Wire TiO 2 −Sn@Carbon Nanofibers Paper Anodes for Lithium and Sodium Ion Batteries, Nano Lett. 17 (2017) 3830–3836. https://doi.org/10.1021/acs.nanolett.7b01152.

[224] W. Wang, H. Lin, J. Li, N. Wang, Formation of titania nanoarrays by hydrothermal reaction and their application in photovoltaic cells, J. Am. Ceram. Soc. 91 (2008) 628–631. https://doi.org/10.1111/j.1551-2916.2007.02132.x.

[225] J. Gao, L. Li, Z. Zeng, X. Ma, R. Chen, C. Wang, K. Zhou, Superior acetone uptake of hierarchically N-doped potassium citrate-based porous carbon prepared by one-step carbonization, J. Mater. Sci. 54 (2019) 6186–6198. https://doi.org/10.1007/s10853-018-03300-y.

[226] B. Ahmed, D.H. Anjum, M.N. Hedhili, Y. Gogotsi, H.N. Alshareef, H2O2 assisted room temperature oxidation of Ti2C MXene for Li-ion battery anodes, Nanoscale. 8 (2016) 7580–7587. https://doi.org/10.1039/c6nr00002a.

[227] S. Thakur, N. Karak, Tuning of sunlight-induced self-cleaning and self-healing attributes of an elastomeric nanocomposite by judicious compositional variation of the TiO2-reduced graphene oxide nanohybrid, J. Mater. Chem. A. 3 (2015) 12334–12342. https://doi.org/10.1039/c5ta02162f.

[228] T. Zhou, Y. Zheng, H. Gao, S. Min, S. Li, H.K. Liu, Z. Guo, Surface Engineering and Design Strategy for Surface-Amorphized TiO2@Graphene Hybrids for High Power Li-Ion Battery Electrodes, Adv. Sci. 2 (2015) 1–8. https://doi.org/10.1002/advs.201500027.

[229] A. V. Fulari, M. V. Ramana Reddy, S.T. Jadhav, G.S. Ghodake, D.Y. Kim, G.M. Lohar, TiO2/reduced graphene oxide composite based nano-petals for supercapacitor application: effect of substrate, J. Mater. Sci. Mater. Electron. 29 (2018) 10814–10824. https://doi.org/10.1007/S10854-018-9146-5/FIGURES/9.

[230] I.A. Baragau, N.P. Power, D.J. Morgan, T. Heil, R.A. Lobo, C.S. Roberts, M.M. Titirici, S. Dunn, S. Kellici, Continuous hydrothermal flow synthesis of blue-luminescent, excitation-independent nitrogen-doped carbon quantum dots as nanosensors, J. Mater. Chem. A. 8 (2020) 3270–3279. https://doi.org/10.1039/c9ta11781d.

[231] R. Maharsi, A.F. Arif, T. Ogi, H. Widiyandari, F. Iskandar, Electrochemical properties of TiOX/rGO composite as an electrode for supercapacitors, RSC Adv. 9 (2019) 27896–27903. https://doi.org/10.1039/c9ra04346b.

[232] J. Xiao, Q. Li, Y. Bi, M. Cai, B. Dunn, T. Glossmann, J. Liu, T. Osaka, R. Sugiura, B. Wu, J. Yang, J.G. Zhang, M.S. Whittingham, Understanding and applying coulombic efficiency in lithium metal batteries, Nat. Energy. 5 (2020) 561–568. https://doi.org/10.1038/s41560-020-0648-z.

[233] H.Y. Lee, J.B. Goodenough, Supercapacitor Behavior with KCl Electrolyte, J. Solid State Chem. (1999). https://doi.org/10.1006/jssc.1998.8128.

[234] G. Dhanaraj, K. Byrappa, V. Prasad, M. Dudley, Crystal Growth Techniques and Characterization: An Overview, in: Springer Handb. Cryst. Growth, 2010. https://doi.org/10.1007/978-3-540-74761-1_1.

[235] Y. Wang, W. Lai, N. Wang, Z. Jiang, X. Wang, P. Zou, Z. Lin, H.J. Fan, F. Kang, C.-P. Wong, C. Yang, A reduced graphene oxide/mixed-valence manganese oxide composite electrode for tailorable and surface mountable supercapacitors with high capacitance and super-long life, Energy Environ. Sci. 10 (2017) 941–949. https://doi.org/10.1039/C6EE03773A.

[236] H.U. Shah, F. Wang, M.S. Javed, R. Saleem, M.S. Nazir, J. Zhan, Z.U.H. Khan, M.U. Farooq, S. Ali, Synthesis, characterization and electrochemical properties of α-MnO2 nanowires as electrode material for supercapacitors, Int. J. Electrochem. Sci. (2018). https://doi.org/10.20964/2018.07.48.

[237] W. Tang, X. Shan, S. Li, H. Liu, X. Wu, Y. Chen, Sol-gel process for the synthesis of ultrafine MnO2 nanowires and nanorods, Mater. Lett. (2014). https://doi.org/10.1016/j.matlet.2014.05.211.

[238] Y. Li, L. Xu, J. Gao, X. Jin, Hydrothermal fabrication of reduced graphene oxide/activated carbon/MnO2 hybrids with excellent electrochemical performance for supercapacitors, RSC Adv. (2017). https://doi.org/10.1039/c7ra07056j.

[239] ThermoscientificXPS, XPS Interpretation of Manganese, (n.d.). https://xpssimplified.com/elements/manganese.php (accessed April 7, 2019).

[240] H. Kumar, P. Sangwan, Synthesis and Characterization of MnO 2 Nanoparticles using Co-precipitation Technique, Int. J. Chem. Chem. Eng. (2013).

[241] P. Ragupathy, H.N. Vasan, N. Munichandraiah, Synthesis and Characterization of Nano-MnO[sub 2] for Electrochemical Supercapacitor Studies, J. Electrochem. Soc. (2007). https://doi.org/10.1149/1.2800163.

[242] X. Chen, S. Yan, N. Wang, S. Peng, C. Wang, Q. Hong, X. Zhang, S. Dai, Facile synthesis and characterization of ultrathin δ-MnO2 nanoflakes, RSC Adv. (2017). https://doi.org/10.1039/c7ra08962g.

[243] B. Yin, S. Zhang, H. Jiang, F. Qu, X. Wu, Phase-controlled synthesis of polymorphic MnO2 structures for electrochemical energy storage, J. Mater. Chem. A. (2015). https://doi.org/10.1039/c4ta06943a.

[244] J. Deng, L. Chen, Y. Sun, M. Ma, L. Fu, Interconnected MnO2 nanoflakes assembled on graphene foam as a binder-free and long-cycle life lithium battery anode, Carbon N. Y. 92 (2015) 177–184. https://doi.org/10.1016/j.carbon.2015.04.021.

[245] T. Zhao, S. Guo, X. Ji, Y. Zhao, X. Wang, Y. Cheng, J. Meng, Three-dimensional heterostructured MnO2/graphene/carbon nanotube composite on Ni foam for binder-free supercapacitor electrode, Http://Dx.Doi.Org/10.1080/1536383X.2017.1324850. 25 (2017) 391–396. https://doi.org/10.1080/1536383X.2017.1324850.

[246] K. Ghosh, C.Y. Yue, Development of 3D MoO3/graphene aerogel and sandwich-type polyaniline decorated porous MnO2−graphene hybrid film based high performance all-solid-state asymmetric supercapacitors, Electrochim. Acta. 276 (2018) 47–63. https://doi.org/10.1016/J.ELECTACTA.2018.04.162.

[247] G. Zhang, L. Ren, Z. Yan, L. Kang, Z. Lei, H. Xu, F. Shi, Z.H. Liu, Mesoporous-assembled MnO2 with large specific surface area, J. Mater. Chem. A. 3 (2015) 14567–14572. https://doi.org/10.1039/C5TA03326H.

[248] S. Kajiyama, L. Szabova, K. Sodeyama, H. Iinuma, R. Morita, K. Gotoh, Y. Tateyama, M. Okubo, A. Yamada, Sodium-Ion Intercalation Mechanism in MXene Nanosheets, ACS Nano. 10 (2016) 3334–3341. https://doi.org/10.1021/acsnano.5b06958.

[249] D. Xiong, X. Li, Z. Bai, S. Lu, Recent Advances in Layered Ti3C2Tx MXene for Electrochemical Energy Storage, Small. 14 (2018) 1703419. https://doi.org/10.1002/smll.201703419.

[250] C. Daniel, D. Mohanty, J. Li, D.L. Wood, Cathode materials review, AIP Conf. Proc. 1597 (2014) 26–43. https://doi.org/10.1063/1.4878478.

[251] H. Darjazi, A. Staffolani, L. Sbrascini, L. Bottoni, R. Tossici, F. Nobili, Sustainable Anodes for Lithium- and Sodium-Ion Batteries Based on Coffee Ground-Derived Hard Carbon and Green Binders, Energies. 13 (2020) 6216. https://doi.org/10.3390/en13236216.

[252] S.F. Lux, F. Schappacher, A. Balducci, S. Passerini, M. Winter, Low Cost, Environmentally Benign Binders for Lithium-Ion Batteries, J. Electrochem. Soc. 157 (2010) A320. https://doi.org/10.1149/1.3291976.

[253] L. Zhang, L. Chai, Q. Qu, L. Zhang, M. Shen, H. Zheng, Chitosan, a new and environmental benign electrode binder for use with graphite anode in lithium-ion batteries, Electrochim. Acta. 105 (2013) 378–383. https://doi.org/10.1016/j.electacta.2013.05.009.

[254] J. Chong, S. Xun, H. Zheng, X. Song, G. Liu, P. Ridgway, J.Q. Wang, V.S. Battaglia, A comparative study of polyacrylic acid and poly(vinylidene difluoride) binders for spherical natural graphite/LiFePO4 electrodes and cells, J. Power Sources. 196 (2011) 7707–7714. https://doi.org/10.1016/j.jpowsour.2011.04.043.

[255] C. (John) Zhang, V. Nicolosi, Graphene and MXene-based transparent conductive electrodes and supercapacitors, Energy Storage Mater. 16 (2019) 102–125. https://doi.org/10.1016/j.ensm.2018.05.003.

[256] S.J. Kim, M. Naguib, M. Zhao, C. Zhang, H.T. Jung, M.W. Barsoum, Y. Gogotsi,

High mass loading, binder-free MXene anodes for high areal capacity Li-ion batteries, Electrochim. Acta. 163 (2015) 246–251. https://doi.org/10.1016/j.electacta.2015.02.132.

[257] P. Yu, G. Cao, S. Yi, X. Zhang, C. Li, X. Sun, K. Wang, Y. Ma, Binder-free 2D titanium carbide (MXene)/carbon nanotube composites for high-performance lithium-ion capacitors, Nanoscale. 10 (2018) 5906–5913. https://doi.org/10.1039/c8nr00380g.

[258] Y. Liu, Y. Yang, Recent progress of TiObased anodes for Li ion batteries, J. Nanomater. 2016 (2016). https://doi.org/10.1155/2016/8123652.

[259] X. Du, Q. Wang, T. Feng, X. Chen, L. Li, L. Li, X. Meng, L. Xiong, X. Sun, L. Lu, Y. Xu, One-step Preparation of Nanoarchitectured TiO2 on Porous Al as Integrated Anode for High-performance Lithium-ion Batteries, Sci. Rep. 6 (2016) 20138. https://doi.org/10.1038/srep20138.

[260] E. Lester, P. Blood, J. Denyer, D. Giddings, B. Azzopardi, M. Poliakoff, Reaction engineering: The supercritical water hydrothermal synthesis of nano-particles, J. Supercrit. Fluids. 37 (2006) 209–214. https://doi.org/10.1016/j.supflu.2005.08.011.

[261] I.-A. Baragau, N.P. Power, D.J. Morgan, T. Heil, R.A. Lobo, C.S. Roberts, M. Titirici, S. Dunn, S. Kellici, Continuous Hydrothermal Flow Synthesis of Blue-Luminescent{,} Excitation-Independent N-doped Carbon Quantum Dots as Nanosensors, J. Mater. Chem. A. (2020). https://doi.org/10.1039/C9TA11781D.

[262] A. Vaughn, J. Ball, T. Heil, D.J. Morgan, G.I. Lampronti, G. Maršalkaitė, C.L. Raston, N.P. Power, S. Kellici, Selective Calixarene-Directed Synthesis of MXene Plates, Crumpled Sheets, Spheres, and Scrolls, Chem. - A Eur. J. 23 (2017) 8128–8133. https://doi.org/10.1002/chem.201701702.

[263] Z. Zhang, S. Brown, J.B.M. Goodall, X. Weng, K. Thompson, K. Gong, S. Kellici, R.J.H. Clark, J.R.G. Evans, J.A. Darr, Direct continuous hydrothermal synthesis of high surface area nanosized titania, J. Alloys Compd. 476 (2009) 451–456. https://doi.org/10.1016/j.jallcom.2008.09.036.

[264] J. Li, Y. Du, C. Huo, S. Wang, C. Cui, Thermal stability of two-dimensional Ti2C nanosheets, Ceram. Int. 41 (2015) 2631–2635. https://doi.org/10.1016/j.ceramint.2014.10.070.

[265] X. Li, X. Yin, M. Han, C. Song, X. Sun, H. Xu, L. Cheng, L. Zhang, A controllable heterogeneous structure and electromagnetic wave absorption properties of Ti2CT: X MXene, J. Mater. Chem. C. 5 (2017) 7621–7628. https://doi.org/10.1039/c7tc01991b.

[266] B. Mendoza-Sánchez, Y. Gogotsi, Synthesis of Two-Dimensional Materials for Capacitive Energy Storage, Adv. Mater. 28 (2016) 6104–6135. https://doi.org/10.1002/adma.201506133.

[267] K. Zhu, Y. Jin, F. Du, S. Gao, Z. Gao, X. Meng, G. Chen, Y. Wei, Y. Gao, Synthesis of Ti 2 CT x MXene as electrode materials for symmetric supercapacitor with capable volumetric capacitance, J. Energy Chem. 31 (2019) 11–18. https://doi.org/10.1016/j.jechem.2018.03.010.

[268] X. Zhang, Y. Liu, S. Dong, Z. Ye, Y. Guo, One-step hydrothermal synthesis of a TiO2-Ti3C2Tx nanocomposite with small sized TiO2 nanoparticles, Ceram. Int. 43 (2017) 11065–11070. https://doi.org/10.1016/j.ceramint.2017.05.151.

[269] P. Lazar, R. Mach, M. Otyepka, Spectroscopic Fingerprints of Graphitic, Pyrrolic, Pyridinic, and Chemisorbed Nitrogen in N-Doped Graphene, J. Phys. Chem. C. 123 (2019) 10695–10702. https://doi.org/10.1021/acs.jpcc.9b02163.

[270] A.H.M. Al-antaki, T.M.D. Alharbi, S. Kellici, N.P. Power, W. Lawrance, C.L. Raston, Vortex Fluidic Mediated Synthesis of TiO2 Nanoparticle/MXene Composites, ChemNanoMat. 6 (2020) 657–662. https://doi.org/10.1002/cnma.201900779.

[271] R.B. Rakhi, B. Ahmed, M.N. Hedhili, D.H. Anjum, H.N. Alshareef, Effect of Postetch Annealing Gas Composition on the Structural and Electrochemical Properties of Ti2CTx MXene Electrodes for Supercapacitor Applications, Chem. Mater. 27 (2015) 5314–5323. https://doi.org/10.1021/acs.chemmater.5b01623.

[272] C.H. Sun, X.H. Yang, J.S. Chen, Z. Li, X.W. Lou, C. Li, S.C. Smith, G.Q. Lu, H.G. Yang, Higher charge/discharge rates of lithium-ions across engineered TiO 2 surfaces leads to enhanced battery performance, Chem. Commun. 46 (2010) 6129–6131. https://doi.org/10.1039/c0cc00832j.

[273] L. Sun, W. Liu, R. Wu, Y. Cui, Y. Zhang, Y. Du, S. Liu, S. Liu, H. Wang, Bio-derived yellow porous TiO2: The lithiation induced activation of an oxygen-vacancy dominated TiO2 lattice evoking a large boost in lithium storage performance,

Nanoscale. 12 (2020) 746–754. https://doi.org/10.1039/c9nr09042h.

[274] C. (John) Zhang, S.J. Kim, M. Ghidiu, M.Q. Zhao, M.W. Barsoum, V. Nicolosi, Y. Gogotsi, Layered Orthorhombic Nb2O5@Nb4C3Tx and TiO2@Ti3C2Tx Hierarchical Composites for High Performance Li-ion Batteries, Adv. Funct. Mater. 26 (2016) 4143–4151. https://doi.org/10.1002/adfm.201600682.

[275] L. Li, G. Jiang, C. An, Z. Xie, Y. Wang, L. Jiao, H. Yuan, Hierarchical Ti3C2@TiO2 MXene hybrids with tunable interlayer distance for highly durable lithium-ion batteries, Nanoscale. 12 (2020) 10369–10379. https://doi.org/10.1039/d0nr01222j.

[276] H. Zhou, B. Pei, Q. Fan, F. Xin, M.S. Whittingham, Can Greener Cyrene Replace NMP for Electrode Preparation of NMC 811 Cathodes?, J. Electrochem. Soc. 168 (2021) 040536. https://doi.org/10.1149/1945-7111/abf87d.

[277] J. Zhang, G.B. White, M.D. Ryan, A.J. Hunt, M.J. Katz, Dihydrolevoglucosenone (Cyrene) As a Green Alternative to N,N-Dimethylformamide (DMF) in MOF Synthesis, ACS Sustain. Chem. Eng. 4 (2016) 7186–7192. https://doi.org/10.1021/acssuschemeng.6b02115.

[278] H.J. Salavagione, J. Sherwood, M. De Bruyn, V.L. Budarin, G.J. Ellis, J.H. Clark, P.S. Shuttleworth, Identification of high performance solvents for the sustainable processing of graphene, Green Chem. 19 (2017) 2550–2560. https://doi.org/10.1039/c7gc00112f.

[279] K. Pan, Y. Fan, T. Leng, J. Li, Z. Xin, J. Zhang, L. Hao, J. Gallop, K.S. Novoselov, Z. Hu, Sustainable production of highly conductive multilayer graphene ink for wireless connectivity and IoT applications, Nat. Commun. 9 (2018) 1–10. https://doi.org/10.1038/s41467-018-07632-w.

[280] X. Sang, Y. Xie, M.-W. Lin, M. Alhabeb, K.L. Van Aken, Y. Gogotsi, P.R.C. Kent, K. Xiao, R.R. Unocic, Atomic Defects in Monolayer Titanium Carbide (Ti3C2Tx) MXene, ACS Nano. 10 (2016) 9193–9200. https://doi.org/10.1021/ACSNANO.6B05240.

[281] J. Xiao, D. Mei, X. Li, W. Xu, D. Wang, G.L. Graff, W.D. Bennett, Z. Nie, L. V. Saraf, I.A. Aksay, J. Liu, J.G. Zhang, Hierarchically porous graphene as a lithium-air battery electrode, Nano Lett. 11 (2011) 5071–5078.

https://doi.org/10.1021/NL203332E/SUPPL_FILE/NL203332E_SI_001.PDF.

[282] X. Wang, S.M. Tabakman, H. Dai, Atomic layer deposition of metal oxides on pristine and functionalized graphene, J. Am. Chem. Soc. 130 (2008) 8152–8153. https://doi.org/10.1021/JA8023059/SUPPL_FILE/JA8023059-FILE002.PDF.

[283] S. Seyedin, J. Zhang, K.S. Aldren Usman, S. Qin, A.M. Glushenkov, E.S. Roswell Yanza, R.T. Jones, J.M. Razal, S. Seyedin, J. Zhang, K.A. S Usman, S. Qin, E.R. S Yanza, J.M. Razal, A.M. Glushenkov, R.T. Jones, Facile Solution Processing of Stable MXene Dispersions towards Conductive Composite Fibers, Glob. Challenges. 3 (2019) 1900037. https://doi.org/10.1002/GCH2.201900037.

[284] C.E. Ren, M.Q. Zhao, T. Makaryan, J. Halim, M. Boota, S. Kota, B. Anasori, M.W. Barsoum, Y. Gogotsi, Porous Two-Dimensional Transition Metal Carbide (MXene) Flakes for High-Performance Li-Ion Storage, ChemElectroChem. 3 (2016) 689–693. https://doi.org/10.1002/CELC.201600059.

[285] H. Abdurehman Tariq, U. Nisar, J. James Abraham, Z. Ahmad, S. AlQaradawi, R. Kahraman, R.A. Shakoor, TiO2 encrusted MXene as a High-Performance anode material for Li-ion batteries, Appl. Surf. Sci. 583 (2022) 152441. https://doi.org/10.1016/j.apsusc.2022.152441.

[286] Y. Tang, J. Zhu, W. Wu, C. Yang, W. Lv, F. Wang, Synthesis of Nitrogen-Doped Two-Dimensional Ti 3 C 2 with Enhanced Electrochemical Performance , J. Electrochem. Soc. 164 (2017) A923–A929. https://doi.org/10.1149/2.0041706JES.

[287] W. Lv, J. Zhu, F. Wang, Y. Fang, Facile synthesis and electrochemical performance of TiO2 nanowires/Ti3C2 composite, J. Mater. Sci. Mater. Electron. 29 (2018) 4881–4887. https://doi.org/10.1007/S10854-017-8446-5/FIGURES/6.

[288] T.A. Le, Q.V. Bui, N.Q. Tran, Y. Cho, Y. Hong, Y. Kawazoe, H. Lee, Synergistic Effects of Nitrogen Doping on MXene for Enhancement of Hydrogen Evolution Reaction, ACS Sustain. Chem. Eng. 7 (2019) 16879–16888. https://doi.org/10.1021/ACSSUSCHEMENG.9B04470.

[289] J. Zhang, N. Kong, D. Hegh, K.A.S. Usman, G. Guan, S. Qin, I. Jurewicz, W. Yang, J.M. Razal, Freezing Titanium Carbide Aqueous Dispersions for Ultra-long-term Storage, ACS Appl. Mater. Interfaces. 12 (2020) 34032–34040.

https://doi.org/10.1021/acsami.0c06728.

[290] S. Sarciaux, A. Le Gai La Salle, A. Verbaere, Y. Piffard, D. Guyomard, γ-MnO2 for Li batteries Part I. γ-MnO2: Relationships between synthesis conditions, material characteristics and performances in lithium batteries, J. Power Sources. 81–82 (1999) 656–660. https://doi.org/10.1016/s0378-7753(99)00095-6.

[291] D. Wu, X. Xie, Y. Zhang, D. Zhang, W. Du, X. Zhang, B. Wang, MnO2/Carbon Composites for Supercapacitor: Synthesis and Electrochemical Performance, Front. Mater. 7 (2020) 2. https://doi.org/10.3389/fmats.2020.00002.

[292] W. Song, Q. Jiang, X. Xie, A. Brookfield, E.J.L. McInnes, P.R. Shearing, D.J.L. Brett, F. Xie, D.J. Riley, Synergistic storage of lithium ions in defective anatase/rutile TiO2 for high-rate batteries, Energy Storage Mater. 22 (2019) 441–449. https://doi.org/10.1016/j.ensm.2019.07.025.

Supporting Information

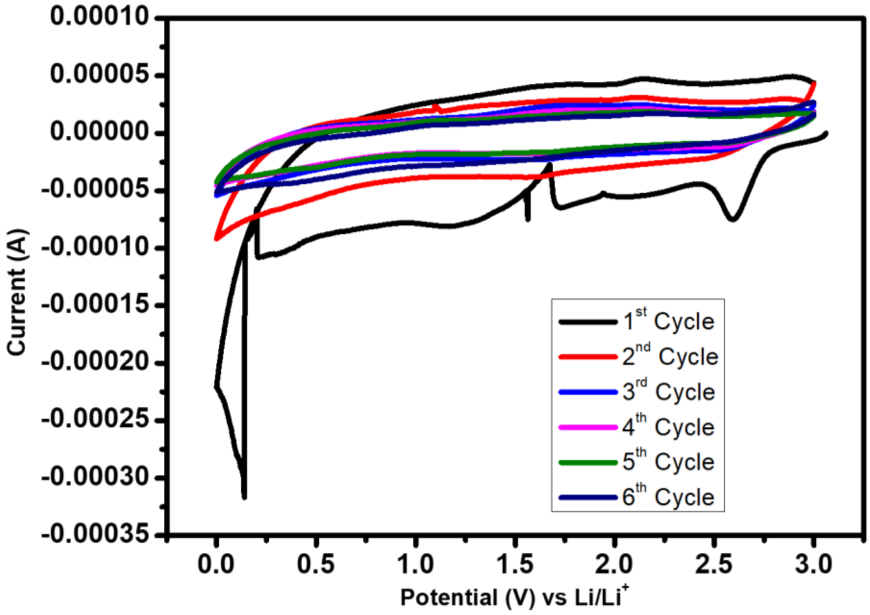

S1: 6 cycles of CV on $NTi_3C_2CYRTiO_2$

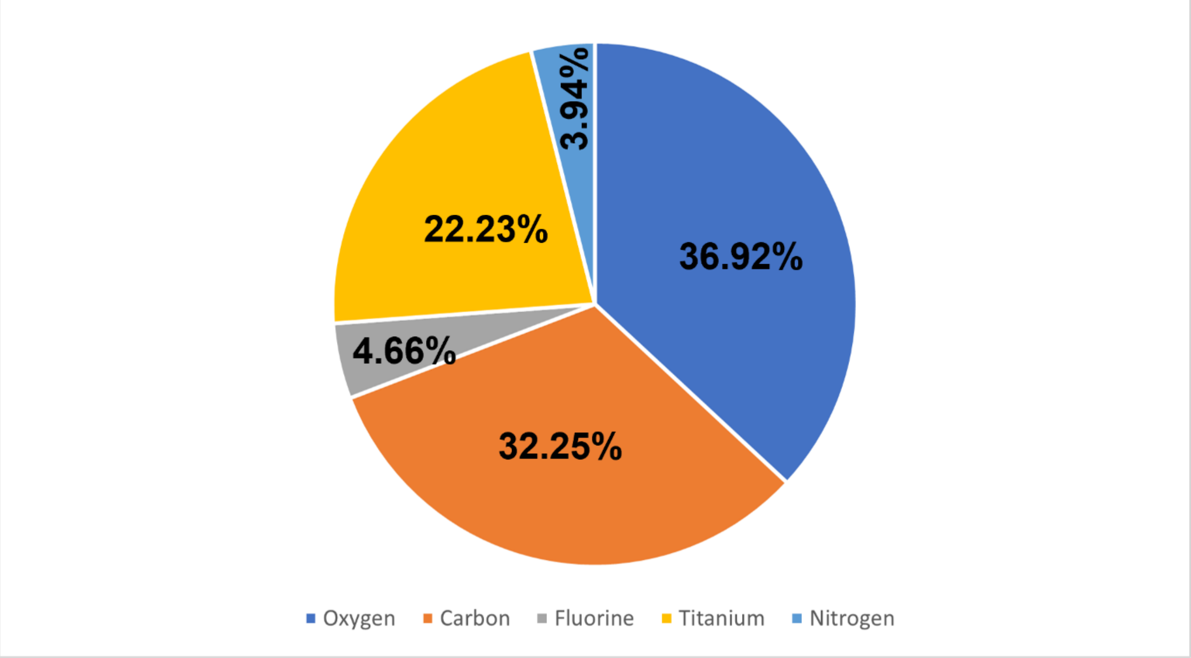

S2: Elemental % composition in $NTi_3C_2CYRTiO_2$

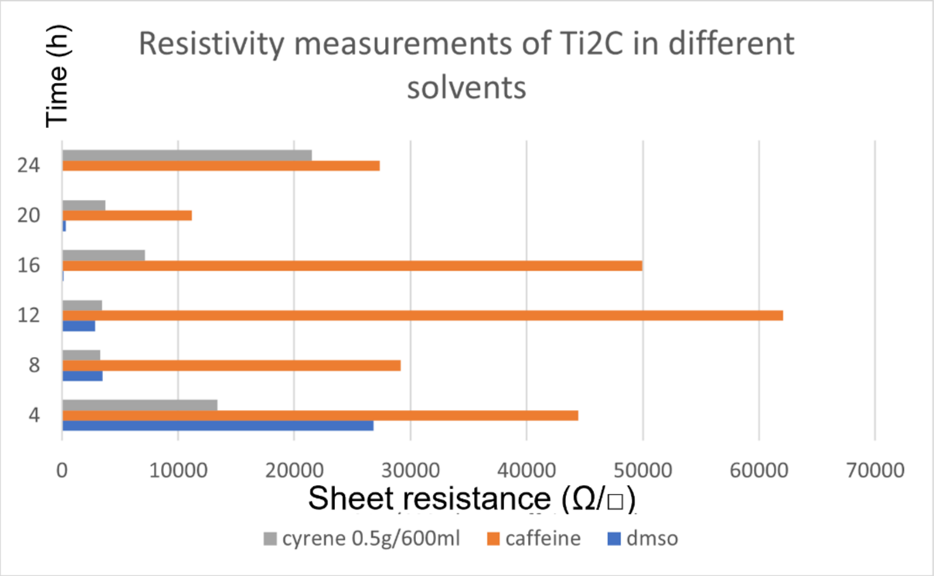

S3: Resistivity of Ti_2C MXene in different solvents